Dissertation
submitted to the
Combined Faculties for the Natural Sciences and for Mathematics
of the Ruperto-Carola University of Heidelberg, Germany
for the degree of
Doctor of Natural Sciences

Put forward by
M.Sc. Philipp Mann
Born in: Stuttgart
Oral examination: 19.04.2017

Development and implementation of 3D-dosimetric end-to-end tests in adaptive radiation therapy of moving tumors

Referees: Prof. Dr. Peter Bachert
Prof. Dr. Joao Seco

Development and implementation of 3D-dosimetric end-to-end tests in adaptive radiation therapy of moving tumors

Clinical implementation of novel advanced treatment techniques in adaptive radiation therapy requires proper workflow verification. However, this subject is not satisfactorily solved yet as current experimental validation techniques do not reflect the complexity of real patient treatments. In this thesis, several methods for patient-specific end-to-end tests were developed and applied to clinical workflows especially including treatments of moving tumors. End-to-end-tests were performed with geometrically well-defined phantoms as well as with an anthropomorphic dynamic ex-vivo porcine lung phantom in combination with a 3-dimensional (3D) polymer gel dosimeter (PGD). Different experimental settings of increasing complexity were tested in terms of (i) accuracy, (ii) feasibility of clinical workflows testing, (iii) validation of clinical concepts for motion-compensated treatments, (iv) additional integration of real-time markerless fluoroscopic imaging, and (v) validation of 4D dose calculation algorithms. Phantom irradiations were performed under static and dynamic conditions with and without beam gating. PGD evaluation revealed good tumor coverage for all treatment concepts and beam gating significantly reduced normal tissue exposure. In all cases, good agreement with the calculated dose distribution was obtained. As a conclusion, the established experimental workflow provides a versatile and valuable tool for geometrical and dosimetrical validation of advanced motion-compensated treatment techniques in adaptive radiation therapy.

Entwicklung und Implementierung von 3D-dosimetrischen End-to-End-Tests in der adaptiven Strahlentherapie für bewegte Tumore

Die klinische Implementierung neuer Behandlungsmethoden in der adaptiven Strahlentherapie erfordern eine ordnungsgemäße Validierung der einzelnen Arbeitsschritte. Allerdings ist diese Thematik noch nicht zufriedenstellend gelöst, da die derzeitigen experimentellen Verifikationsverfahren nicht die Komplexität realer Patientenbehandlungen widerspiegeln. In dieser Arbeit wurden mehrere Methoden für patientenspezifische End-to-End-Tests entwickelt und auf klinische Workflows, insbesondere die Behandlungen von sich bewegenden Tumoren, angewendet. Die End-to-End-Tests wurden sowohl mit geometrisch gut definierten Phantomen als auch mit einem anthropomorphen dynamischen *Ex-vivo*-Schweinelungenphantom in Kombination mit einem dreidimensionalen (3D) Polymer-Gel-Dosimeter (PGD) durchgeführt. Unterschiedliche experimentelle Konfigurationen zunehmender Komplexität wurden hinsichtlich (i) Genauigkeit, (ii) Durchführbarkeit klinischer Arbeitsabläufe, (iii) Validierung von klinischen Konzepten für bewegungskompensierte Behandlungen, (iv) zusätzliche Integration markerloser fluoroskopischer Echtzeitbildgebung und (v) der Validierung von 4D-Dosisberechnungsalgorithmen getestet. Phantombestrahlungen wurden unter statischen und dynamischen Bedingungen mit und ohne Gating durchgeführt. Die PGD Evaluierung zeigte für alle Behandlungskonzepte eine gute Tumorabdeckung und die Normalgewebsexposition konnte durch eine Gatingbestrahlung deutlich reduziert werden. In allen Fällen wurde eine gute Übereinstimmung mit der berechneten Dosisverteilung erzielt. Es wird daher geschlussfolgert, dass der etablierte Workflow ein vielseitiges und wertvolles Werkzeug für die geometrische und dosimetrische Validierung fortschrittlicher bewegungskompensierender Behandlungstechniken in der adaptiven Strahlentherapie darstellt.

Contents

List of abbreviations

3D-CRT	*3D conformal radiation therapy*
APR	*automated post registration*
CB-CT	*cone-beam CT*
CPMG	*Carr-Purcell-Meiboom-Gill*
CT	*computer tomography*
CTV	*clinical target volume*
D	*dose*
DTA	*distance to agreement*
DVH	*dose volume histograms*
FA	*flip angle*
FID	*free induction decay*
GTV	*gross tumor volume*
GUI	*graphical user interface*
GW	*gating window*
HU	*hounsfield units*
IC	*ionization chamber*
IGRT	*image guided radiation therapy*
IMRT	*intensity modulated radiation therapy*
ITV	*internal target volume*
LEM	*lung-equivalent material*
LINAC	*linear accelerator*
MLC	*multi leaf collimator*
MRI	*magnetic resonance imaging*
MTMA	*multiple template matching algorithm*
MU/min	*monitor units per minute*
NCC	*normalized-cross-correlation-coefficient*
NSCLC	*non-small cell lung cancer*
OAR	*organ at risk*
PAGAT	*polyacrylamide gelatine gel fabricated at atmospheric conditions*
PET	*positron emission tomography*
PGD	*polymer gel dosimeters*
PMMA	*polymethyl-methacrylate*
PTV	*planning target volume*
R_2	*relaxation rate*
RF	*radio frequency*
ROI	*region of interest*
RT	*radiation therapy*

SE	*spin echo*
SMR	*standard marker based point registration*
SNR	*signal to noise ratio*
SPECT	*single photon emission tomography*
SR	*saturation recovery*
THPC	*bis[tetrakis(hydroxymethyl)-phosphonium] chloride*
TPAR	*tumor position acceptance region*
TPS	*treatment planning system*
TR	*repetition time*
TRU-FISP	*true fast imaging with steady precession*
TV	*total variation*
VS	*voxel size*
WASABI	*water shift and* B_1

1 Introduction

Advances in the field of medical care, especially the developments of new medical treatment devices, pharmaceuticals and medical education resulted in an always growing life expectancy. Especially in the field of cancer research both, diagnostics- and treatment methods could be continuously improved and therefore increases the quality of life of patients. However, cancer still remains one of the main causes of death in industrialized countries all around the world. In 2013, a total of 482.500 persons were diagnosed with cancer in Germany while 223.088 died in the same year (Zentrum für Krebsregisterdaten im Robert Koch-Institut 2016). These numbers show that in spite of an increasingly personalized medical care, the mortality still remains at a very high level. Tailoring treatments to the needs of the individual patient is therefore still an important field of research and new developments and treatment techniques should be quickly transferred into clinical routine.

In general, cancer is a diseases type that causes malignant tissue cells (called: *tumor cells*) to proliferate uncontrolled, which is often accompanied by invasion of the tumor into adjacent healthy tissue as well as the ability of tumor cells to spread in other parts of the body. The underlying processes are very complex and not fully understood. Therefore, a large variety of different treatment approaches were developed. Standard treatment modalities include surgery, chemotherapy and radiation therapy, which follow either a curative- or palliative approach.

In case of radiation therapy (RT), the fundamental paradigm relies on delivering a high therapeutic *dose* (D) to the tumor volume while sparing the surrounding normal tissue. A major advantage of radiation therapy is its non-invasive nature thereby providing the possibility to treat tumors that cannot completely be resected by surgical interventions (e.g. because vital organs (organs at risk, OAR)) as they are located in the surgical access path. Using radiation therapy together with dedicated immobilization techniques, irradiations even of deep-seated tumors can be performed with high accuracy (in the order of $1-2\ mm$). However, this can only be realized if the exact tumor position inside the patient is known within the same accuracy. For this, three-dimensional (3D) imaging modalities are used to localize the tumor as well as the OARs. Nowadays, imaging includes computed tomography (CT) and often additionally magnetic resonance imaging (MRI). Images are then used to delineate the tumor (gross and clinical target volume, GTV and CTV) and the OARs (ICRU Report No 50 1993) and to optimize optimal treatment parameters such as dose, beam shapes and beam direction to maximize the dose within the tumor, while minimizing the dose to adjacent OARs. This process is the essential part of treatment planning which is performed separately for each individual patient. This process, however, is still accompanied by several uncertainties that need to be taken into account. This includes uncertainties due to patient positioning, anatomical changes between two irradiations sessions (so-called inter-fractional changes of the anatomy) or during the treatment itself (e.g. by intra-fractional motion). To account for these uncertainties, additional safety margins are usually included in the definition of the planning target volume (PTV).

Uncertainties related to patient positioning and inter-fractional anatomical changes can be reduced by a combination of (i) a proper patient immobilization and (ii) additional image information acquired in the treatment position directly before the treatment. While (i) can be realized by stereotactic systems or personalized immobilization molds, (ii) is realized by on-board imaging systems. These images are then compared against reference images from treatment planning and, if necessary, the patient position is corrected. This technique is known as image guided radiation therapy (IGRT).

However, this task becomes especially challenging for intra-fractional motion as the tumor may exhibit larger displacements caused by respiratory- (e.g. for lung tumors (Plathow et al. 2004, Keall et al. 2006)) or cardiac motion. In conventional radiation therapy planning, this is compensated for by delineating the so-called internal target volume (ITV), which includes the whole tumor in all breathing phases (ICRU Report No 62 1999). Adding additional margins to take account for remaining uncertainties caused by positioning and beam delivery, then results in the PTV. This concept assures that the tumor is covered with dose in all breathing phases. Depending on the magnitude of the motion, this technique is usually accompanied by a higher normal tissue exposure and therefore leading to an increased risk of long term side effects.

Modern adaptive radiation therapy aims at compensating for such organ motion e.g. by including beam gating (Kubo & Hill 1996, Jiang 2006) or tracking (Tacke *et al* 2010). While gating aims at irradiating the tumor only, if it is located at a specific position, tracking techniques attempt to follow the motion trajectory of the tumor during irradiation. Both methods require information on the exact tumor position during irradiation. This can be realized by either direct tumor monitoring using fluoroscopic imaging (Cui et al. 2007, Tang *et al* 2007, Moser *et al.* 2008, Witte 2016) or indirect surrogate techniques, such as spirometer (Keall *et al* 2006), breathing belts (Moser *et al* 2008b), body surface imaging (Bert et al. 2006, Bert et al. 2005) or by means of implanted electromagnetic markers (Schmitt *et al* 2012). However, clinical implementation of such techniques require end-to-end tests where the entire intended workflow from image acquisition to dose delivery is validated by dedicated phantom measurements as well as by dose calculations. An ideal experimental setting should therefore include phantoms with (i) anthropomorphic image contrast for a large variety of different imaging modalities (e.g. CT, MRI and fluoroscopy), (ii) realistic motion patterns comparable to those in patients, (iii) the possibility to measure the delivered dose within the phantom in three dimensions (3D), and (iv) real-time acquisition of the tumor position using clinically accepted tracking devices to retrospectively perform a 4D (3D+time) dose calculation.

Such an experimental setting is required to simulate the entire chain of patient-treatment for moving targets which includes CT imaging, treatment planning, dose delivery and retrospective 4D dose calculation. Various settings have been proposed including both, in-house developed or commercially available breathing phantoms (Vedam et al. 2003, Court et al. 2010a, Szegedi et al. 2010, Court et al. 2010b, ‘Quasar’ (Modus Medical Devices Inc., London, Canada) and the ‘Dynamic Thorax Phantom’ (CIRS, Norfolk, VA, USA)). However, these phantoms do usually not include the complexity, uncertainties and difficulties present in real patient treatments and usually lack of 3D dose measurements.

In this work, an experimental setup was developed and implemented that meets the above mentioned requirements by combining a 3D polymer gel dosimetry-based target volume (Venning *et al* 2005) with various phantom settings of increasing complexity. This includes well-reproducible, geometrical, static and dynamic phantoms with various tissue-equivalent inserts as well as a dynamic anthropomorphic porcine lung phantom (Biederer and Heller 2003), which reflects the complexity of real patients.

The polymer gel dosimeter (PGD) has shown to be a suitable method to measure 3D dose distributions (Schreiner 2006) within containers of arbitrary shape and has already been applied for IMRT (Vergote et al. 2004, Sandilos et al. 2004) as well as in combination with respiratory motion (Ceberg *et al* 2008) and 4D dose calculation (Niu *et al* 2012). The entire setup was used to evaluate various radiation techniques including static and dynamic targets with and without application of beam gating. Experiments include (i) investigation of the accuracy of the PGD, (ii) feasibility of the application of PGD within the porcine lung phantom (iii) validation of a clinical workflows including the application of clinical margins and motion-compensation concepts, (iv) integration of fluoroscopy for the validation of the surrogate signal, and (v) validation of an in-house developed 4D dose accumulation algorithm (Schlegel *et al* 1992, Schmitt *et al* 2012).

2 Material and methods

2.1 Image-guided radiation therapy

The fundamental idea of radiation therapy relies on the process of delivering a therapeutic dose to the tumor volume while sparing the surrounding normal tissue. On one hand, the major advantage of RT is its non-invasive nature and ability to locally deposit dose with high precision that allows treating tumors that are located close to OARs. On the other hand, however, this involves various challenges as “radiation therapy is the art of hitting an invisible target with an invisible beam” (Schlegel 2005). The following section will give a short introduction to the basic principle of RT, including tumor localization, treatment planning, state-of-the-art beam delivery techniques and an outline on current developments in IGRT.

2.1.1 *The general RT process*

Generally, the principle of radiation therapy is based on energy deposition within a previously defined target volume by ionizing radiation. In RT, the term *dose* is precisely defined as the amount of absorbed energy dE per irradiated unit mass dm ($D = \frac{dE}{dm}$) using water as reference medium. The absorbed dose to water is expressed in units of Gray ($1\ Gy =\ 1\frac{J}{kg}$). As the lethal dose for a whole body irradiation amounts to $4.5\ Gy$ (Mole 1984), the underlying reason of radiation induced tumor death cannot be correlated to a temperature increase $\Delta T\ [K]$ as this is only a minor effect ($\Delta T \approx 0.23\ mK/Gy$ in tissue). On a microscopic level, the ionization radiation induces DNA damage within the cell (either single- or double strand breaks). As a result, depending on the dose and radiobiological properties, this can lead to cell death. However, this effect occurs for both, tumor- and normal tissue. Since the main goal of precise radiation therapy is to kill the tumor cells while avoiding normal tissue- or OAR irradiation, special measures needs to be taken. For this, two radiobiological principles are applied (i) tissue sparing and (ii) fractionation. Tissue sparing is realized by conformal radiation techniques and will be explained in the following sections. Fractionation, on the other hand, uses the fact that repair of sub-lethal damage in cells is more efficient in normal than in tumor cells (Sauer 2010). Consequently, treatment is usually split in many small doses (“fractions”) delivered over a larger period of time (typically 30 fractions of 2 Gy in 6 weeks). Optimization of RT using these two principles, however, is not within the scope of this work.

The general RT process can be divided into three major steps:

(i) Imaging
(ii) Treatment planning
(iii) Treatment delivery

2.1.1.1 Imaging

Prior to the treatment planning procedure, an anatomical CT image of the patient is acquired, which is then used for segmentation of tumor and OARs and by this defines a geometrical model of the patient. The segmentation process may be supported by additional images of other imaging modalities (e.g. MRI, positron emission tomography (PET) or single photon emission tomography (SPECT)), which provide additional morphological or functional information on the tumor and the normal tissues. As second important feature, the CT provides information about the attenuation of the ionizing radiation in the tissue, which is then used to calculate the dose distribution within the patient. Thus, the geometrical model gets complemented by an attenuation model of the patient. This is possible as the image acquisition of CT and the irradiation of the tumor underlie the same physical principles. Although CT images are usually acquired in a voltage range between 80 kV and 120 kV compared to the energy spectrum of conventional photon RT ranging from $6 - 18$ MeV, CT-based attenuation coefficients (usually given in Hounsfield units, (HU)) can also be extrapolated to higher energies and are thus used for dose calculation in treatment planning.

Accurate delivery of the dose distribution requires identical patient immobilization and positioning during imaging and treatment delivery. For this, different techniques are used in clinical routine, ranging from a rather simple point marker approach (usually attached to the patient's body surface) up to a fixation with customized molds. In the case of moving tumors (e.g. caused by breathing inside the lung), additional information on tumor trajectory is required for proper treatment planning. This is usually realized with the acquisition of an additional 4D-CT dataset (Korreman 2012). For this, an external trigger signal (e.g. from a breathing belt or internal markers, Section 2.1.2) captures the current motion state, which can then be used to correlate each CT image projection to a specific motion state. The complete CT image at each breathing phase is then reconstructed using only the projection of the respective breathing phase. Although CT images provide time resolved images with high spatial resolution, the morphological- and functional information is rather low. Depending on the irradiation site, other imaging modalities are additionally used to achieve a much better soft tissue contrast (as for MRI) or functional information (MRI and PET) that can further improve tumor- or OAR localization.

2.1.1.2 Treatment planning

The planning process itself can be divided into three sub-steps: (i) image registration and segmentation, (ii) definition of treatment parameters and (iii) dose calculation. Although each substep requires a large variety of different techniques, including image processing and iterative optimization, the entire planning process is usually performed on a single platform, the so-called treatment planning system (TPS). As a first step, the images are transferred to the TPS. If more than a single CT dataset is used, all images need to be co-registered by means of proper registration algorithms which are optimized with respect to the imaging modalities (e.g. MR and CT (Brock and Dawson 2014)). As a next step, different volumes have to be delineated on the planning CT (ICRU Report No 62 1999) prior to dose prescription and calculation. For the tumor volume, up to four different areas are defined to account for (i) tumor location, (ii) clinical spread of the tumor, (iii) tumor motion, and (iv) both, machine- and positioning-related uncertainties. The delineation of the gross tumor volume (GTV) includes the visible part of the tumor. As there may be some infiltration of tumor cells in the surrounding normal tissue, which is not visible on the image data, an additional clinical target volume (CTV) is defined by a physician. The CTV is usually based on historical series of large patient cohorts, tumor types and tumor location. Additional information from different imaging modalities can assist the CTV delineation, as the CTV is most likely one of the most difficult volumes to define (Burnet *et al* 2004). However, it should be noted that including co-registered images from other modalities may also introduce additional geometrical uncertainties originating from the co-registration algorithm (Chuter 2015). In case of tumor motion, the ITV is defined as the superposition of all CTVs that have been delineated on all 4D-CT phases (Vinet and Zhedanov 1970). The final PTV additionally accounts for machine- and positioning related errors. For a standard treatment plan design where neither image guidance (see Figure 1) nor tumor metabolism is taken into account, the entire volume is uniformly irradiated. An example, how various margins can significantly increase the size of the irradiated volume is shown in Figure 2, where a spherical tumor with a diameter of $d = 10\ mm$ has been assumed. The PTV-volume is displayed assuming an isotropic margin between CTV and GTV including a one dimensional tumor motion on the vertical axis (see also Figure 1(a)). In this example, the final PTV increases by a factor of 4 with respect to the GTV, if only the margins for CTV and PTV are considered and it increases up to a factor of 30 if motion is additionally considered. This exemplary calculation shows the importance of minimizing patient- and treatment-related uncertainties. A short overview on various treatment techniques allowing for reduction of margins will be given in Section 2.1.2. As a next step, the parameters of the treatment plan (e.g. number and orientations of beams and field shapes) have to be defined and for these parameters, the dose distribution is calculated by the TPS. In an iterative process, the dose distribution is optimized with respect to the clinical goals. Depending on the shape, size and location of the target volume and OAR, different treatment techniques can be applied:

3D conformal radiation therapy (3D-CRT):
This technique uses a pre-defined number of beam directions to uniformly irradiate the delineated PTV. The beam shape and dose per beam are manually optimized to match the tumor with the contour of the PTV to a pre-defined level of uniform dose distribution. This is visualized by the so-called isodose line and is usually equals the median dose. In modern radiation therapy, shaping of the beam is realized by means of a multi leaf collimator (MLC, Section 2.1.1.3).

Intensity modulated radiation therapy (IMRT):
To further optimize dose delivery with respect to a uniform PTV coverage while sparing the dose to OARs, beams with non-uniform fluence distributions are used. This can be realized by superimposing various beam apertures that are individually formed by the MLC. As a result, very complex-shaped dose distributions may be generated allowing for sparing of OARs even in cases where the tumor surrounds the OAR. As the number of degrees of freedom is strongly increased in IMRT, so called inverse dose optimization techniques have to be used. This aims at automatically determining shapes and weights of the beams based on dose constraints for the tumor and the OAR. Nevertheless, the first optimization result may not be satisfying and an iterative approach may be required. Different techniques to deliver IMRT are available, including the step-and-shoot-, the sliding window- and the rotating arc-technique. For more information, the reader is referred to a review on IMRT by Bortfeld 2006.

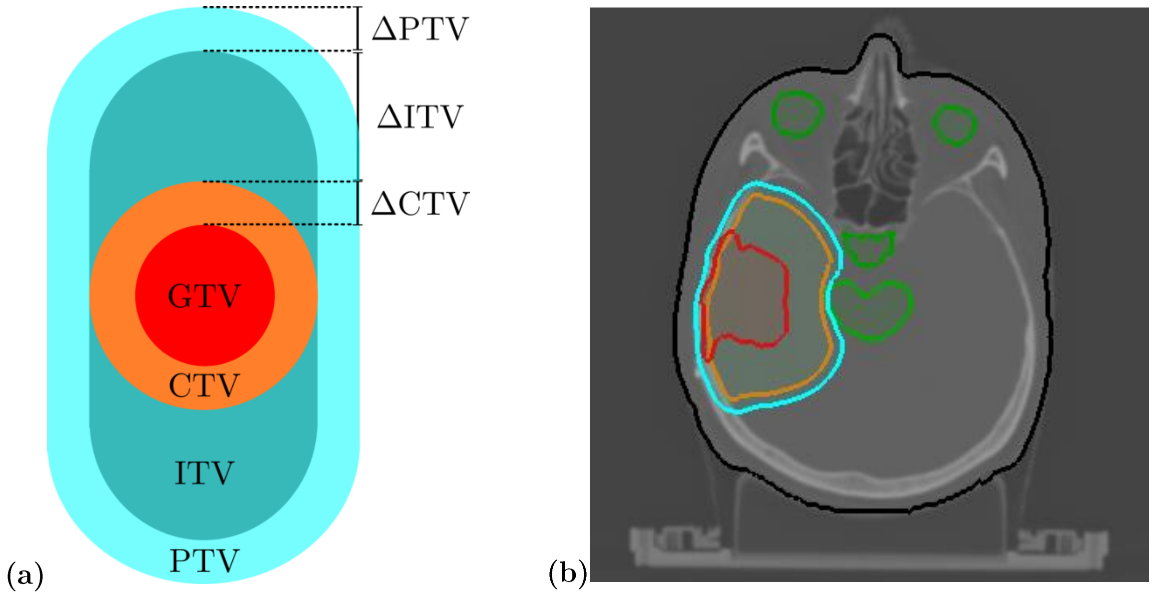

Figure 1. (a) Schematic overview of delineated target volumes for treatment planning: GTV (red), CTV (orange), ITV (grey), PTV (blue). Δ refers to the margins between the different target volumes. (b) In addition to the target volumes, various OARs (green) and the skin (black) are visualized for an anonymized treatment plan.

2.1.1.3 Treatment delivery

Prior to the treatment, the patient is positioned on the treatment table by means of an individual fixation aid using external- or internal-markers. Dose delivery is then performed in most cases with high-energy photons generated by a medical linear accelerator (LINAC). The treatment beam is produced by electron acceleration which is directed to a target made of materials with high atomic number (e.g. tungsten). As a result, the electron-target interaction produces bremsstrahlung and characteristic X-rays. As a next step, a so-called flattening filter (usually a cone-shaped peace of tungsten) is used to produce a uniform beam fluence. The beam shape is then defined by means of a MLC, which typically consists of 2×80 opposing tungsten leafs having a width of $0.5\ cm$. These leaves can be moved independently to create a large variety of beam-shapes. The entire setup is mounted on a so-called *gantry* which allows rotating the beam around the patient. As a result, a large variety of different beam shapes and –directions can be produced to realize a highly personalized tumor treatment. Depending on the depth of the target, different beam energies may be selected (typical range: $6-18\ MV$). A schematic sketch of a medical LINAC is visualized in Figure 3.

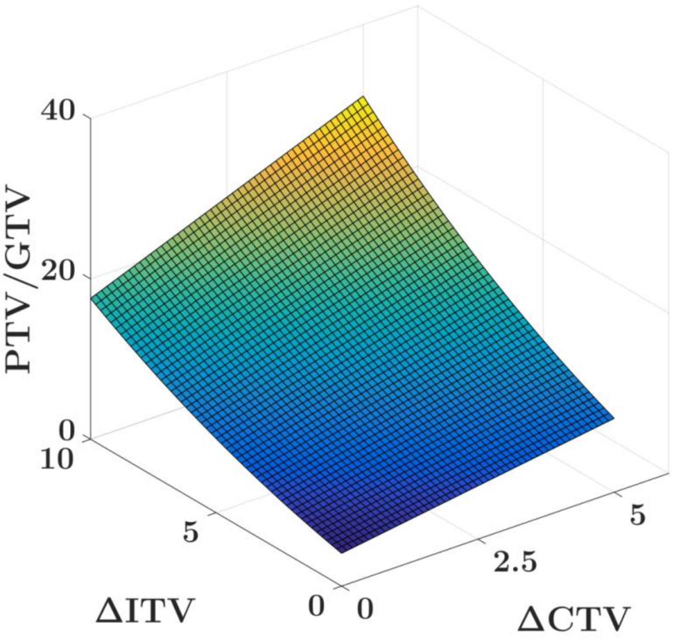

Figure 2. Ratio of PTV and GTV for a spherical tumor with a diameter of 10 mm as a function of target volume increase by ΔITV and ΔCTV . The absolute tumor volume was calculated for a maximum motion amplitude in one direction of up to 20 mm and a maximum CTV-margin of 5 mm. The final PTV includes a safety margin of $\Delta PTV = 3$ mm to compensate for both, machine- and positioning- related errors.

2.1.2 *Motion-compensation concepts*

Radiation therapy aims at covering the tumor uniformly with dose while minimizing the dose to the surrounding normal tissue, a task which becomes very challenging in case of moving targets. In particular, lung tumors may exhibit large displacements due to respiratory motion (Vedam *et al* 2003, Plathow *et al* 2004, Keall *et al* 2006) and conventional extension of the PTV with the purpose of full ITV coverage (Vinet and Zhedanov 1970) leads to higher normal tissue exposure. This is especially problematic if the precision and accuracy of beam delivery is very high and the dose delivery is divided into several fractions on different days. Although patient positioning can in principle be reproduced on the LINAC site by using a dedicated protocol (e.g. by external markers or fixation masks) it cannot be guaranteed that internal structures maintain a constant position when comparing to the planning CT-acquisition. As a result, positioning uncertainties may occur and internal structure may change during the treatment which can therefore lead to a deviation between planned and delivered doses.

In the following, techniques are described that allow compensating for (i) positioning errors and inter-fractional motion and (ii) uncertainties that are related to delivery errors in presence of intra-fractional motion.

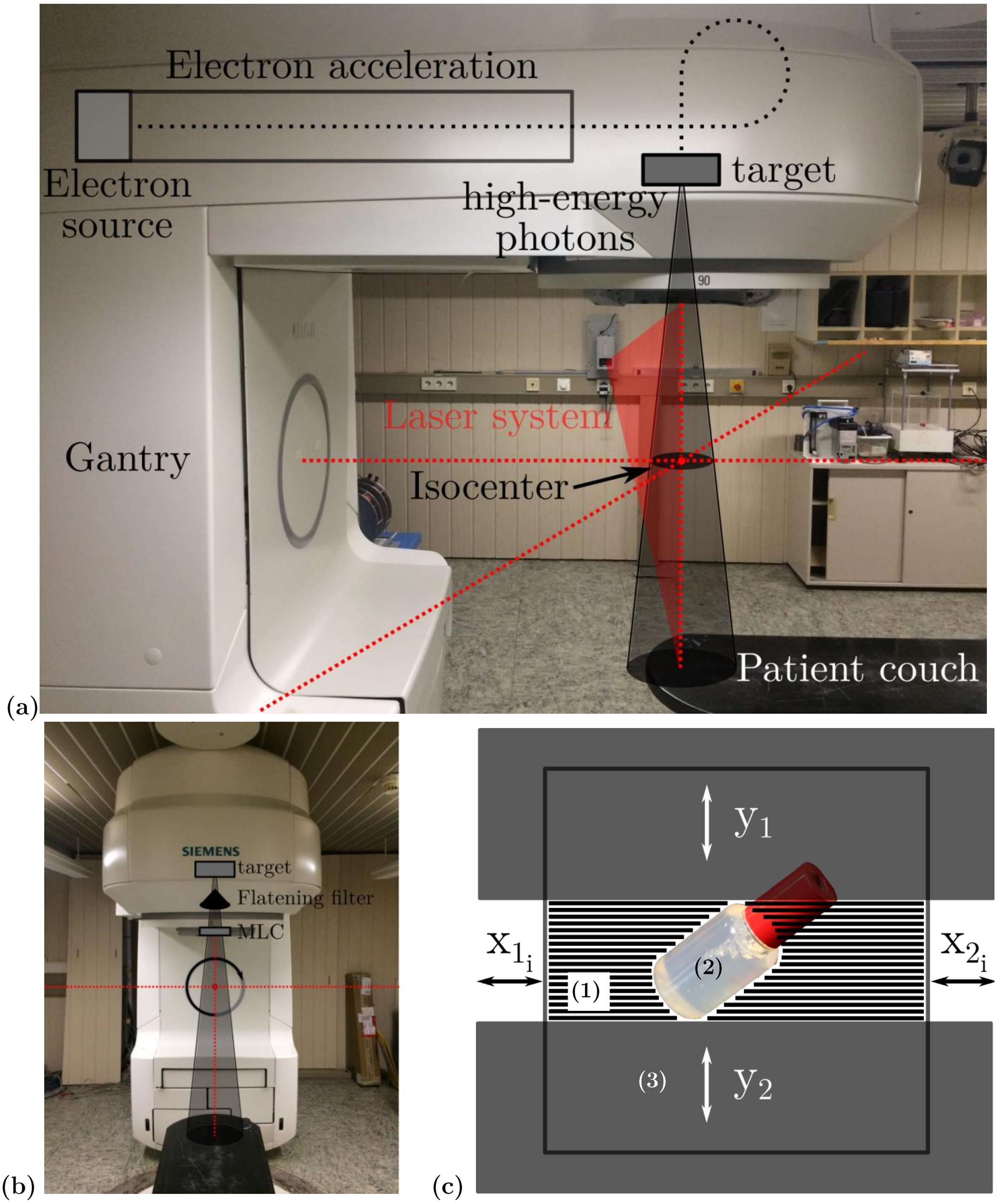

Figure 3. Side- (a) and front view (b) of a medical linear accelerator for photon irradiation. Beam shaping is realized by the MLC (c). It consists of multiple opposing leafs that can individually be moved in x-direction (1) to match die contour of the PTV (2). In addition, y-jaws (3) limit the beam in y-direction and consist of two solid independently movable blocks made of tungsten.

2.1.2.1 Inter-fractional motion-compensation

Inter-fractional motion describes all geometrical uncertainties, which may occur from fraction to fraction. This includes changes within the patient like tumor shrinkage, different bladder fillings or organ deformations. In principle, these uncertainties can be compensated for by applying the ICRU margin concept (ICRU Report No 50 1993). However, as visualized in Figure 1, this may lead to a significant PTV increase. A widely used workflow to minimize uncertainties that are related to positioning or inter-fractional errors is offered by IGRT which uses additional images acquired in the treatment room. This is usually realized by an imaging system that is mounted on the LINAC. The acquired images can then be used to compare the actual position of important structures (e.g. PTV or OARs) with that in the reference CT. Deviations are corrected for either by re-positioning or in case of larger deviation (e.g. caused by significant PTV shrinkage or growth) by re-planning. Imaging is realized either by an on-board kV-imaging system with an opposed flat panel detector or by using the treatment beam itself in combination with additional detectors. Depending on the tumor location either planar- (2D) or CT-images (3D) are acquired. In contrast to a diagnostic CT, which uses a fan beam geometry, the CT at the LINAC uses a cone beam and is therefore referred to as cone-beam CT (CB-CT). One major drawback of this image acquisition technique is that both, image quality due to high scatter contribution (Siewerdsen and Jaffray 2001) and time resolution are significantly lower. This is the reason why CB-CT are not routinely used for on-site re-planning yet.

2.1.2.2 Intra-fractional motion-compensation concepts

Intra-fractional motion is defined as tumor or organ motion, which is present *during* the treatment. Prominent examples include breathing and prostate motion (Schmitt *et al* 2012). Adaptive radiation therapy techniques attempt to compensate such organ motion e.g. by gating (Kubo and Hill 1996, Jiang 2006) or tracking (Tacke *et al* 2010). While gating aims at irradiating the tumor only, if it is located at a specific position (so-called *gating window*), tracking techniques attempt to follow the motion trajectory of the tumor during irradiation. As a successful implementation of both methods requires the knowledge of the exact tumor position, different techniques were proposed that use either direct tumor monitoring by fluoroscopic imaging (Cui *et al* 2007, Tang *et al* 2007, Moser *et al* 2008) or electromagnetic markers (Shah *et al* 2013) or alternatively indirect surrogate signals, such as body surface imaging (Bert *et al* 2006, 2005), spirometer (Keall *et al* 2006), or breathing belts (Moser *et al* 2008). More recent developments in real-time non-invasive intra-fractional motion monitoring also focus on the implementation of MRI in combination with a LINAC (Kontaxis *et al* 2015). Major advantages of this so called MRI-guided RT approach include continuous image acquisition and a very high soft tissue contrast. As in this work, motion monitoring is realized by either a breathing belt or electromagnetic markers, a short introduction to both systems will be given in the following:

Anzai Respiratory Gating System:

The Anzai respiratory gating system (Anzai Medical, Co., Ltd, Tokyo, Japan) is a well-established motion management system that can be used for both, image acquisition and radiation therapy treatment. It consists of a pressure sensitive sensor which is attached by means of an additional belt on the thorax or abdomen of the patient. It measures the relative change in pressure on the sensor which is caused by patient breathing and is then converted into a digital signal with an update rate of 40 Hz. This system is widely used for CT imaging as it allows correlating the current breathing phase to a specific CT projection to acquire 4D-CT datasets. Acquisition of time-resolved CTs is an essential step for the definition of the ITV. Nonetheless, this system is a rather simple approach to visualize patient motion as the signal is provided in 1D only and should therefore be used with care. This is especially valid when the system is applied in radiation therapy (e.g. gating) as a unique correlation between the surface signal and tumor position is not necessarily given (Korreman *et al* 2006) and different breathing pattern (e.g. abdominal and thoracic) can cause signal variation that do not correspond to the actual tumor position. Nevertheless, the system was used in this work for both, 4D-CT acquisition as well as for the realization of gated irradiations as the used phantom (see Section 2.2.3 for more details) shows a highly reproducible correlation between breathing signal and tumor position. An exemplary Anzai signal, which was acquired during a gated phantom irradiation, is shown in Figure 4.

Electromagnetic marker system:
The Calypso^{TM} tracking system (Varian Medical Systems Inc., Palo Alto, CA, USA) is designed to monitor both, patient positioning and tumor motion during radiation therapy (e.g. for prostate- (Balter *et al* 2005) and lung tumors (Shah *et al* 2013)). Data acquisition is realized by means of three implanted electromagnetic transponders being located either within or close to the target volume. These so called beacons^{TM} are excited by external electro-magnetic source coils (Mate *et al* 2004) with resonance frequencies of 300, 400 and 500 kHz. The excited beacons emit resonance signals which are then detected by a sensor array. An optical infrared camera system is used to locate the spatial position of the sensor array within the treatment room (see Figure 5). This information is used by the implemented tracking algorithm to estimate the absolute location of the beacons with an accuracy of < 1 mm with an update rate of 10 Hz (Franz *et al* 2014). A major advantage of this tracking system is that neither visibility of the markers nor cable connections to the electromagnetic transponders are required. A patient-based lung tumor tracking record is displayed in Figure 6 for tumor motion in x-, y- and z-direction. Besides its tracking capabilities, the Calypso^{TM}-system allows to monitor the beam-on/off time during the irradiation such that acquired data can be used to retrospectively perform a 4D dose calculation (Schmitt *et al* 2012).

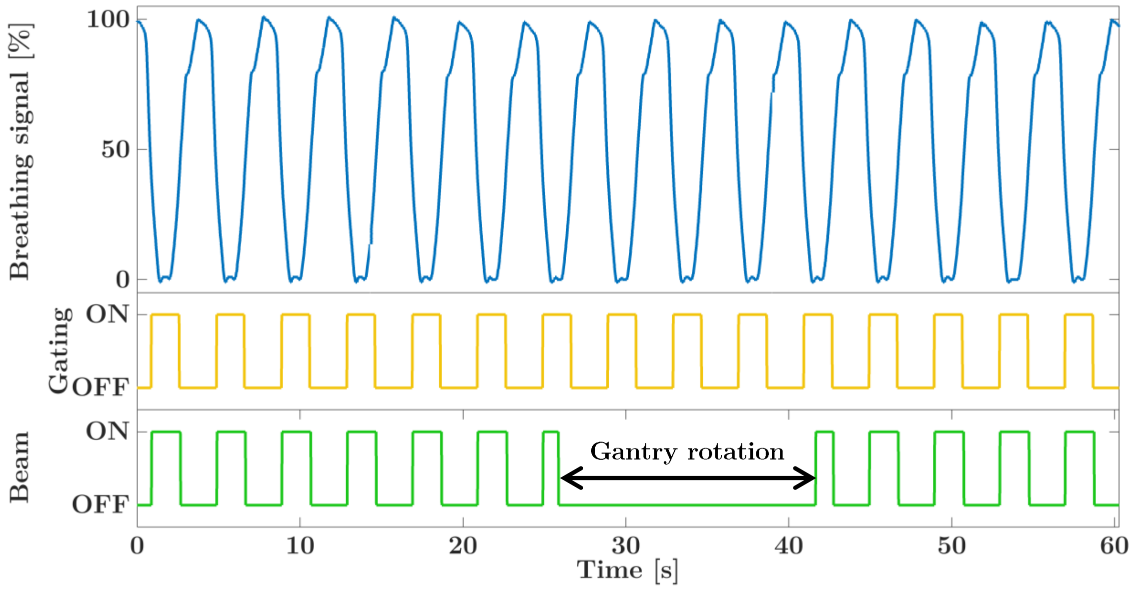

Figure 4. Respiratory motion signal of the porcine lung phantom (Section 2.2.3) recorded by the Anzai breathing belt (blue). The gating window was set to phase signal of 40% based on 4D – CT data. The corresponding gating- (yellow) and beam-on signal (green) are also displayed. During the gantry rotation, the beam signal is switched off.

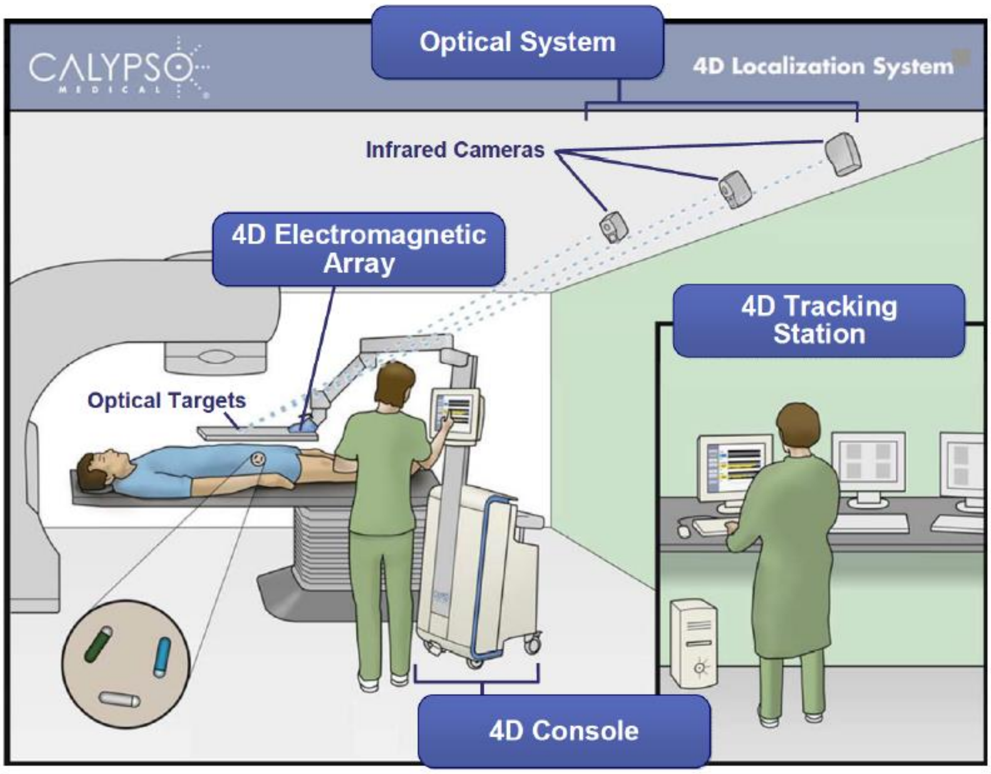

Figure 5. Schematic setup of the Calypso^{TM}-system in patients (adapted from Calypso^{TM} Medical Technologies 2010). Prior to treatment, electromagnetic markers are implanted into the patient. The 4D electromagnetic array is placed close to the marker region. To correlate the markers to the coordinate system of the treatment machine, fiducials are located on top of the electromagnetic array and are localized by three stationary infrared cameras. The control unit is located in the LINAC control room and allows monitoring of the electromagnetic markers.

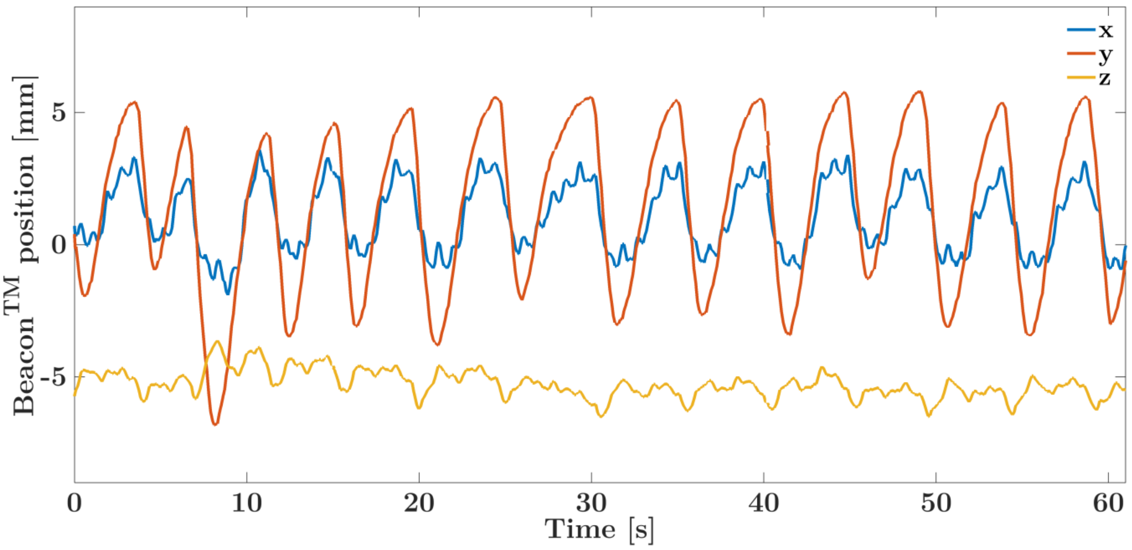

Figure 6. Breathing curve of a patient recorded with the Calypso^{TM} tracking system. Different motion directions are displayed in different colors: blue (anterior-posterior), red (superior-inferior) and orange (right-left).

2.2 Phantoms for end-to-end-tests

Before new treatment concepts in IGRT for intra-fractional motion-compensation can be implemented and tested in the clinic, the intended workflow need to be validated first. This is usually done with dedicated phantoms that provide (i) realistic motion patterns ideally from real patient data, (ii) an anthropomorphic image contrast for radiological imaging, and (iii) the ability to measure the delivered dose in 3D. This phantom could in principle be used to perform the entire chain of adaptive radiation therapy. This includes CT imaging, treatment planning and dose delivery. A large variety of different phantoms have already been developed (Szegedi *et al* 2010), Vedam *et al* 2003, Court *et al* 2010, 'Quasar' (Modus Medical Devices Inc., London, Canada) and the 'Dynamic Thorax Phantom' (CIRS, Norfolk, VA, USA)). However, up to now there is no phantom available that meets (i) – (iii) as they usually do not reflect the complexity of real patients, and if they do, information on dose delivery is not provided in 3D. In this work, a new and unique approach is presented that meets (i) – (iii) by combining a dynamic anthropomorphic porcine lung phantom (Biederer and Heller 2003) with polymer gel dosimetry (Section 2.3) which allows measuring the dose in 3D.

2.2.1 *Cylinder phantom*

Initial quantification of the implemented workflow in terms of accuracy and precision had to be validated first. For that, a phantom was developed which allows to benchmark 3D polymer gel dosimetry experiments with TPS-based dose calculations under different, well-defined conditions (see Figure 7). This is realized by a phantom with a modular structure. It consists of a double-walled cylindrical polymethyl-methacrylate (PMMA) shell (inner and outer diameter: 16 cm and 18 cm, respectively, height h=10 cm) that allows using different inserts for each phantom region. The ring-shaped space between the walls was designed to simulate the outer part of the human body (muscle and/or fat tissue) and can be filled with different solid or liquid materials, while the inner cylindrical volume mimics different parts of the inner human body. In our experimental setup, the outer shell was filled with water, while the inner volume was either filled with water or lung-equivalent material (LEM, Obomodulan 302, OBO-Werke GmbH & Co. KG, Stadthagen, Germany). Obomodulan has similar density and x-ray absorption properties as real lung tissue (Vásquez *et al* 2012). Additionally, a 3D printed mounting was developed that allows holding a dosimetry gel-filled flask (subsequently referred to as *gel tumor*) which can be placed at the center of the phantom. For absolute dose measurements, an ionization chamber or diode can be alternatively placed in the center of the phantom.

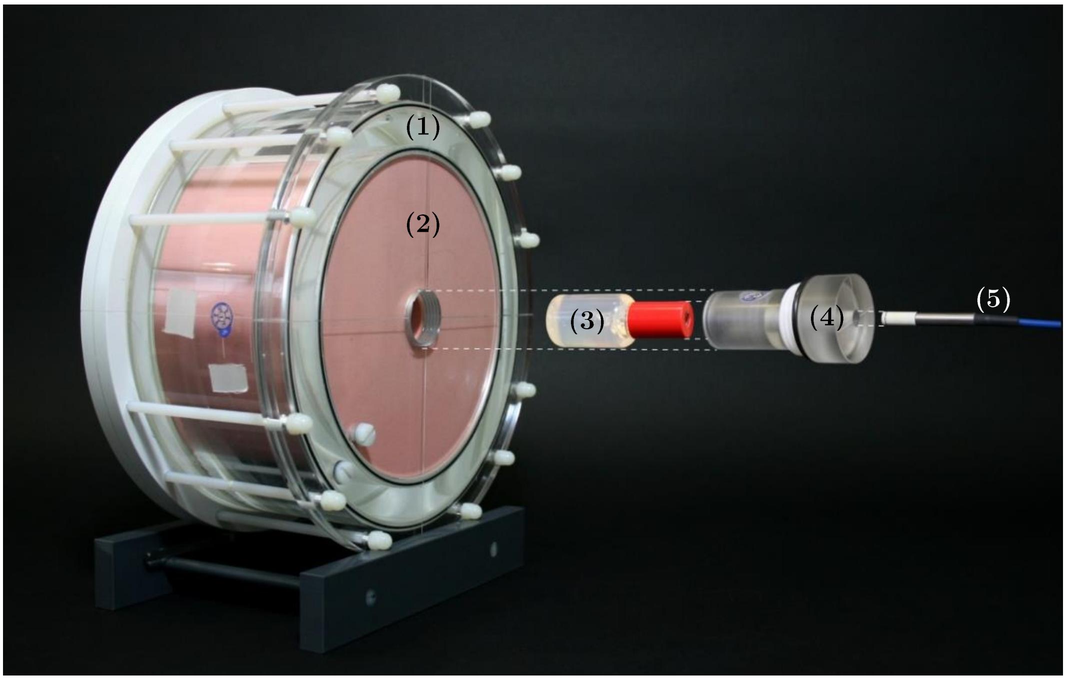

Figure 7. The cylinder phantom consists of two separate modules, namely a water-filled PMMA ring (1) and (2) a cylindrical insert which can be filled with different materials . Dose measurements can be performed by either inserting a PGD container (3) by means of a dedicated holder (4) or a diode for absolute dose measurement in 1D (5).

2.2.2 *Motion robot*

To further increase the complexity of the experimental setting in combination with the PGD measurements, a motion robot was used to move a phantom in 3D with a high reproducibility. The motion robot allows performing any arbitrary motion in three dimensions with amplitudes of up to 20 cm with a maximum speed of 7.9 cm/s. It is also possible to load datasets containing individually designed or patient-specific motion trajectories (e.g. acquired from Calypso^{TM} data) to the control unit and transfer it to the motion robot.

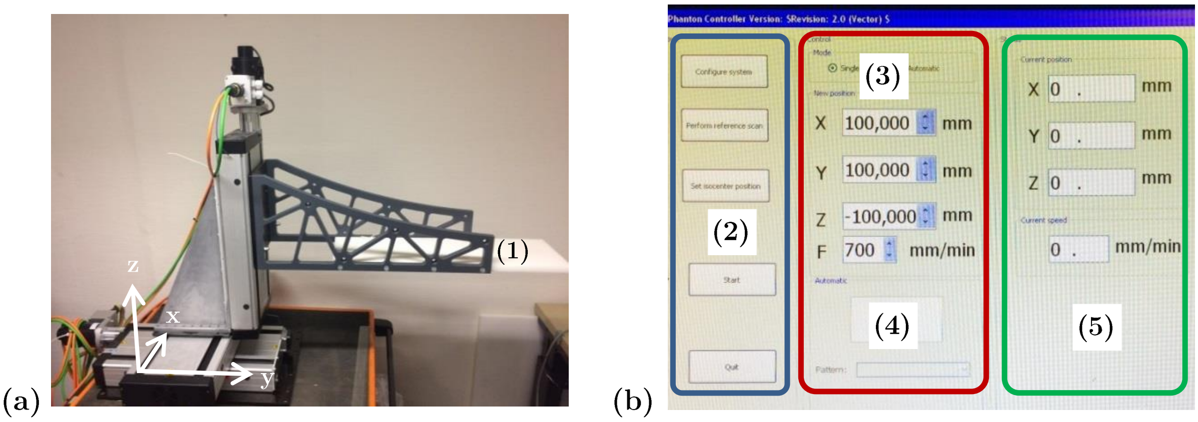

Mode: ● Single ○ Automatic

New position:
X 100,000 mm
Y 100,000 mm
Z -100,000 mm
F 700 mm/min

Current position:
X 0 . mm
Y 0 . mm
Z 0 . mm

Current speed: 0 . mm/min

Figure 8. (a) The motion robot that can move in x-, y- and z-directions by means of three independent motors. The phantom is placed on the front part of an extension plate (1). (b) Graphical user interface (GUI) of the in-house developed motion robot control software. The control unit (2) is used to perform different robot motion protocols (e.g. reference scan, isocenter positioning). The robot can be moved either manually (3) or by means of externally provided files (4). Current coordinates and speed is shown in (5).

2.2.3 *Dynamic porcine lung phantom*

The dynamic porcine lung phantom (see Figure 9(a)) has previously been used for several radiological experiments that include dynamic 4D-CT and MRI experiments (Biederer and Heller 2003). This includes investigation of tumor motion patterns that were simulated by means of agarose-gel (Biederer *et al* 2009) directly injected into the porcine lung. As the phantom setting is well-described in literature, only a brief description will be given here. The corpus of the dynamic lung phantom consists of a double-walled PMMA shell (wall distance 2 – 5 cm), in which a post-mortem explanted porcine lung is inserted. A realistic attenuation during irradiation is achieved by filling the shell with water. To reduce the development of alga, 1.25 g/L Nickel-Sulfate is added.

An under-pressure of approx. -20 to -30 hPa within the phantom corpus is applied to realize inflation of the inserted lung by means of an on-board vacuum pump (VP0940, Nitto Kohki GmbH, Steinenbronn, Germany). The diaphragm is simulated by a water-filled silicon balloon located inferior to the lung. This allows changing the porcine lung volume by varying the pressure inside the artificial diaphragm by means of a computer-controlled air flow unit. Different breathing patterns can be applied that are comparable to those measured in patients.

Fresh porcine lungs were obtained from a slaughtery 2-3 hours prior to the experiment. They include the heart, trachea and esophagus to achieve a realistic image contrast. Before inserting the lung into the PMMA shell, the quality had to be checked first. This includes checking for elasticity, gas tightness and size of the inflated lung. The *gel tumor* was then sewed to the mediastinum by means of a special mount (see Figure 9(b)). As the inflation of the lung requires a continuous air flow through the PMMA shell, the inner wall, the silicon bladder and porcine lung were treated with ultrasound gel (P.J. Dahlhausen & Co. GmbH, Cologne, Germany) to ensure smooth and continuous lung motion during the experiment.

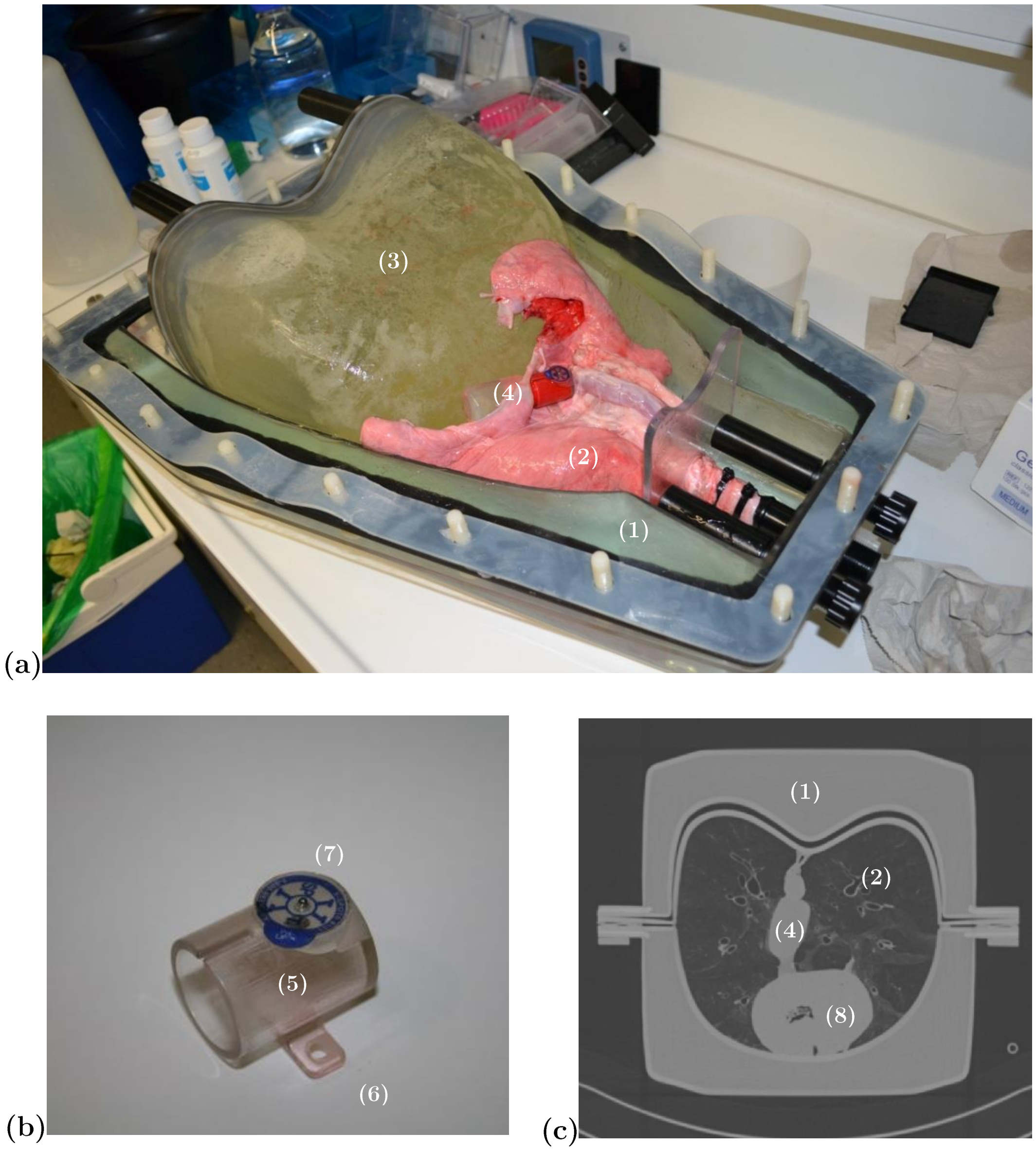

Figure 9. (a) The water-filled corpus of the dynamic lung phantom consists of PMMA (1) and contains a fresh porcine lung (2). A water-filled silicon-balloon (3) is located at the lower part of the phantom and is used to apply pre-defined motion pattern to the lung located superior to a water-filled silicon-balloon (3), which is used to apply arbitrary breathing patterns to the lung. The PGD (4) is sewed to the mediastinum of the lung. (b) The PGD holder (5) incorporates two eyelets (6) which are used for sewing the holder onto the lung. It additionally holds a CT marker (7) which is used for image registration later. (c) A transversal CT image of the closed phantom which is acquired for treatment planning. In this experiment, the PGD (4) is located anterior to the heart (8).

As the on-board vacuum pump requires a high-voltage power supply, it had to be switched off for the transport of the phantom (e.g. from planning CT to the LINAC). To prevent the lung from collapsing, the under-pressure system was connected to an external vacuum pump (Accuvac Rescue, Weinmann Geräte für Medizin GmbH + Co. KG, Hamburg, Germany) with a portable battery. For that, the on-board system was switched off.

2.3 3D polymer gel dosimetry

Quality control and workflow verification in modern adaptive RT should also be able to perform dosimetric measurements. Standard measurements are usually performed in 1D (e.g. by ionization chambers (IC) or diodes) or in 2D using films (Ehrbar *et al* 2016). However, this is not possible for the lung phantom setting as the insertion of either films or an IC is not feasible. In addition, films provide only 2D rather than 3D information. By using the porcine lung phantom, an ideal dosimeter should be able to (i) measure dose in 3D while (ii) showing a tissue or water equivalent image contrast and (iii) be placed at different positions within the phantom without changing the phantom dynamics. A very promising dosimeter meeting requirements (i) – (iii) which is currently used only for research purposes, is the application of polymer gel dosimeters (PGD). PGD have shown to be a suitable method to measure 3D dose distributions (Schreiner 2006) and has been applied to measure dose distributions from intensity-modulated radiation therapy (Vergote *et al* 2004, Sandilos *et al* 2004) as well as to acquire the delivered dose in presence of respiratory motion (Ceberg *et al* 2008). In addition, it exhibits both, water-equivalent image contrast and attenuation properties. Gel dosimetry is therefore a versatile tool that can be used to measure the delivered dose distribution in such an experimental setting. The following sections provide an introduction to the general principles, fabrication and irradiation procedures of PGD as well as the developed evaluation procedure. For a more detailed description on polymer gel dosimetry the reader is referred to the topical review of Baldock *et al.*

2.3.1 *General principle*

Polymer gel dosimeters are fabricated from radiation sensitive chemicals embedded within a gelatine matrix which, upon irradiation, polymerize as a function of the absorbed radiation dose. This polymerization process locally changes material specific constants like the T_2 relaxation or optical density. These changes can be measured by MRI (Baldock et al. 2010) or CT (Jirasek and Hilts 2014), respectively. Due to the larger polymer structures as compared to the pore size of the gelatine matrix, dose information stays locally bound (Baldock *et al* 2010). In general, polymer gel dosimetry is especially interesting, if the dose measurement intends to acquire spatial information in 3D as well as for irradiation setups where steep dose gradients are present, e.g in IMRT or stereotactic surgery (Vandecasteele and De Deene 2013a, Papagiannis *et al* 2005). To perform absolute dose measurement, the PGD requires a set of calibration samples that are irradiated with known doses. This calibration method needs to be repeated for each batch of PDG (Venning et al. 2005). It should be mentioned that the application of PGD is challenging and time-consuming as a specific workflow needs to be followed between gel fabrication and evaluation. The entire workflow from production to evaluation takes approx. four days. It is also very important to minimize the influence of external factors such as oxygen contamination of the gel as this would significantly impact the polymerization process (De Deene *et al* 2002). However, if a dedicated protocol for fabrication, storage, irradiation and evaluation is applied, polymer gel dosimetry is a versatile tool for 3D-dose measurements

A large variety of different PGD is described in literature. These are made of various radiosensitive chemicals of different concentration. This work focuses on two kind of PGD, (i) the commercially available Pre *BANG-kit* (MGS Research, Inc. Madison, USA) and the in-house produced

PAGAT dosimetry gel (PolyAcrylamide Gelatine gel fabricated at ATmospheric conditions (Venning et al. 2005)). As the commercial solution allows to easily fabricate the polymer gels by following an optimal and well-established protocol, initial measurements were focused more on the irradiation- and evaluation workflow. However, due to the superior properties of the PAGAT gel dosimeter in terms of dose-rate dependence (De Deene *et al* 2006, Karlsson *et al* 2007), easier evaluation protocols and lower costs, the Pre BANG-kit was replaced by the PAGAT dosimetry gel.

2.3.2 *Fabrication*

A short introduction into the fabrication procedure for both, the commercially available BANG-kit and the in-house produced PAGAT, will be given in the following section. Both dosimetry gel production procedures follow similar protocols, starting with the separate preparation of monomer- and gelatine solution, followed by the mixing- and the filling procedure. The interested reader will find a detailed description of the protocol in Appendix A. The chemical composition of the different gel dosimeters will be given in the following.

Pre BANG-kit: This type of dosimetry gel is based on monomers (not more than 6% methacrylic acid or sodium methacrylate) as active components embedded within a gelatine matrix consisting of gelatine (not more than 6%, 300 bloom), a nontoxic thickening agent (not more than 12%), deionized water (at least 70%) and an oxygen scavenger (no further information available). A description of the exact chemical concentration is not provided by the vendor.

PAGAT: This type of dosimetry gel is based on monomers (3% acrylamide and 3% N,N-methylene-bis-acrylamide as active components embedded within a gelatine matrix (6% Gelatin, 300 bloom, Sigma Aldrich, St. Louis, MO, USA) and 88% deionized water. Due to its high reactivity to oxygen penetrating the gel during production and storage, 10 mM bis[tetrakis(hydroxymethyl)-phosphonium] chloride (THPC) is added as antioxidant.

2.3.3 *Gel containers*

After production, the gel was poured into suitable storage containers (Section 2.4) at a temperature of 32 °C. Prior to this, all containers were rinsed with nitrogen gas to remove the oxygen. To further reduce the potential impact of oxygen on the gel response, all containers were placed inside a desiccator flushed with nitrogen for 5 min and were then stored in a refrigerator at 4 °C for 20-24 h before the gel was irradiated (Vandecasteele & De Deene 2013c). To minimize the influence of light as an additional cause of polymerization (Koeva *et al* 2009) the flasks were covered with aluminum foil during storage.

2.3.4 *Irradiation*

At the day of irradiation, the PGD were removed from the refrigerator 4 h prior to irradiation and transferred to the irradiation facility. The PGD were irradiated at room temperature with a clinical 6 MV linear accelerator (Artiste, Siemens Healthineers, Erlangen, Germany) at a dose rate of 300 monitor units per minute (MU/min). To acquire the calibration curve for the gel, the calibration flasks were subsequently irradiated with doses from $0 - 7\ Gy$ in steps of $1\ Gy$. These irradiations were performed under reference conditions at room temperature inside a $30 \times 30 \times 30\ cm^3$ stationary cubic water phantom (T4322, PTW, Freiburg, Germany) using a field size of 10 × 10 cm^2 at a depth of 5 cm and a gantry angle of 270°. At the end of the experiment, the PGD were enwrapped in aluminum foil and stored together with the calibration flasks at room temperature for at least 48 h prior to MRI-evaluation.

2.3.5 *MR-based evaluation*

Quantitative polymer gel evaluation can be realized using a large variety of different devices. All these methods measure locally-dependent radiation-induced chemical or physical changes within the polymer gel. A commonly used and widely accepted method is to measure the mobility of water protons surrounding the polymerized gel structure using MRI. Alternatively, changes in optical density can be measured by optical CT devices, variations in mass density may be visualized by X-ray CT or ultrasound measurements can detect changes in acoustic propagation speed. A detailed description of each acquisition method is not within the scope of this work, but can be found elsewhere (Baldock *et al* 2010). In this work, quantitative 3D dose evaluation was realized using MRI. As the MR image acquisition is a crucial part of the polymer gel dosimetry evaluation procedure, a brief description to the applied MR image acquisition technique will be given in this section. This is then followed by a detailed description of the polymer gel dosimetry evaluation procedure including an analysis of the impact of MR-based errors on quantitative 3D dose distribution and how these can be minimized.

2.3.5.1 MR – Basic principles

A short overview on MR-basics and its importance for polymer gel dosimetry will be given in this section. A detailed description, on the physical principles of magnetic resonance imaging, however, is not within the scope of this work. For this, the reader is referred to the book from Haacke *et al* 1999.

Magnetic resonance imaging is a tomographic imaging modality, which uses non-ionizing radiation to acquire images with an excellent soft tissue contrast. Major applications include the musculoskeletal system, brain tumors, spinal cord and imaging of the abdomen (Reiser *et al* 2008). The physical principle of MRI is based on the nuclear spin I, which is different from zero for nuclei with an uneven number of protons and/or neutrons. In the presence of an external static magnetic field B_0, the spins start to align parallel or anti-parallel. According to the Boltzmann statistics, the parallel spins exceed the number of anti-parallel spins. As a result, this leads to a measurable time independent macroscopic net magnetization or polarization P (e.g. for protons: $P = 1{,}67 \times 10^{-6}$ at $T = 293\ K$ and $B_0 = 3\ T$). According to *Faraday´s Law*, however, only a time dependent magnetization component can be measured. This can be realized by applying a time dependent radio-frequent (RF)- field $B_1\ t$ to the system which causes the equilibrium occupation of parallel and anti-parallel spins to change. An RF-pulse, which is applied perpendicular to B_0, rotates the net magnetization around the x- or y-axis towards the $x - y$-plane. The corresponding flip angle α of the magnetization can then be calculated by:

$$\alpha = \int_0^{t_p} \gamma B_1\ \tau\ d\tau \tag{2.1}$$

with the gyromagnetic ratio γ, the time dependent RF amplitude $B_1 \ \tau$ and the pulse duration t_p. In case of a static B_1, Equation (2.1) simplifies to $\alpha = \gamma B_1 t_p$. As the resulting magnetization signal starts to decay, the transversal magnetization becomes time-dependent and can be measured by a receiver coil. This decay process is driven by: (i) the spin-lattice-, (ii) spin-spin interactions, and (iii) by local field inhomogeneities. While (i) causes transitions of the polarized spins towards the equilibrium state, (ii) and (iii) lead to a dephasing of the spins in the transversal plane. All processes are characterized by material specific relaxation times T_1, T_2 or T_2^*, respectively. By using a sequence of RF-pulses of different length, direction and power, a large variety of image contrasts can be achieved. In case of polymer gel dosimetry, the irradiation-induced polymerization leads to changes of the absolute T_2 values. The aim of the polymer gel dosimetry evaluation is therefore to quantitatively measure this value and convert it to absolute dose values.

A very prominent and widely used method to acquire quantitative T_2-images is to perform a so-called spin-echo (SE) experiment. It consists of a 90° excitation pulse that rotates the z-component of the macroscopic magnetization M_z into the transversal plane. Both, local field variations and spin-spin interactions cause the transversal magnetization M_{xy} to decay. This so called *free induction decay* (FID) can be measured by the receiver coil. By applying a 180° - refocusing pulse at time $t = \tau$, spin dephasing due to local field inhomogeneities is reversed and results in rephasing of the spins at the time $t = 2\tau$, which leads to a maximum signal intensity ("spin echo"). The decrease of this maximum signal intensity over time is then mainly governed by the spin-spin relaxation time T_2. Applying a series of multiple 180° pulses allows acquiring the spin echoes at times $t = 4\tau$, $t = 6\tau$ and so on. The decrease in signal intensity of the multiple SE-echo signals can then be fitted against a mono-exponential function with the T_2-relaxation rate as characteristic decaying constant:

$$\mathrm{S} = \mathrm{S}_0 \mathrm{exp}^{-\frac{TE}{T_2}}, \tag{2.2}$$

where S_0 is the initial signal intensity and the echo time (TE) is the time between two consecutive echoes. In principle, two SE are sufficient to acquire quantitative T_2 values, however, it was shown that a set of multiple SE measurements is preferable for the polymer gel dosimetry evaluation procedure to achieve a better dose resolution (De Deene and Baldock 2002) and a lower signal to noise ratio (SNR) (De Deene *et al* 1998). In this work, a standard Carr-Purcell-Meiboom-Gill sequence (CPMG) (Meiboom and Gill 1958) with a fixed number of 32 consecutive echoes was used (see Figure 10). After the repetition time (TR) the multi-SE experiment is repeated with a new 90 ° excitation pulse to acquire sufficient data for image reconstruction.

2.3.5.2 MR and polymer gel dosimetry – potential error sources

Besides errors that may occur during the PGD production procedure or irradiation, the MR acquisition can introduce additional uncertainties in absolute T_2 measurement. The largest influence on quantitative T_2 measurement is caused by temperature variations, which can arise during very long MR measurements due to energy deposition by the alternating RF-field inside the evaluated phantom (De Deene and De Wagter 2001), temperature differences between phantoms of different volumes or within very large phantoms if no dedicated measures for temperature control are taken. As temperature variations have a major impact on the proton mobility and therefore on the spin-spin interaction process, T_2 is strongly influenced. Increasing the temperature will result in larger T_2 values and vice versa (Vandecasteele and De Deene 2013d). This is especially problematic, if a temperature gradient e.g. within larger phantoms is present as this would result in a spatially distributed T_2 values, even for phantoms where a homogeneous T_2 distribution is expected (e.g. for uniformly irradiated phantoms). In addition, even if a constant temperature can be assured within the large phantom, temperature differences with respect to the calibration containers would also cause errors in the absolute dose determination.

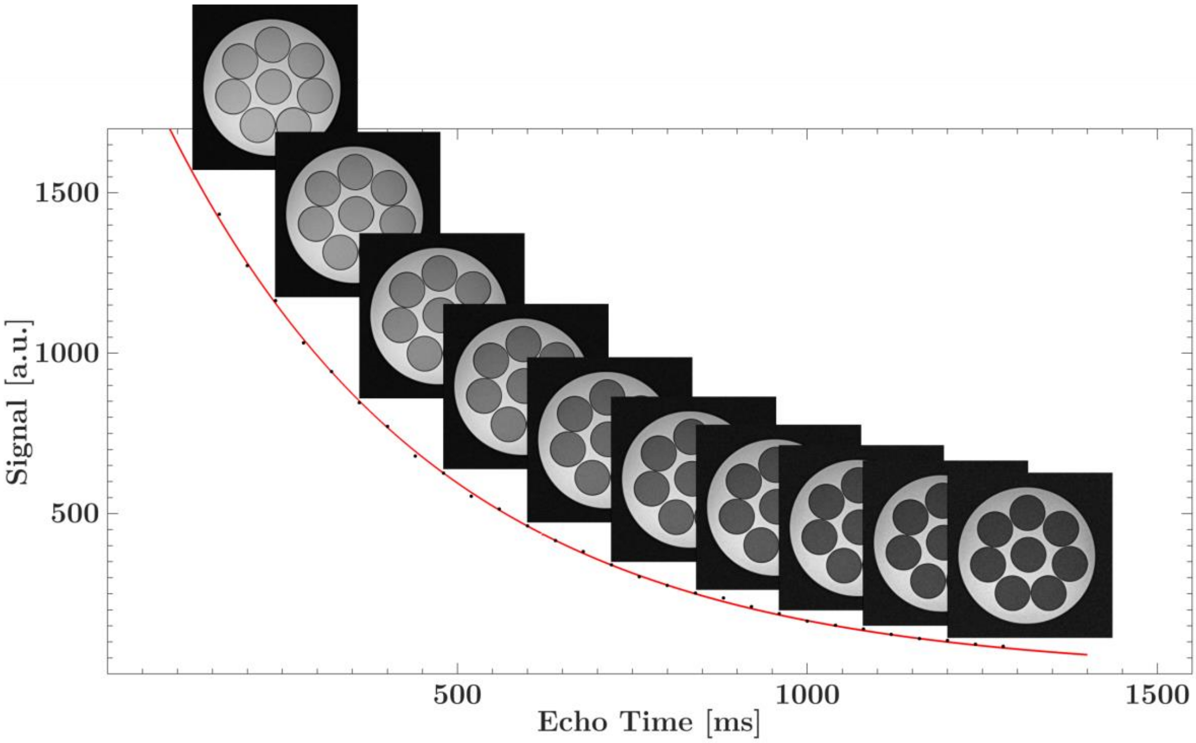

Figure 10. CPMG multi-SE acquisition for 32 consecutive echoes, with $TE = 40\ ms$ and $TR = 3\ s$. The signal intensity for one representative ROI is plotted against the echo number TE and fitted against a mono-exponential function.

As an additional error source, inhomogeneities of both, the static B_0-, and time dependent B_1-field may introduce errors. While uncertainties in B_0 potentially cause the spatial information to be shifted by several pixels (Vandecasteele and De Deene 2013d) a non-uniform slice excitation pattern due to B_1-field inhomogeneities can result in T_2 deviations of up to 20% as compared to the real value (De Deene *et al* 2000). This effect is especially pronounced for the peripheral region of larger phantoms.

Besides this, as the visualization of steep dose gradients over a 3D volume is desirable for the purpose of 3D dose measurements, the correct choice of imaging parameters is essential to acquire high-resolution images (down to voxel sizes (VS) of $1 \times 1 \times 1\ mm^3$) with a large signal to noise ratio (SNR). As a result, the imaging parameters TE and TR were optimized with respect to the applied radiation plan and the total MR acquisition time. This is especially important as the choice of suboptimal parameters can significantly influence the accuracy of PGD (De Deene and Baldock 2002)

In summary, it should be kept in mind that uncertainties in polymer gel dosimetry do not only originate from the production- or irradiation protocol, but also from the MR image acquisition, if no dedicated MR protocol is applied.

2.3.5.3 Evaluation of the polymer gel dosimeters

Calibration- and *gel tumor* flasks were scanned simultaneously on a 3T Biograph mMR (Siemens Healthineers, Erlangen, Germany) using specially designed adapter plates for both, calibration flasks and *gel tumor* (Figure 11(a) and (b)). The holder was placed inside a dedicated temperature controlled water phantom (Section 2.4.2) which was placed at the center of a 16-channel head/neck RF coil. Relaxation rate images were acquired in a transversal plane with a multi-SE CPMG sequence. Calibration flasks were scanned twice, at the beginning and the end of the session. This allows identifying any measurement-related T_2 variations that occur during the scan. For volumetric *gel tumor* scanning between 15 and 28 slices were measured using identical imaging parameters as for the calibration flask. A comparison between MRI-based PGD dose measurement and TPS-based dose calculation requires image registration between MR and planning CT (see 2.2.5, image registration). This was realized by acquiring an additional high-resolution (0.5 × 0.5 × 0.5 mm^3) 3D-image of the *gel tumor* using a standard TRUe Fast Imaging with Steady Precession (TRU-FISP) sequence as implemented by the vendor.

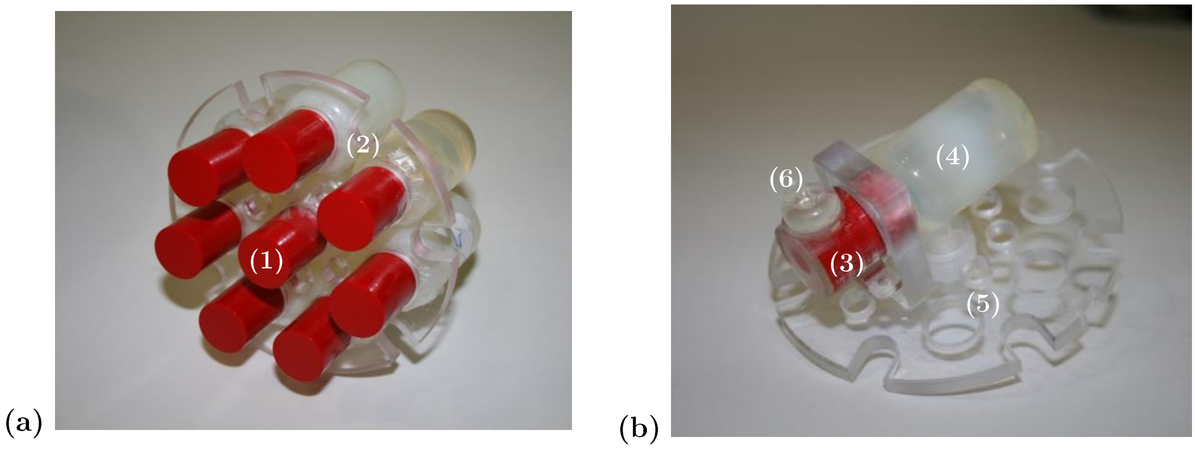

Figure 11. (a) Eight calibration flasks (1) were equally distributed using a dedicated PMMA holder (2). (b) The mounting (3) of the *gel tumor* (4) is attached to an adapter plate (5) and the metal fiducial is replaced with high accuracy (<1 mm) by an MRI-visible marker (6) using a special template.

2.3.6 *Calibration of the dosimetry gel*

To perform absolute dose measurements in 3D, the *gel tumor* T_2 maps need to be calibrated using a set of calibration vessels. As external influences on the production procedure can not completely be avoided (Vandecasteele and De Deene 2013b), a calibration is necessary for each experiment.

For the evaluation of the calibration vessels, MR data was transferred to a personal computer and imported into an in-house developed, Matlab (The Mathworks Inc., Natick)-based polymer gel dosimetry evaluation tool (Witte 2010). For each calibration vessel, a circular region-of-interest (ROI) was automatically delineated with a *canny* segmentation algorithm (Canny 1986). To acquire mean T_2 maps and the related standard deviation for each gel probe, a mono-exponential curve was fitted to 29 of the 32 acquired MR-images using a Levenberg-Marquard X^2 -minimization algorithm (Marquardt 1963). Due to stimulated echoes that can occur during the quantitative T_2 measurement (Hennig 1991), the first three images were not included in the fitting procedure. Based on the calibration flasks, the calibration curve was then determined from the calculated mean relaxation rate $R_2 = 1/T2$-values. The PAGAT dosimetry gel was fitted using a mono-exponentially saturated dose-dependent fit function (Vandecasteele and De Deene 2013a):

$$\mathrm{R}_2(\mathrm{D}) = \mathrm{R}_{2,\mathrm{sat}} - \Delta\mathrm{R}_2\mathrm{e}^{-\alpha\mathrm{D}} \tag{2.3}$$

where $R_{2,sat}$ corresponds to the saturation relaxation rate, ΔR_2 to the range of R_2 values and α being the fit coefficient of the exponential function. The basic calibration procedure is visualized in Figure 12.

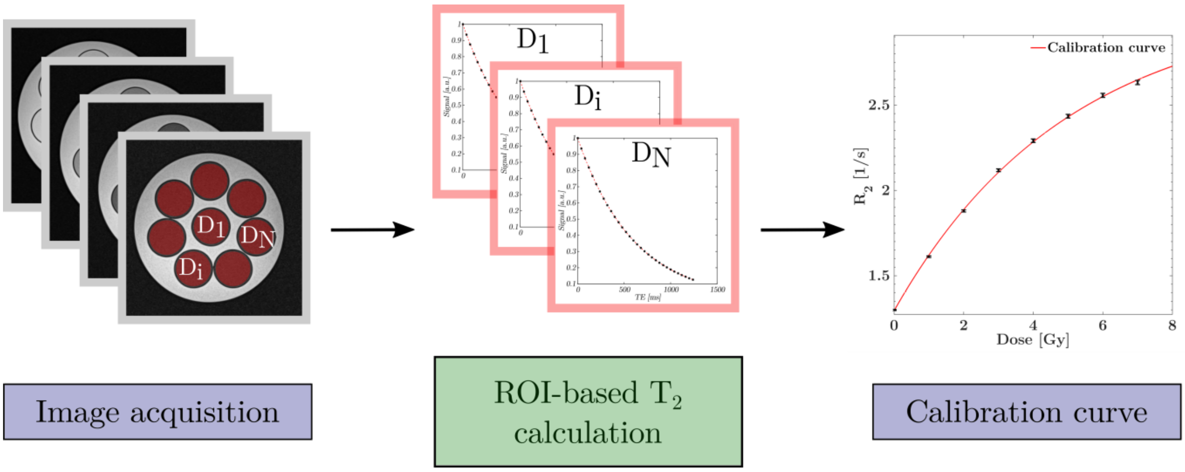

Figure 12. Calibration workflow of PAGAT-based PGD. Calibration vessels were irradiated with well-known doses between 0 and 7 Gy and subsequently measured at the MR to acquire quantitative T_2 images (left). Based on an automated segmentation algorithm, mean T_2values were calculated (middle) within different ROIs D_i. The corresponding dose was then related to the R_2 and fitted by a mono-exponential function (right).

2.3.7 *Image filtering*

One of the major challenges in quantitative MRI acquisition is noise reduction as it can significantly influence quantitative data evaluation. This is especially pronounced if a pixel-wise quantitative evaluation is necessary since averaging over a larger area is not desired in 3D dosimetry. In addition, if a non-linear conversion between the relaxation rates and doses by means of a calibration curve are necessary, the influence of noise depends on the absolute measured values. One option of noise reduction is to modify the measurement procedure by averaging over a larger period of time or by increasing the voxel size. However, if the measurement volume is rather small and the resolution of steep gradients is important, an increase in voxel size is not desirable. A suitable image filtering procedure is therefore a very important step towards quantitative 3D dose measurements. The applied filter should (i) reduce the noise level within regions of constant intensities while ensuring that (ii) steep gradients are not smeared-out. In this work an edge conserving total variation (TV) filter was used (Rudin *et al* 1992).

The TV of an image y is defined as the sum of the difference between two neighbouring pixels.

$$TV\ \ y \ = \sum |y_{n+1} - y_n| \tag{2.4}$$

which is minimized while assuming that the new image is similar to the initial one. A similarity measure, which is proposed for this algorithm, is given by the sum of square errors:

$$S\ \ x, y \ = \frac{1}{2} \sum \ x_n - y_n \ ^2 \tag{2.5}$$

where x_n is the unfiltered image data and y_n corresponds to a similar image with smaller total variation. Combining Equations (2.4) and (2.5) leads to the following minimization problem

$$\min_y \ S\ \ x, y \ - \lambda\ TV(y) \tag{2.6}$$

with the regularization parameter λ, which can then be solved by using the Euler-Langrange equation. A one-dimensional example dataset with and without TV-filtering is displayed in Figure 13.

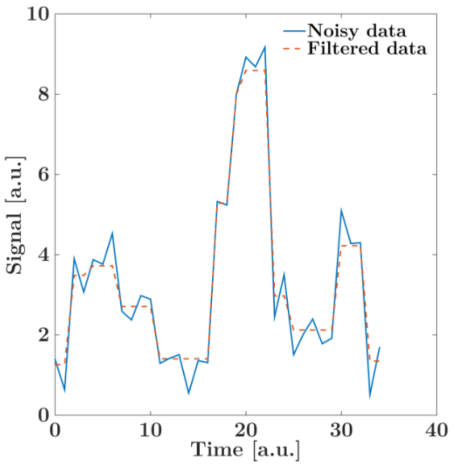

Figure 13. The data shows an arbitrary signal (blue) which was filtered by a TV filter (orange). The resulting filtered signal clearly shows less noise while steep gradients or edges are still maintained.

2.3.8 *Spatial alignment of the measured and planned dose distribution*

As the MR evaluation was not performed inside the phantom which was used for treatment planning and irradiation, both dose distributions had to be spatially aligned. This was realized by co-registering CT- and high-resolution MR images by means of three uniquely defined landmarks on the surface of the *gel tumor*: (i) the center of the lid, (ii) the center of the bottom and (iii) a previously attached marker. Both, (i) and (ii) could be geometrically reconstructed. For a uniquely definition of (iii), two kinds of fiducial markers were used (X-Spot for the CT- and a PinPoint$^{\text{TM}}$ MR-marker for the MR-measurement, Beekly Medical, Bristol, USA). Corresponding markers were attached to the *gel tumor* mounting before inserting the *gel tumor* into the phantom by means of a special template (Figure 11(b)) that allows replacing the CT marker by the MR marker with high accuracy. The registration was performed on the image processing platform MITK (Nolden *et al* 2013) together with a point-based *RigidClosedFrom3D* b-Spline 3$^{\text{rd}}$ order interpolation algorithm as implemented by the software. This registration procedure will be referred to as standard marker based point registration (SMR).

A schematic sketch of the registration procedure is shown in Figure 14. As the measured dose distribution includes only a limited sensitive volume as compared to the calculation, a threshold-based delineation was applied to the *gel tumor* volume. It was ensured that both, the flask wall and clearly visible dose errors, caused either by the PGD or MR (such as gas- bubbles or imaging artefacts) were not included in the delineated volume.

2.3.9 *Renormalization of the calibration curve*

In general, the challenge of gel dosimetry is to perform dose measurements in an absolute manner. However, this is rather challenging as there are various factors that influence the gel response. These factors are not only limited to the production procedure (Vandecasteele and De Deene 2013b), gel storage or irradiation (Vandecasteele and De Deene 2013c) but also show a very sensitive behavior on the evaluation process (De Deene and Vandecasteele 2013). This makes polymer gel dosimetry a very challenging technique for absolute dose measurement in 3D. There is a large variety of reports on how to perform polymer gel dosimetry, but most of the published work focuses on relative dosimetry. Furthermore, in contrast to our experimental setting, most experiments were performed under well-defined conditions. Combining polymer gel dosimetry with the porcine lung phantom might introduce further, yet unknown uncertainties. Therefore, the acquired calibration curve was renormalized as described by Vandecasteele and De Deene which is especially useful for small volumetric phantoms like the *gel tumor*. Renormalization is carried-out by using the mean doses in two uniform low- and high-dose regions. As the small *gel tumor* volumes do not show a uniform low-dose region, only the information inside the high-dose region was used for renormalization. For this, a manually segmented ROI within the *gel tumor* was normalized either (i) to the measurement of an ionization chamber which is located at the same position, or (ii) a corresponding ROI was defined in the treatment plan, if it was not possible to perform an ionization chamber measurement (e.g. inside the porcine lung phantom).

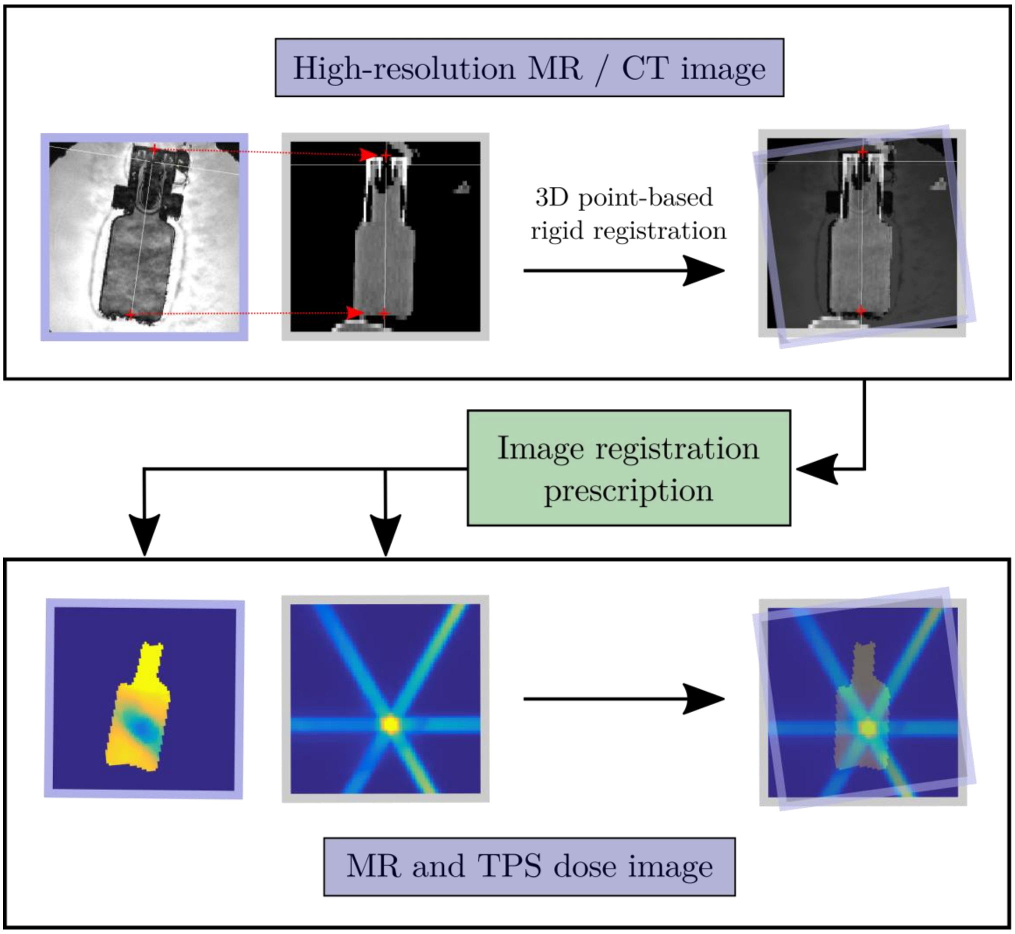

Figure 14. Standard Marker based point Registration (SMR). Corresponding reference points are defined in both, the high-resolution MR and the CT images. A 3D point-based rigid registration is performed, stored and subsequently applied to the dose image of both, TPS and MR.

The previously acquired calibration curve (Section 2.3.6) was then renormalized such that the original shape was preserved while the new fit parameters $R'_{2,sat}$ and $\Delta R'_2$ were calculated from Equation (1) as follows:

$$\Delta R'_2 = \frac{R_{2,0} - R_{2,1}}{e^{-\alpha \cdot D_1} - 1} \tag{2.7}$$

$$\mathrm{R}'_{2,\mathrm{sat}} = \Delta \mathrm{R}'_2 + \mathrm{R}_{2,0} \tag{2.8}$$

D_1 corresponds to the mean value inside the high-dose ROI of the IC measurement or TPS calculation and $R_{2,1}$ to the measured R_2 data within the same ROI. $R_{2,0}$ is the intersection of the original calibration curve with the y-axis and is defined by

$$R_{2,0} = \mathrm{R}_{2,\mathrm{sat}} - \Delta R_2 \tag{2.9}$$

As for experiments with steep dose gradients performed inside the porcine lung phantom no IC could be inserted and only a small high-dose area (Section 2.5.4 and Section 2.5.5) is present, the renormalization coefficients $R'_{2,sat}$ and $\Delta R'_2$ were calculated using the maximum rather than the ROI-based mean values for D_1 and $R_{2,1}$.

2.3.10 *Calculation of the 3D dose distribution*

The final dose distribution was acquired by subsequently converting the R_2-map of the *gel tumor* into a dose map by means of the renormalized calibration curve.

2.3.11 *Gamma index analysis*

The validation of a three-dimensional dose distribution requires a comparison between the TPS-based calculation and the measured data. A well-established and widely used method in clinical quality assurance (Schreiner 2006, Oldham *et al* 2012, Bakai *et al* 2003)) was developed by Low *et al.* This method uses a combination of two independent evaluation techniques: (i) the local dose-difference criterion ΔD_M and (ii) the distance to agreement (DTA) criterion Δd_M. The dose-difference criterion calculates the absolute dose difference between measurement and calculations in areas of uniform dose distribution (low dose-gradients). In the presence of large dose-gradients, however, a small position shift of the measured dose would cause the dose-difference criterion to fail. To compensate for that, the DTA is used as quality index. It requires the calculated dose to be located around the measured dose within a certain radius Δd_M. It was therefore concluded that a combination of both methods ideally complement each other in regions of low- (i) and high dose gradients (ii), respectively.

The evaluation procedure is performed by evaluating a set of calculated data points $D_C(r_c)$ that are located at a distance

$$r \;\; r_m, r_c \;\; = |r_c - r_m| \tag{2.10}$$

around the measured data point $D_m(r_m)$. Subsequently, the dose difference $\delta \;\; r_m, r_c$ is calculated:

$$\delta \;\; r_m, r_c \;\; = D_c(r_c) - D_m(r_m). \tag{2.11}$$

The suggested acceptance criterion taking both, dose-difference and DTA into account can then be visualized by an ellipsoidal surface

$$\mathrm{T} \;\; r_m, r_c \;\; = \sqrt{\frac{r^2 \;\; r_m, r_c}{\Delta d_M^2} + \frac{\delta^2 \;\; r_m, r_c}{\Delta D_M^2}} \tag{2.12}$$

where ΔD_M and Δd_M are defined as the acceptance threshold for the maximum dose-difference and DTA, respectively.

A quantitative value for a single measurement at position r_m that allows describing the agreement between measured and calculated dose distribution can be defined by the gamma-index:

$$\gamma \;\; r_m \;\; = \min\{T \;\; r_m, r_c \;\; \} \, \forall \{r_c\} \tag{2.13}$$

With this definition, the passing criteria becomes

$$\gamma(r_m) \leq 1, \text{ calculation passes,} \tag{2.14}$$

$$\gamma(r_m) > 1, \text{ calculation fails.} \tag{2.15}$$

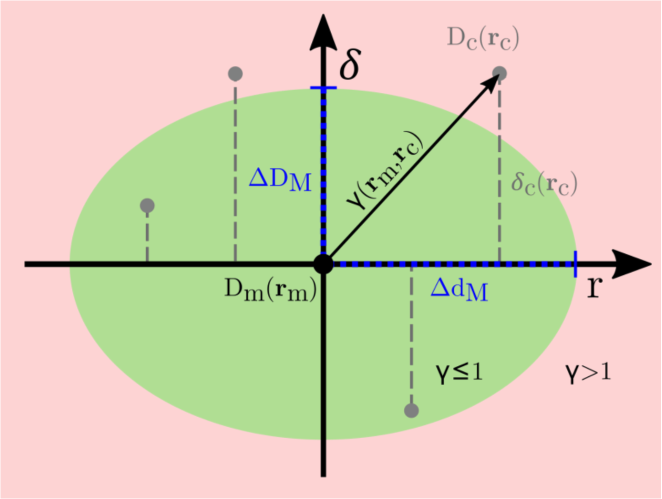

Figure 15. Basic principle of γ-map analysis exemplified in 1D. A measured point $D_m(r_m)$ is compared against a calculated data point $D_c(r_c)$. Calculated points are only evaluated within a radius Δd_M. In addition, a threshold ΔD_M for the dose difference $\delta_C(r_C)$ is defined. If a single evaluated point is located within the green area ($\gamma \leq 1$) the $\gamma-$map analysis is passed for $D_m(r_m)$.

A schematic visualization of the principle of γ-index calculation in 1D is displayed in Figure 15. The calculated and measured dose distributions were compared using the 3D γ-map analysis as implemented by the commercial software VeriSoft (PTW, Freiburg, Germany). A passing criterion of 3% / 3 mm (dose-difference / DTA) was used, taking only dose levels > 10% of the maximum dose into account. The dose threshold of 10% was selected as dose calculation algorithms at this dose level are less accurate on the one hand, but also clinically less relevant on the other. Results in this thesis are given as passing rates, i.e. the percentage of evaluated points passing the γ-criteria. Voxels presenting clearly visible image artifacts (e.g. caused by the MR image acquisition or dosimetry gel based errors) were excluded from the evaluation procedure.

In case of small field irradiations, γ-map analysis was performed for two different settings. First, only the SMR was performed prior to the γ-calculation. As residual positioning errors may strongly affect the agreement for small dose distributions, an additional automated post registration (APR) as implemented by the VeriSoft-software was applied to correct for these errors to determine the maximum possible agreement.

2.3.12 *Workflow summary*

As the polymer gel dosimetry evaluation procedure requires a large number of steps, the developed workflow is briefly summarized: For a detailed description the reader is referred to Section 2.3.5 - 2.3.11. In principle, the evaluation procedure can be divided into six sub-steps (Figure 16): After acquiring quantitative T_2 images by means of an MR measurements using a dedicated temperature control protocol, a voxel-wise T_2 calculation is performed. Noise removal is achieved by applying an edge conserving TV filter. As a next step, high-resolution images of both, CT- and MR-data are consecutively registered using a point-based registration. This registration procedure is then applied to spatially correlate the measured to the calculated dose distribution. The measured calibration curve is then renormalized by means of a point-dose measurement or a high-dose region within the calculated dose distribution before converting the R_2-map into dose. As a last step, measured and calculated dose distributions are compared using the 3D γ-evaluation procedure.

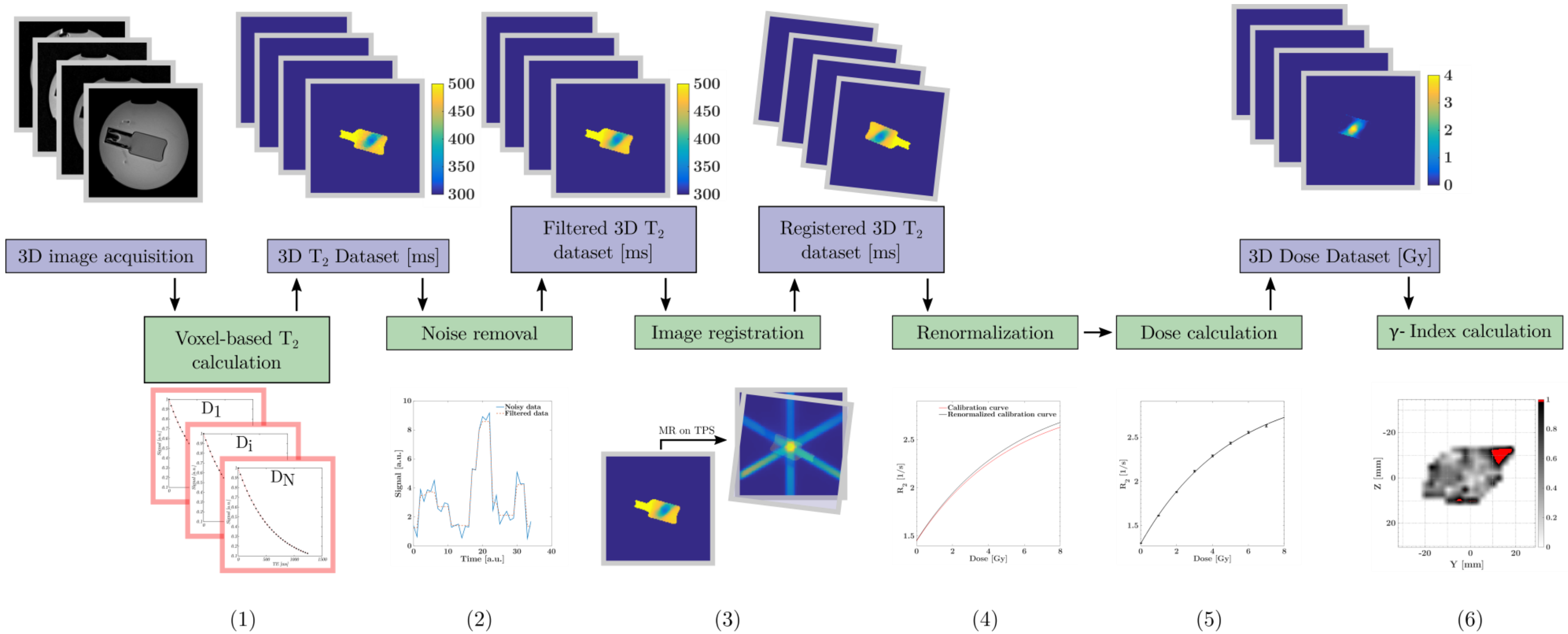

Figure 16. Schematic overview of the implemented polymer gel dosimetry evaluation workflow which can be summarized in six different sub-steps: (1) T_2 calculation, (2) noise removal, (3) registration (4) renormalization, (5) dose calculation and (6) dose comparison.

2.4 Polymer gel characterization

As polymer gel dosimetry is still not implemented into the clinical routine and therefore not implemented as a standard workflow in our institution yet, the PGD handling in terms of production, storage, irradiation, evaluation and post-processing was thoroughly investigated. PGD irradiation was performed inside the water-tank which is used for gel calibration purposes with known doses from $0-7\ Gy$ in steps of $1\ Gy$ with a field size of $10 \times 10\ cm^2$ and a dose rate of $300\ MU/min$ if not stated otherwise.

2.4.1 *Gel container materials*

Besides the well-known polymerization inhibition characteristics of oxygen penetrating the container wall, chemical interactions of the PGD with the wall material are known to influence the dose response (Baldock *et al* 2010, Vandecasteele and De Deene 2013d, Mann *et al* 2015). Therefore, the selection of an adequate flask material was considered highly critical. A suitable gel storage container for our application should meet the following requirements: (i) excellent oxygen barrier, (ii) limited interactions with the PGD (iii) water equivalent image contrast for CT images (iv) tumor equivalent size and shape, and (v) should only show a minor influence on motion properties of the lung within the phantom. Several containers of different volumes were investigated and characterized, namely latex, silicon, borosilicate glass and BAREX^{TM} material. Initial measurements were performed with the commercially available BANG-kit^{TM} as they were the only dosimeters available at the beginning of the project. However, in the process of investigating the compatibility with the above requirements the PAGAT dosimetry gel turned out to be better suited for the purpose of the project. Nonetheless, the results of the investigations of the BANG-gel could easily be transferred as the basic underlying properties and potential error sources are the same.

2.4.2 *Temperature control protocol*

As mentioned in Section 2.3.5, temperature fluctuations during MR scanning have a significant influence on quantitative PGD evaluation. To minimize the impact of temperature differences, special measures were taken during and prior to the MR measurement. All containers were stored at room temperature 2 h prior to T_2 evaluation inside a light shielded water filled thermobox (Figure 17(a)). To additionally monitor the water temperature and to ensure that the influence of RF-induced energy deposition (especially for longer measurements) is kept to a minimum, the initially used thermobox was replaced by a water-flow phantom, which was developed to keep the temperature constant within $\pm\ 0.1\ °C$ (Figure 17(b)). Motion artefacts caused by the water flow were reduced by substituting a contrast agent (Gd-DTPA) to the water (T_1- and T_2- $< 50\ ms$). Both storage method aimed at achieving the temperature of the scanner-bore (approx. $20\ °C$). To directly visualize whether temperature fluctuations occur during the measurement, a set of eight calibration vessels were measured at different slice positions at the beginning and the end of each MR measurement procedure. As they often include time consuming 3D measurements (up to $3\ h$), the preferable temperature control protocol should be able to keep deviations between both calibration curves to a minimum.

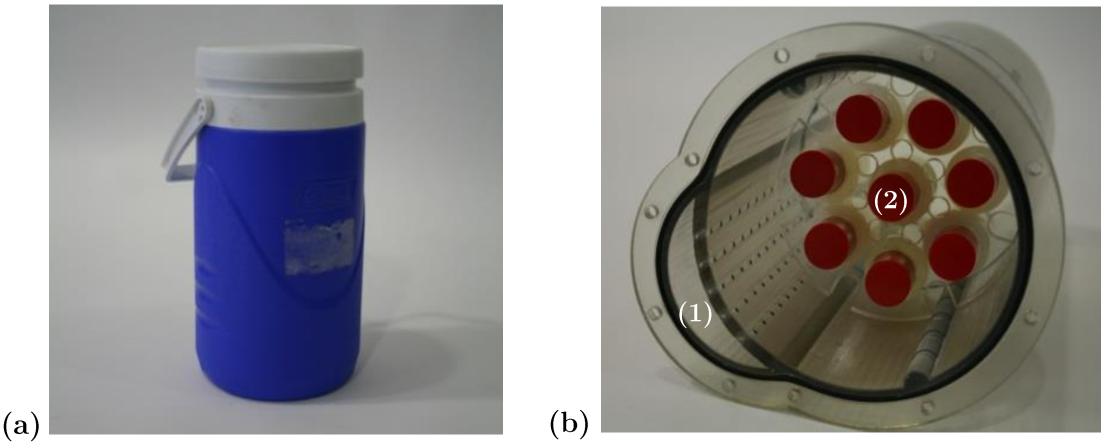

Figure 17. MR measurements of the *gel tumor* and calibration probes were performed under isothermic conditions using either a thermobox (a) or a water-flow phantom (b). In the water-flow phantom the water inlet (1) is located below the measurement volume (2) containing the *gel tumor* and calibrations probes.

2.4.3 *Measurement parameters*

Besides the influence of temperature variations during the MR acquisition, CPMG measurement parameters can cause absolute T_2 values to vary. Therefore, these parameters had to be optimized first which includes (i) number of echoes used for the evaluation procedure, (ii), TR and (iii) echo time TE. The presence of stimulated echoes are known to introduce uncertainties in the T_2 fitting procedure as they cause the SE amplitude to differ from a *pure* T_2 decay. TR was optimized as to assure that on the one hand sufficient signal is available for each new excitation and on the other hand to minimize the total measurement time. This was realized by acquiring a quantitative T_1 image for doses ranging between $0 - 7\ Gy$ by using a saturation recovery (SR) sequence as implemented by the scanner with a total of 18 contrasts ranging from $20\ ms - 3000\ ms$. Unlike T_1, the T_2 values significantly change with higher doses. Therefore, TE had to be optimized in terms of the applied irradiation schemes (small-field and uniform irradiation, Section 2.5.2) and the corresponding dose-range. It had to be assured that the image noise of the last echo number for high-resolution T_2 acquisition shows only a small contribution. For this, the SNR was calculated which amounts to:

$$\text{SNR} = \frac{\text{mean signal intensity in ROI}}{\text{standard deviation of background noise}} \tag{2.16}$$

In addition, the relative T_2 error was calculated for different radiation schemes, image resolution and T_2 values.

2.4.4 *Dose resolution*

To quantify the intrinsic precision of the PGD, the metric of dose resolution was used. It takes both, dose sensitivity and MR induced noise into account. The exact formalism is based on the work of Baldoc *et al* 2001 and is defined as the minimal dose difference at which two doses D_1 and D_2 can be distinguished (see Figure 18) with a given level of confidence p by the following equation:

$$D^p_\Delta = \sqrt{2}\cdot k_p \cdot \ \sigma_D \tag{2.17}$$

where the coverage factor k_p is given by the t-distribution and σ_D is estimated to be the standard dose uncertainty given by the derivative $\partial D/\partial R_2$. For that, Equation (2.3) was rearranged to calculate the Dose with respect to R_2.

$$\mathrm{D(R_2)} = \frac{1}{\alpha}\ln\frac{\Delta \mathrm{R_2}}{\mathrm{R_{2,sat}} - \mathrm{R_2}} \tag{2.18}$$

Combining Equation (2.17) and (2.18) the final equation for the calculation of the dose resolution becomes:

$$\mathrm{D^p_\Delta} = \sqrt{2}\cdot \mathrm{k_p} \cdot \frac{1}{\alpha(\mathrm{R_{2,sat}} - \mathrm{R_2})}\sigma_{\mathrm{R_2}} \tag{2.19}$$

where $\sigma_{R_2}$is defined as the standard uncertainty in R_2 for a given dose value. For a given confidence level of $p = 95\%$ the coverage factor is equal to $k_p = 1.96$.

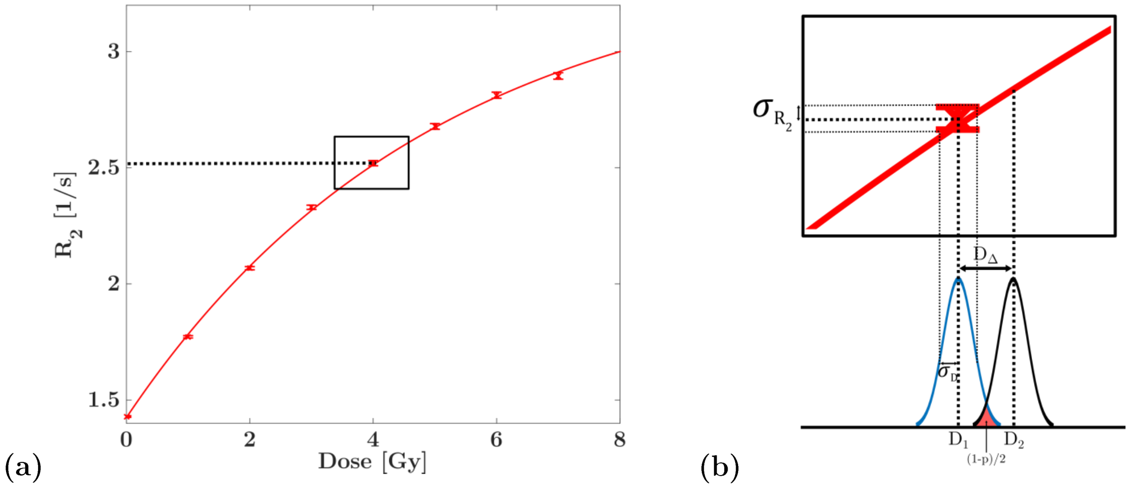

Figure 18. Schematic illustration of the basic principles of dose resolution. By means of a calibration curve (a) measurement uncertainties σ_{R_2} are converted to dose uncertainties σ_D. (b) The term of dose resolution ΔD aims at defining the minimum distance at which two doses D_1 and D_2 with an uncertainty σ_{R_2} can be separated with a level of confidence p which is directly related to the red area under the dose curves.

It should be noted that this definition of dose-resolution does not include stochastic variations in production procedure (chemical concentration, homogeneity of gel mixing, temperature during production) or dose delivery. All experiments were performed with the in-house produced PAGAT dosimetry gel which is why a systematic evaluation of the commercially available Pre BANG-kit in terms of dose-sensitivity and –resolution was not necessary.

2.4.5 *B_1 and B_0 inhomogeneities*

Besides temperature related error sources, local field inhomogeneities that are present during image acquisition can significantly influence quantitative T_2 measurements. This effect is especially pronounced in the outer region of larger phantoms (De Deene and Vandecasteele 2013). However, as our polymer gel dosimetry workflow differs from the standard procedure, this effect needs to be investigated first. Quantitative B_1 and B_0 field-inhomogeneity maps were acquired using the recently published water shift and B_1 approach (WASABI) (Schuenke *et al* 2017). It enables simultaneous flip angle (FA)-B_1 and B_0-mapping in a single acquisition. Measurements of a uniformly irradiated *gel tumor* were performed inside the water-flow phantom which was switched off during image acquisition. Prior to the scan, a manual B_0 shim was applied to reduce the influence of field inhomogeneities caused by the static magnetic field. B_0 and B_1 maps were acquired in 2D for a central slice located within the *gel tumor* and compared with the corresponding T_2 distribution.

2.4.6 *Dose rate dependence*

In polymer gel dosimetry and the application for patient-specific workflow verification, the *gel tumor* is irradiated to ensure uniform coverage. In clinical routine, this is usually realized by irradiating the target from different directions / gantry angles. As a result, a continuous irradiation of the target cannot be performed as for the step-and-shoot technology, the irradiation comes to a halt until the next gantry angle is reached. Depending on the location, motion behavior and target size, irradiation length can differ from gantry angle to gantry angle and therefore the rate at which the total dose is delivered to the target volume varies. To analyse this dose-rate dependency, two sets of *gel tumors* from the same batch were irradiated inside the cylinder phantom with a total of 520 *MU* from a gantry angle of 90°. While for *gel tumor* (i) the dose was continuously delivered, the irradiation for *gel tumor* (ii) was divided into 4 fractions of 130 *MU* each with a time delay of $\Delta t = 60\ s$.

2.5 Phantom measurements

In this study, four experimental series were performed taking the results of Section 2.4 into account. The goals of these measurements were (i) to determine the accuracy of the PGD using the implemented workflow under geometrically and dosimetrically well-defined conditions (Section 2.5.3), (ii) feasibility testing in the dynamic lung phantom (Section 2.5.4), (iii) to investigate different clinical margin and motion-compensation concepts (Section 2.5.5 - 2.5.6) and (iv) to validate a 4D dose calculation algorithm (Section 2.5.7). Experiments (i) - (iv) involved the following steps: phantom preparation, imaging, treatment planning and irradiation according to the standard patient protocols.

2.5.1 *CT imaging*

Images for treatment planning were acquired on a SOMATOM Definition Flash (Siemens AG Healthineers, Forchheim, Germany). Prior to the scan, a reference point was defined by three fiducial X-Spot markers (Beekley Medical, Bristol, USA) being attached in the intersection point of the sagittal, the two horizontal and the transversal laser lines on the surface of the phantom. The phantoms were then aligned with respect to the in-room CT laser system. CT acquisition was performed using the following imaging parameters: voltage 120 kVp, current 300 mAs and VS $= 1 \times 1 \times 1\ cm^3$.

CT scans with the cylinder phantom were performed without *gel tumor* motion whereas for the porcine lung phantom, scans were performed either with (dynamic mode) or without (static mode) *gel tumor* motion. In the dynamic mode, *gel tumor* motion was realized by applying a breathing pattern previously acquired from a patient at 12 respiration cycles per minute. In this case, both, a static and a 4D-CT scan was performed. For the 4D-CT, the breathing curve was detected with the ANZAI™ pressure sensor, previously connected to the air flow unit by means of a dedicated adapter. Time-resolved CT images were reconstructed at breathing phases corresponding to 0%, ±20%, ±40%, ±60%, ±80% and ±100% of the breathing phase.

2.5.2 *Treatment planning*

3D-CRT treatment planning was performed with the Raystation TPS (RaySearch Laboratories, Stockholm, Sweden) using a collapsed cone dose calculation algorithm and a dose grid resolution of $1 \times 1 \times 1\ mm^3$ or $2 \times\ 2 \times\ 2\ mm\ ^3$ depending on the beam shape and irradiation procedure. Treatment plans for the various experimental series will be described in the following.

2.5.3 *Accuracy of gel dosimetry*

As in polymer gel dosimetry, uncertainties in terms of gel production, storage, irradiation and MR evaluation are well-known and could significantly influence the measured dose distribution, an initial experiment was performed to benchmark the accuracy of the PGD under geometrically and dosimetrically well-defined conditions. For this, the outer ring of the cylinder phantom was filled with water while the inner part was filled either with water or LEM. Dose measurement was performed in 3D by inserting a dosimetry-gel flask in the center. For both, LEM- and water-insert two different treatment plans were generated: (i) Uniform target coverage using two opposing beams (90°, 270°) with field sizes of 10.0 × 10.0 cm^2 and a median dose of $D\ =\ 4\ Gy$ and (ii) small-field irradiation using three equally-spaced beams (0°, 120°, 240°) with a field size of $1.0\ \times\ 1.0\ cm^2$ and a maximum dose of $D_{max} = 5\ Gy$ with dose gradients of up to $5\ Gy/cm$. Here, the dose maximum is located within the central region of the *gel tumor*. Experiment (i) was motivated as to quantify the absolute precision of the gel and the implemented evaluation workflow whereas experiment (ii) was performed as to quantify the overall accuracy in terms of positioning uncertainties, dose gradient, shape and absolute dose. In both cases, the gel measurement was supplemented by a 1D dose measurement (either by a standard PinPoint™ ionization chamber (31014, PTW, Freiburg, Germany) for (i) or a diode (sensitive volume 0.03 mm, Dosimetry Diode E, Type 60017, PTW, Freiburg, Germany) for (ii)) positioned at the center of a new *gel tumor* which acts only as an absorber and is not used for dose measurement. Both, the calibration flasks and the *gel tumor,* were stored inside the water-flow phantom two hours prior to and during the quantitative T_2 evaluation. A total of 15 slices for the uniform irradiation and 28 slices for the small-field irradiation were measured. All measurements were performed with a single batch of dosimetry gel allowing both, qualitative and quantitative comparison between the measured and planned dose distributions. As a first experiment, where quantitative data was analyzed, the entire workflow of polymer gel dosimetry had to be evaluated. This also includes the evaluation of the proposed data filtering process in terms of (i) dose gradient conservation and (ii) noise reduction for the uniform irradiation. Both properties were subsequently analyzed for a small-field irradiation and uniform *gel tumor* coverage using the water-insert.

2.5.4 *Feasibility of 3D gel dosimetry inside the dynamic lung phantom*

As the combination of polymer gel dosimetry and the anthropomorphic lung phantom has not yet been performed, initial experiments focus on the feasibility testing of the entire experimental setup. As a first step a suitable position of the *gel tumor* within the porcine lung phantom had to be identified. As the *gel tumor* is sewed to the lung by means of a special holder the following requirements in terms of positioning should be met: (i) direct sewing onto the lung should be avoided because of air leakage, (ii) sufficient and (iii) reproducible *gel tumor* motion and (iv) the influence of the *gel tumor* on the motion pattern of the porcine lung should be kept to a minimum. As a next step, the PGD was irradiated using different irradiation settings. For this, three equally-spaced beams (0°, 120°, 240°) were planned with a maximum dose of 5 Gy located completely in the center of the *gel tumor* and a field size of $1.0 \times 1.0\ cm^2$. As a result, steep dose gradients of up to 5 Gy/cm could be realized. Three independent irradiation experiments, each with a new batch of dosimetry gel, were performed for the following conditions: (a) static *gel tumor*, (b) moving *gel tumor* without applying any motion-compensation techniques, and (c) a moving *gel tumor* including a gated treatment with a gating window (GW) of ±20% relative to the end-inspirative breathing phase.

2.5.5 *End-to-end tests for standard motion-compensated treatments*

As the overarching objective of this work is to use the combination of PGD and the porcine lung phantom for clinical workflow verification, the setting was also tested in terms of clinical margin and motion-compensation concepts. This includes a uniform irradiation of the target volume. Therefore, the entire sensitive volume of the *gel tumor* was considered as the CTV, which should be irradiated uniformly without causing hot- or cold-spots. Treatment planning was performed using a set of nine equally spaced beams (0°, 40°, 80°, 120°, 160°, 200°, 240°, 280°, 320°), a single segment per beam and a dose-gradient of 3 $Gy\ /\ cm$. Again, three independent irradiation experiments, each with a new batch of dosimetry gel, were performed for the following conditions: (a) static *gel tumor*, (b) moving *gel tumor* including an adequately defined ITV to compensate for motion and (c) moving *gel tumor* compensated by a gated treatment (GW = ±40%) and an accordingly reduced ITV. In the case of the moving *gel tumor,* the final ITV was obtained using both, the previously defined CTV and the individual 4D-CT breathing phases in combination with a semi-automatic deformable registration algorithm as implemented by the TPS. The final PTV was generated by additionally adding a 2 mm safety margin to compensate for positioning or machine related errors.

2.5.6 *End-to end test for real-time markerless fluoroscopic tumor detection for treatments with beam gating*

Although the standard motion-compensation techniques are widely used in clinical practice, the problem of inter- and intra-fractional tumor motion is not completely solved, yet. As the treatment plan is usually based on a single 4D-CT dataset, a uniform tumor irradiation can only be guaranteed if the motion trajectory does not significantly change. This is especially not guaranteed, if beam gating is applied as the time-dependent tumor position is obtained by correlating an external surrogate signal with the different phases of the 4D-CT during treatment planning. If this correlation is not maintained during treatment, a wrong tumor position will be assigned to the surrogate signal and as the surrogate signal steers the irradiation, significant deviations in the delivered relative to the planned dose distribution may be obtained. It is therefore very important to include an intra-fractional real-time-validation of the tumor position during irradiation to assure that the correlation of the surrogate signal with the tumor position is still correct.

In this work, such a real-time validation method was realized by a combination of fluoroscopic real-time imaging and an in-house developed online lung tumor detection algorithm (Teske *et al* 2015). An in-house developed hardware communication system (Fast *et al* 2012) was used to acquire fluoroscopic images in anti-parallel direction of the beam during the irradiation. Major advantage of this imaging direction as compared to orthogonally mounted systems is that tumor motion perpendicular to the beam can be visualized.

The applied tumor detection algorithm is based on a multiple template matching algorithm (MTMA), which compares a tumor template acquired from a training dataset with the fluoroscopic image. The final tumor location is then determined as the template position with the maximum normalized-cross-correlation-coefficient (NCC) within the fluoroscopic image (Mercea *et al* 2015).

As fluoroscopic images consist of time resolved 2D images (2D+t) the MTMA had to be trained on a similar dataset. This training data set was obtained by generating so-called digitally reconstructed radiographs (DRR) for all motion phases of the 4D-CT dataset and for all beam angles. The DRRs were calculated by means of a ray-tracing algorithm as published by Siddon 1985, using the open-source program *Plastimatch* (Sharp *et al* 2010). Thus the tumor trajectory has to be validated for all breathing phases at each beam angle. The calculated template positions within the DRRs were then used to define a tumor position acceptance region (TPAR) for all breathing phases and each beam angle. For a more detailed workflow description and a systematic analysis of the detection algorithm, the interested reader is referred to the work of Witte 2016.

To validate the combination of a gated treatment with the real-time validation of the tumor position, an end-to-end test was carried out. In this experiment a gating window of ±40% was used and the surrogate signal was obtained from the Anzai system. However, in contrast to section 2.5.5, the Anzai signal was used to trigger the imaging system for the real-time fluoroscopic validation of the tumor position rather than to gate the beam. Only if the *gel tumor* position as calculated by the MTMA is located within the TPAR, the beam is switched on. A schematic overview of the developed workflow is displayed in Figure 19.

In this experiment, the entire sensitive volume of the *gel tumor* was considered as the CTV and the goal was to deliver a uniform dose of 4 Gy to this volume. According to previous experiments (Witte 2016), a set of 10 gantry angles (0 °, 20 °, 80°, 90 °, 120 °, 160 °,180 °, 240 °, 270 °, 300 °) with a single segment per beam was planned. The final PTV was then generated by additionally adding a 2 mm safety margin to compensate for positioning or machine related errors.

Prior to the experiment, potential error sources caused by the imaging system were evaluated. As the imaging detector is placed in front of the MLCs, the primary beam may cause severe imaging artefacts and dedicated correction protocol might be necessary. Furthermore, as the primary beam penetrates the detector, it is additionally attenuated. Dedicated measurements were performed with a Farmer IC (30001, PTW, Freiburg, Germany) under reference conditions with and without the imaging detector in front of the beam line. This measurement was repeated for various field sizes, ranging from $3 \times 3\ cm^2$ to $20 \times 20\ cm^2$.

2.5.7 *Validation of the 4D dose calculation for a moving target*

Beam gating aims at irradiating the tumor only, if it is located at a specific position. However, residual motion of both, tumor and OARs might still be present that can cause the calculated dose distribution to deviate from measurements. Therefore, a dedicated workflow needs to be implemented that allows detecting and correcting for such motion. A possible solution is to perform a retrospective 4D dose calculation using externally acquired tumor-trajectory data. However, such a dose calculation algorithm needs to be validated first before it can be integrated into the clinic.

In a previous work, a motion robot has been used to reproduce the treatment delivery of clinically applied prostate treatment plans using the tumor-trajectories acquired with the Calypso^{TM}-system during the treatment of the patient. The delivered dose was then measured in 1D or 2D using an ionization chamber or films. As a next step, the experimental data was then compared with an in-house developed 4D dose calculation using exactly the same motion pattern (Schmitt *et al* 2012).

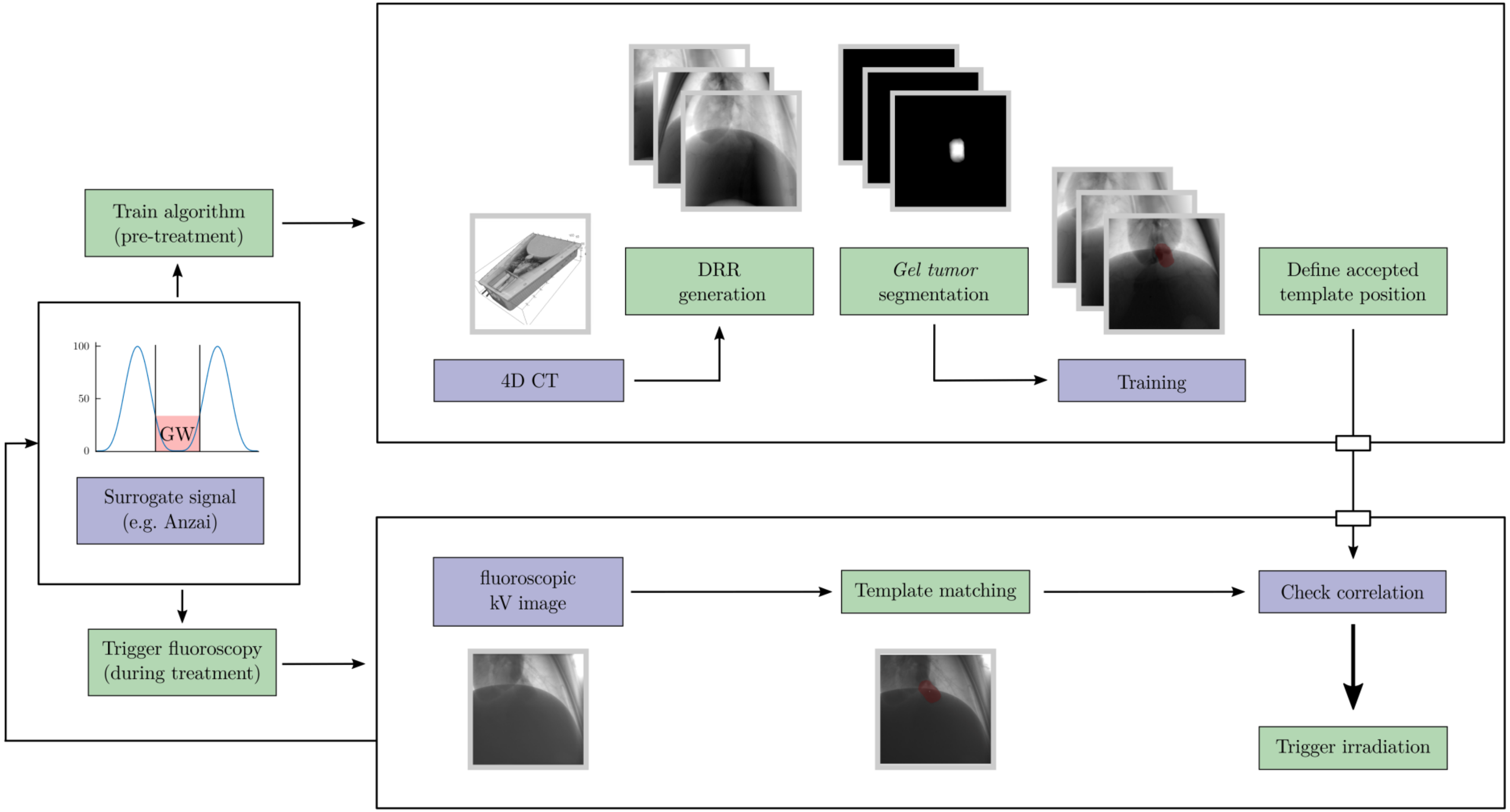

Figure 19. Schematic overview of the implemented fluoroscopic-guided gating workflow. The general principle can be separated in (i) a training (top) and (ii) a treatment (bottom) phase. Based on the surrogate signal (left), the pre-defined GW is either to define respiratory phases that are located within the GW or to trigger the kV imaging system.

In the present study, we used the PGD to measure the 3D accumulated dose distribution in the gel, while the *gel tumor* is moving. The information about the tumor trajectory, required for the 4D dose distribution, was obtained from two sources: (i) from the transmitted position of three Calypso^{TM} beacons, which were fixed close to the irradiated target volume by means of a special holder (Figure 20) and (ii) from the log-file information of the motion robot (including both, speed and exact position).

The first experiment was performed with the cylindrical phantom using only the water insert. A 4D dose distribution has been calculated retrospectively using in-house developed software by shifting the target point within the planning CT based on the motion information (from the Calypso^{TM}-system or the motion robot, respectively) and based on the beam status recorded with the Calypso^{TM}-system. For each target point position, a new sub-beam was assigned together with a weighting factor corresponding to the duration of the irradiation at the respective target point position (Figure 21). In total, 1227 sub-beams were applied for the 4D dose calculation. As the 4D dose calculation uses the pencil beam algorithm of the in-house developed VIRTUOS TPS (Schlegel *et al* 1992), which has some limitations, the dose distribution for the static case was additionally recalculated with the Raystation TPS using the same treatment parameters.#

Figure 20. The *gel tumor* (1) is attached to a dedicated adapter (2), which also includes three Calypso^{TM} *beacons* (3). For absolute dose measurement, a PinPoint^{TM} IC can be inserted (4).

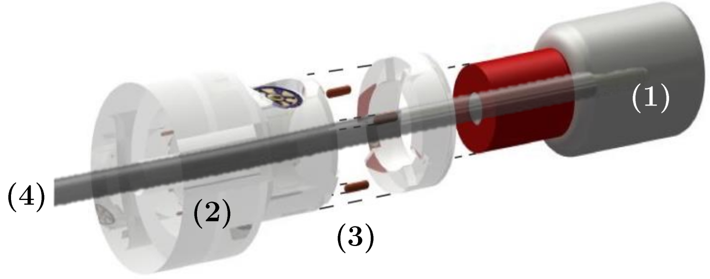

The *gel tumor* plus a 1 mm margin was considered as PTV and was covered uniformly with the median target dose of $D = 4\ Gy$. The treatment plan included 5 beams (0°, 40°, 80°, 240°, 280°) using only one beam segment per gantry angle. Lateral dose fall-off included dose gradients of $2\ Gy/cm$. That only five different gantry angles could be realized results from the experimental setting as (i) the patient table had to be moved to a peripheral position (90° table rotation) to allow the motion robot to be placed in front of the LINAC and (ii) we tried to avoid to irradiate through the motion robot table as this could influence the accuracy of our dose algorithm (280°). In addition, the Calypso^{TM}-system had severe problems to localize the electromagnetic array used for the recording of the beacons for an angle of 320° as the combination of gantry angle and motion robot were blocking the view of the infra-red cameras that are used to locate the array (see Figure 22).

In total, three experiments were performed using separate *gel tumors* from the same batch. The experiments were performed under the following conditions: (i) no phantom motion with the *gel tumor* center located at the machine isocenter to identify any gel related errors, (ii) no phantom motion with a positioning shift of 2.5 *cm* towards the container bottom to characterize the dose gradient within the PGD and (iii) including tumor motion. During irradiation, the phantom was moved periodically perpendicular to the incident beam in axial direction with 2.5 *cm* peak-to-peak amplitude and a period of 7.5 *s*. A $\cos^4$ motion trajectory was applied as it has been demonstrated to provide a good fit to the population data for respiratory motion (George *et al* 2005).

As additional absolute dose measurement, the entire irradiation procedure was repeated with a PinPoint™ Ionization Chamber (31014, PTW, Freiburg, Germany) positioned at the center of a new *gel tumor* which acts only as an absorber dose and was not evaluated. All measurements were performed with a single batch of dosimetry gel allowing for quantitative comparison between dose distributions.

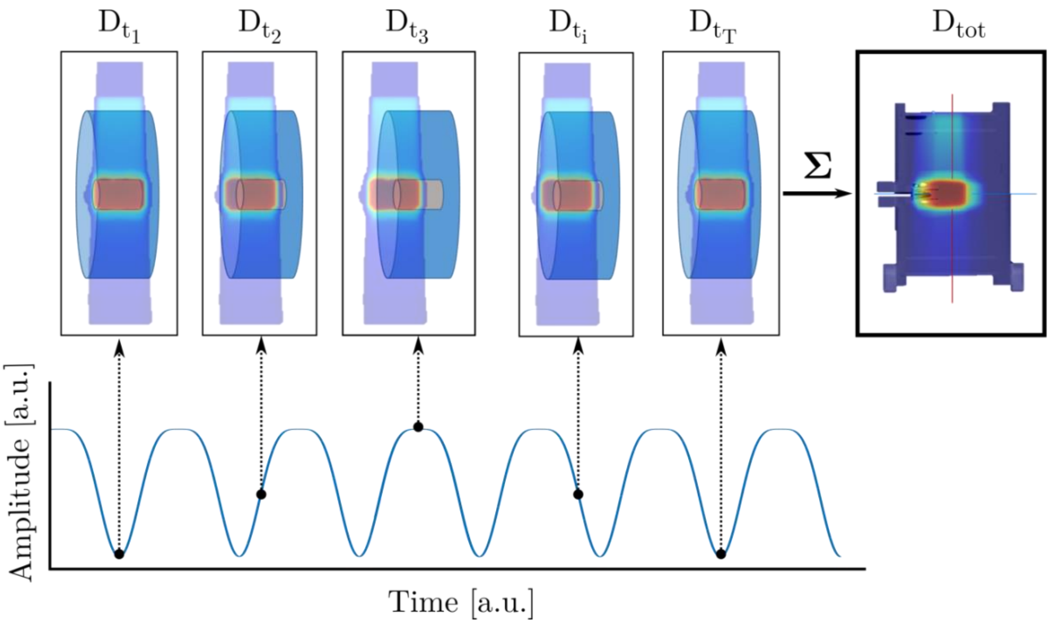

Figure 21. Basic principle of the applied 4D dose accumulation algorithm. Each motion phase t_i is correlated to the corresponding beam parameters (gantry angle and MLC settings) and individually weighted with respect to the average position to acquire the irradiated MU. The dose distributions at all time steps t_i are then summarized to acquire the total integrated dose $D_{tot} = \sum_i^T D_{t_i}$.

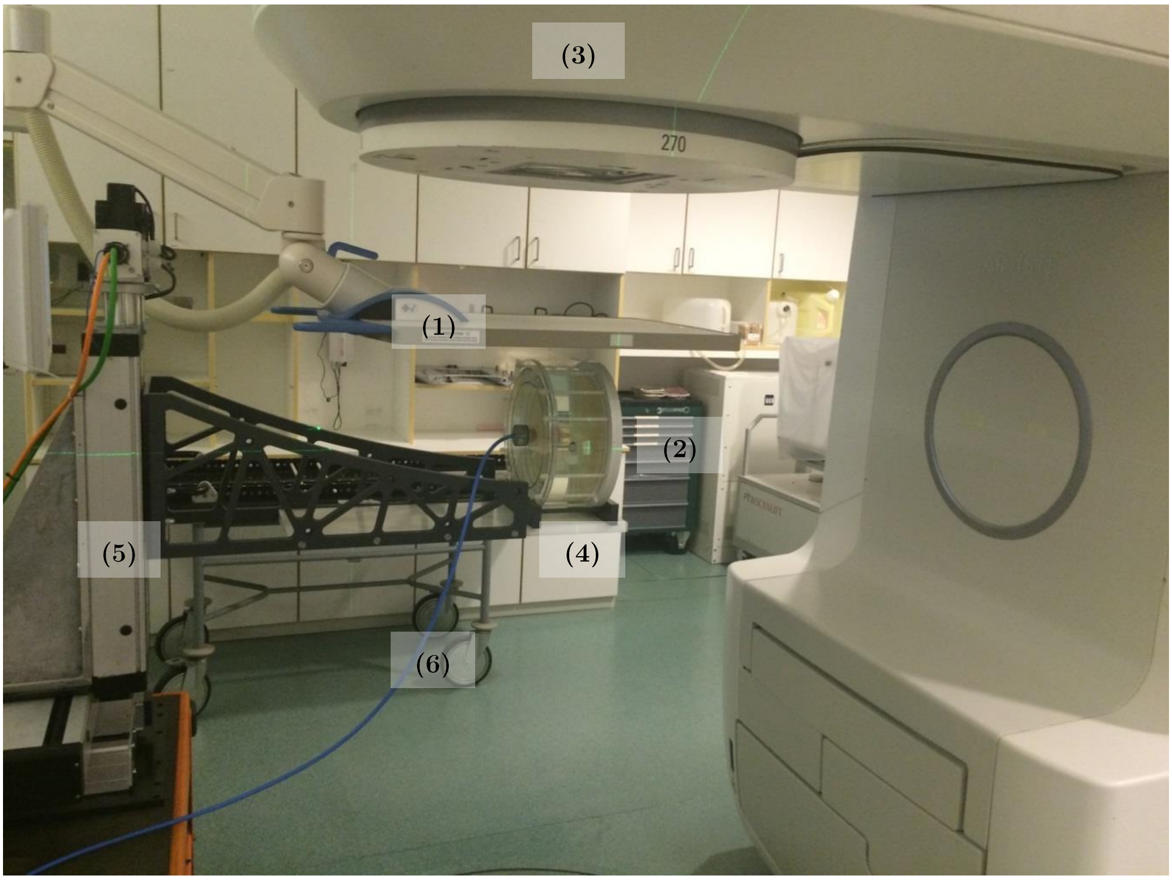

Figure 22. Experimental setup for the validation of the 4D dose calculation using independent motion monitoring by the Calypso^{TM} tracking system (1) and 3D polymer gel dosimetry (2). Irradiation was performed with a conventional LINAC (3). The cylindrical phantom (4) is placed on top of a three axis motion robot (5), which can describe arbitrary motion trajectories. Besides the PGD, a PinPoint™ chamber can be placed at the center of the phantom (6).

3 Results

Parts of this section are already published (Mann *et al* 2017a, 2017b) and reproduced with permission.

3.1 Polymer gel characterization

The goal of the following section was to implement a suitable workflow that allows performing various PGD measurements in a large variety of different environments. This includes the evaluation of suitable gel container materials (Section 3.1.1), the definition of a dedicated temperature control protocol (Section 3.1.2), optimization of MR measurement parameters (Section 3.1.3) as well as the evaluation of dose resolution (Section 3.1.4). In addition, the influence of B_1 and B_0 inhomogeneities as well as the dose rate on quantitative polymer gel dosimetry were evaluated in Section 3.1.5 and 3.1.6.

3.1.1 *Gel container materials*

Since the application of the PGD as described in this work strongly differs from the standard workflow in gel dosimetry, where usually large containers filled with dosimetry gel are irradiated (Vergote 2005 and Vandecasteele and Deene 2013), different storage materials were tested to find the most suitable container for irradiation in combination with the porcine lung phantom. The choice of materials was mainly driven by the requirements as defined in Section 2.4.1, namely (i) excellent oxygen barrier, (ii) limited interactions with the PGD, (iii) water equivalent image contrast for CT images (iv) typical tumor size and shape, and (v) the container should only show a minor influence on motion properties of the lung. At the beginning of the project, it was not clear how to combine both, the PGD and the porcine lung phantom. It was therefore essential to find a possibility to insert the *gel tumor* flask into the phantom and to assure that its location and motion pattern can be well-reproduced during the entire experiment.

Initial work was focusing on the application of a latex-balloon attached on top of a urinary catheter by means of two O-rings to keep the balloon in place. This combination was chosen as the urinary catheter (i) allows guiding the balloon through the pulmonary artery and (ii) acts as an extension that allows inserting the liquid PGD from outside the lung into the latex-balloon. However, a substantial investigation showed that the latex-balloon or other flexible materials (different latex-based materials and silicones) are not suitable for the application of polymer gel dosimetry (Mann *et al* 2015). The oxygen barrier has been shown to be rather weak and additional interactions of the wall material with the PGD and a surrounding aqueous environment, such as for a fresh porcine lung, did also occur. As a result, dose measurements with a homogeneous dose response in the whole volume were not possible with these materials. A more detailed description on the investigation of these materials in combination with the PGD are summarized in the thesis of Witte 2010. In the course of these previous tests, the idea to directly insert the *gel tumor* into the porcine lung via a catheter turned out to be impractical and was therefore not further investigated.

A promising and practical approach was to sew the *gel tumor* (Section 2.2.3) to the mediastinum of the lung by means of a dedicated holder. The mediastinum turned out to be tear-resistant and highly flexible, which makes the *gel tumor* sewing onto the lung very easy. In addition, the size of the mediastinum allows placing the *gel tumor* at various positions, which allows varying the motion amplitude (Section 3.3). As a result, the *gel tumor* material was not only limited to flexible materials and would allow the usage of rigid materials such as borosilicate glass or BAREX^{TM} material (BAREX^{TM} distributed by VELOX GmbH, Hamburg, Germany). Initial experiments with borosilicate glass showed no measurable influence on dose response due to (i) penetrating oxygen or (ii) the storage environment (water or air). However, the large CT numbers of the glass ($1176.4 \pm 139.9\ HU$, see Figure 23(a)) as compared to the PGD ($22.3 \pm 3.8\ HU$) does significantly influence the anthropomorphic image contrast. Therefore, glass turned out to be not suitable for our application.

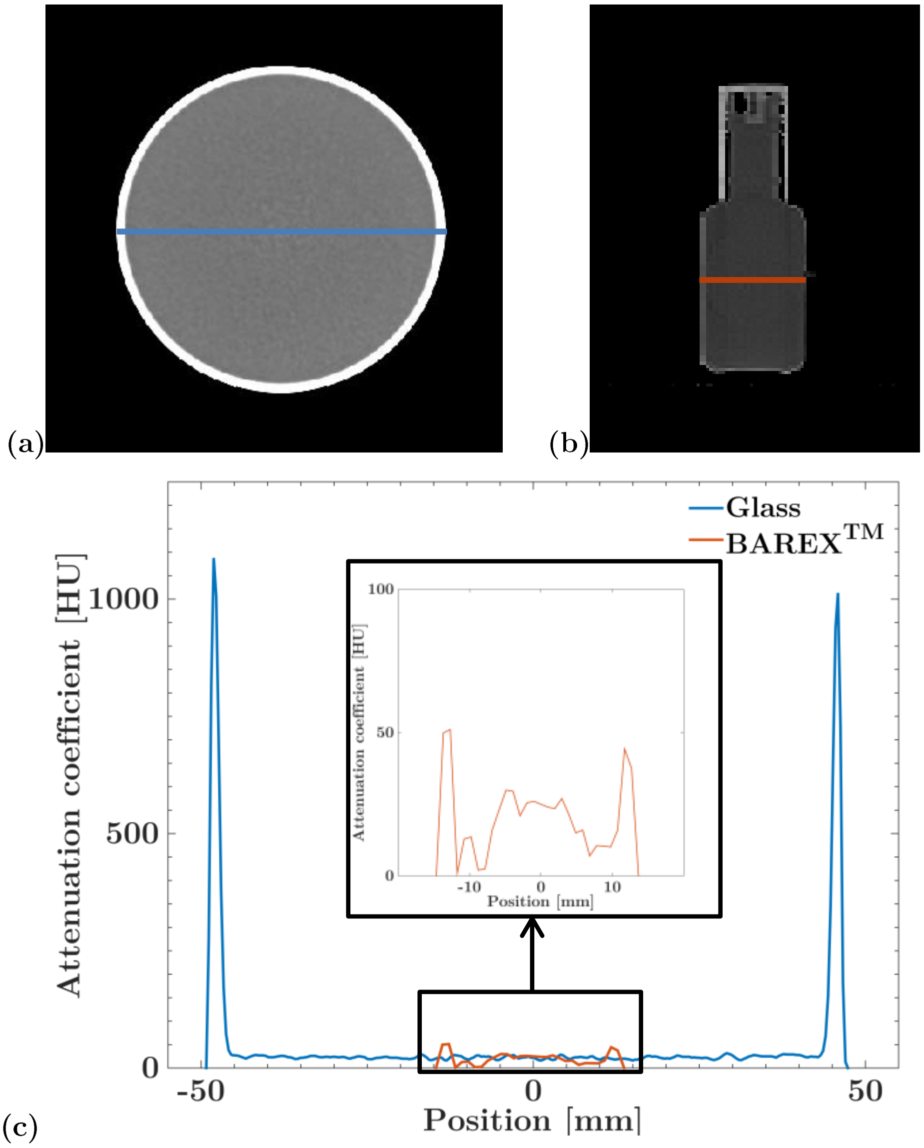

Figure 23. Transversal slice of a CT images for two different *gel tumor* storage containers, namely (a) glass and (b) BAREX^{TM}. Corresponding attenuation profiles are displayed in (c) in blue for glass and red for BAREX^{TM}, respectively.

The BAREX™ material on the other hand turned out to be a very promising material that can be used in combination with the porcine lung phantom. It consists of a thermoformable acrylonitrile-methyl acrylate copolymer with a negligible oxygen permeability and interaction rate with other chemicals, a high chemical stability (Vergote 2005) and it also has a water equivalent image contrast for CT images (48.4 ± 24.3 HU, see Figure 23(b)). In addition, the BAREX™ flasks provides a sufficiently large sensitive PGD volume ($V = 25$ ml) and in combination with its cylindrical shape (length $l = 45$ mm, diameter $d = 28$ mm, wall thickness $t =$ 0.6 mm), it can be used to simulate a non-small cell lung cancer (NSCLC) of stage T2a (Giaccone 2012). Furthermore, the BAREX™ container can also be used for the PGD calibration purposes and by this, volume-related uncertainties that are described in literature when calibration and *gel tumor* flasks differ in size are minimized (De Deene *et al* 2007).

3.1.2 *Temperature control protocol*

As temperature fluctuations during quantitative T_2 measurement are known to significantly alter calculated values, two different settings were evaluated to keep the temperature constant within the measurement volume. Figure 24 shows the variation of the calibration curves caused by temperature changes for two measurements separated by 3 h when using (i) the thermobox or (ii) the water flow phantom, respectively. In case of (i), corresponding calibration curves showed a shift to higher doses for a specific R_2 (Figure 24(a)). As a result, this would lead to large relative dose differences of up to 25% (Figure 24(c), blue curve) for lower doses and up to 6.5%. for doses larger than 6 Gy. A significant stabilization of the calibration curve over time was realized by using the water-flow phantom. No significant shift to higher doses was visible (Figure 24(b)) and maximum dose differences of only 4.1% for low- and 2.0% for high-dose regions were found (Figure 24(c), red curve). Furthermore, the dose differences became stable already at doses larger than 2 Gy.

Variations on the calibration curve acquired in (ii) for three different slice positions (top, middle bottom) are visualized in Figure 26.(a) and (b). Figure 26.(c) additionally displays the relative dose difference between two slices (top and middle, bottom and middle). It can be seen that only minor difference of 1.7% and 1.5% for the top and bottom slice, respectively, were calculated.

3.1.3 *Measurement parameters during image acquisition*

Besides the presence of temperature related dose uncertainties, the MR acquisition sequence parameters can also have a significant influence on quantitative polymer gel dosimetry evaluation. For this, various parameters such as number of acquired echoes, TR, TE and image resolution were optimized in terms of dose uncertainty, dose resolution and acquisition time.

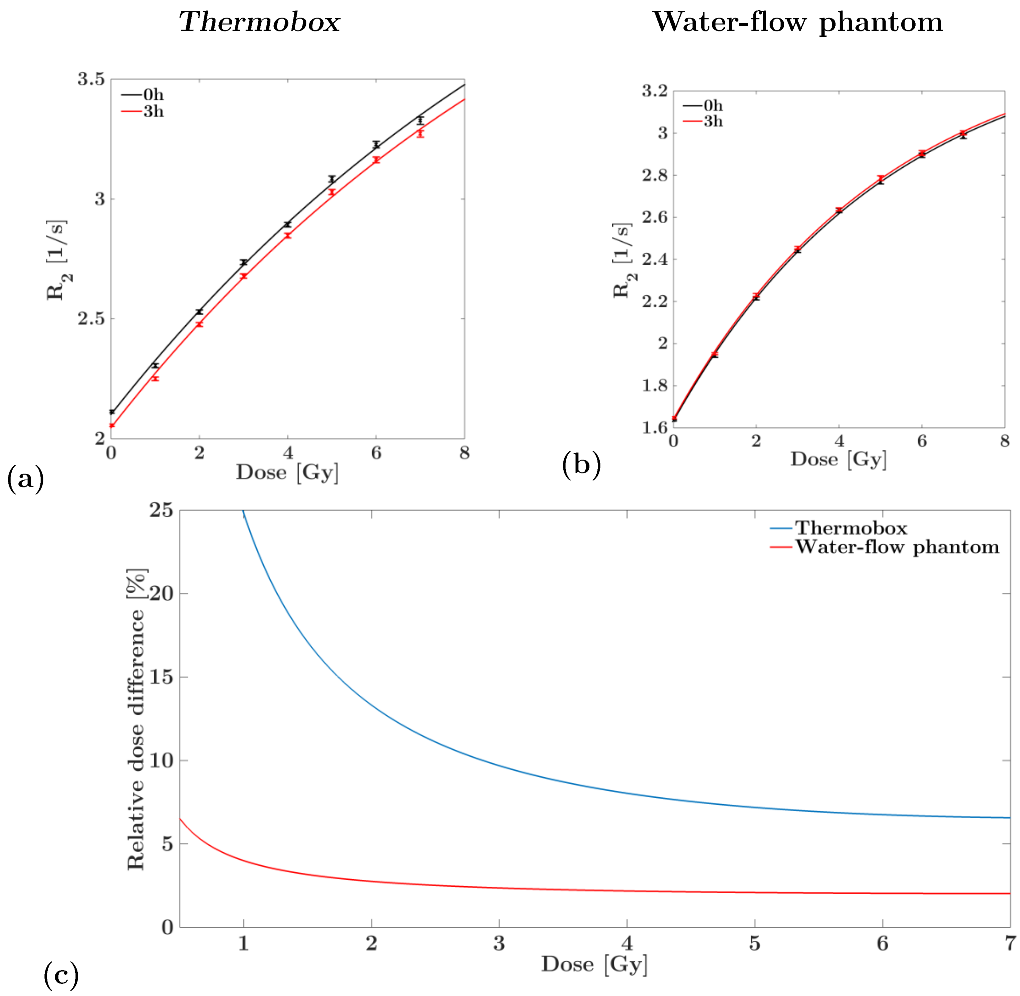

Figure 24. Calibration curves acquired for phantom measurements using (a) a thermobox or (b) a water-flow phantom at the beginning (black) and after 3 h (red). The relative dose difference (c) shows a decreasing temperature-dependence with increasing doses. This effect is especially visible for data acquired inside the thermobox where differences amount up to 25% in low-dose regions. It should be noted that measurements in the thermobox and water-flow phantom were performed with a different batch of PGD, therefore, a quantitative comparison of fit parameters of the calibration is not meaningful for investigating the temperature dependence.

Stimulated echoes

T_2 values acquired with a CPMG sequence are known to suffer from stimulated echoes that can cause variations. A comparison between two calculations, where all echoes are included (see Figure 26(a)) or the first three echoes were excluded (see Figure 26(b)) from the fitting process revealed only minor differences in absolute T_2 values in the order of 3%. However, the corresponding T_2 uncertainty for each calibration flask and therefore the uncertainty in the resulting calibration curve have a strong influence on the overall dose resolution (see Figure 26(c) and (d)). When all echoes were included into the fitting procedure, the relative mean dose resolution amounted to $D_{\Delta}^{95}/D = 0.23$. However, by removing echo one to three, the resolution could be significantly increased to $D_{\Delta}^{95}/D = 0.05$.

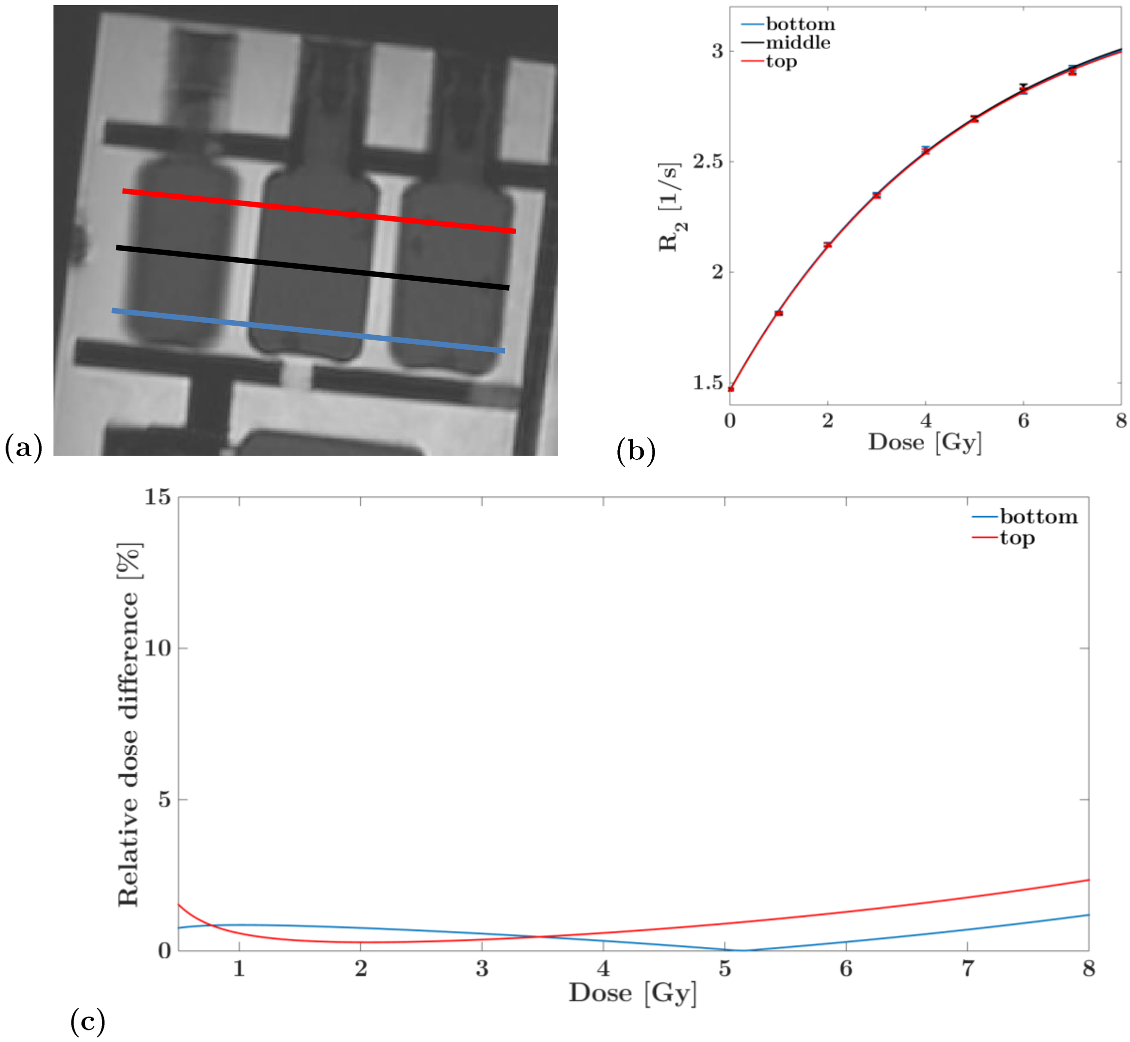

Figure 25. (a) Three different parallel slice positions used for the measurement of the calibration curve inside the water-flow phantom: bottom (blue), center (black) and top (red). (b) Comparison of the resulting calibration curves. (c) Relative dose difference for the three evaluation positions as function of dose. Differences relative to the central slice amounts to less than 2%.

TR optimization

An optimal TR was chosen as to provide adequate primary magnetization while keeping the total acquisition time to a minimum. A previously acquired quantitative T_1 map for a set of eight calibration flasks did not show significant variations in T_1 with varying dose. The mean measured T_1 value amounted to $T_1 = 2.01 \pm 0.04\ s$. As the correct choice of TR is a trade-off between measurement time and signal intensity, two different TR values were selected ($3\ s$ and $6\ s$) to acquire a calibration curve with $TE =\ 40\ ms$ (Figure 27). A comparison between both calibration curves showed only minor dose differences in the order of 2% for doses between $1\ Gy$ and $6\ Gy$. An $SNR = 17.4$ (high-dose ROI, $D = 7\ Gy$) and $SNR = 93.3$ (low-dose ROI, $D = 0\ Gy$) were calculated for $TR = 3\ s$ while data acquisition for $TR = 6\ s$ could increase SNR by approx. 34% in both cases. However, as the MR acquisition was optimized to acquire single slices and therefore an increase in TR by a factor of 2 would double to total measurement time, TR was set to $3\ s$ as it still provides sufficient SNR over a large range of dose values.

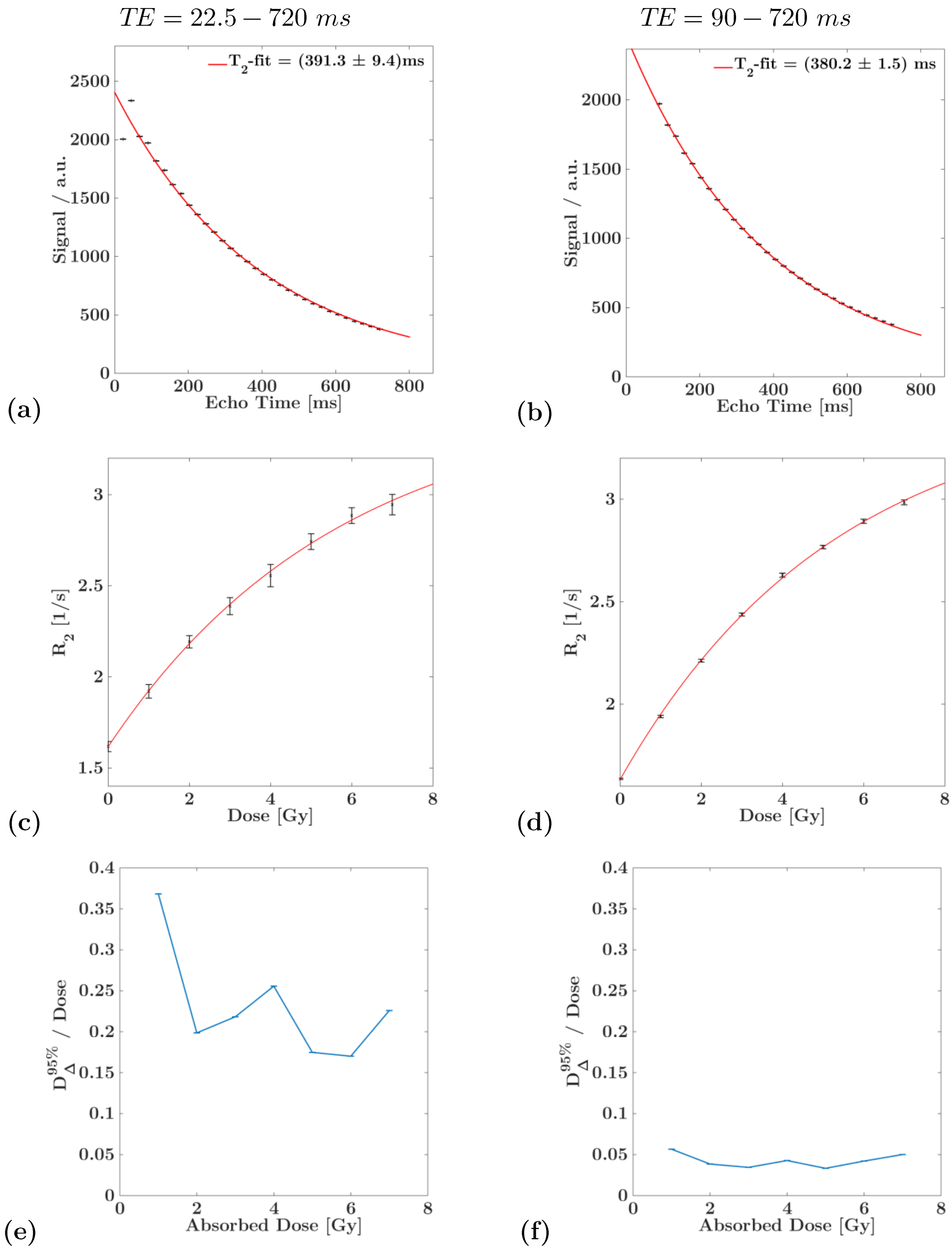

Figure 26. One set of PGD calibration flasks were measured inside the water-flow phantom including either 32 echoes ((a), (c) and (e)) or 29 echoes ((b), (d) and (f)) for the fitting procedure. A representative T_2 decay for a high-dose region (4 Gy) is shown in (a) and (b). Calibration curves are displayed in (c) and (d) with its corresponding dose resolution ((e) and (f)).

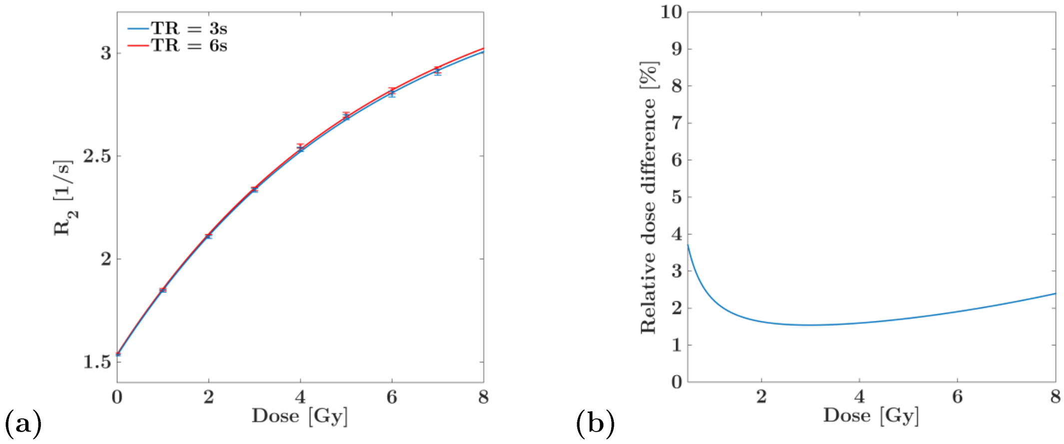

Figure 27. (a) One set of PGD calibration flasks was measured for $TR = 3\ s$ (blue) and $TR = 6\ s$ (red). The relative dose difference for both calibration curves for a given dose value was also calculated (b).

TE optimization

The correct choice of an optimal echo spacing allows minimizing uncertainties in the fitting procedure. This is especially important if no ROI-based averaging is performed as averaging would significantly lower the influence of noise. Depending on the application and experimental setting, two different image resolutions were chosen, $VS = 1 \times 1 \times 1\ cm^3$ for a small-field and $VS = 2 \times 2 \times 2\ cm^3$ for a uniform irradiation. Since the voxel size significantly changes the SNR, the echo spacing was correspondingly adjusted to ensure that there is still sufficient signal available for higher echo numbers. On the other hand, it had to be assured that the signal decrease was sufficiently measured along a wide range of the mono-exponential decay. The echo spacing was also adjusted as to cover a large range of different T_2 values (usually between $300\ ms$ and $650\ ms$). An echo spacing of $40.0\ ms$ was chosen $VS = 2 \times 2 \times 2\ cm^3$. A pixel-wise fitting showed only minor T_2 uncertainties in the order of 0.5% with a SNR for higher echo numbers ($N_{echo} = 32$) of $SNR = 42.1$ (Figure 28(a)). Using the same parameters for a voxel size of $1 \times 1 \times 1\ cm^3$ resulted in ΔT_2 for both, high-dose and low-dose regions of 3% and 1.9%. In addition, the SNR of the last echo was significantly reduced to values of $SNR_{high} = 4.4$ and $SNR_{low} = 10.2$ (Figure 28(b)), which is why the internal echo spacing was decreased to $TE = 22.5\ ms$ (Figure 28(c)). As a result, both, ΔT_2 and SNR could be improved to 1.0% and 1.6% for ΔT_2 and an SNR of 17.4 and 33.4 for the high-dose and low-dose region, respectively.

<table>
<tr><th>Irradiation</th><th>Homogeneous</th><th colspan="4">Small-field</th></tr>
<tr><td>Voxel size</td><td>$2\ x\ 2\ x\ 2\ mm^3$</td><td colspan="4">$1\ x\ 1\ x\ 1\ mm^3$</td></tr>
<tr><td><i>TE</i></td><td>$40\ ms$</td><td colspan="2">$40\ ms$</td><td colspan="2">$22.5\ ms$</td></tr>
<tr><td></td><td>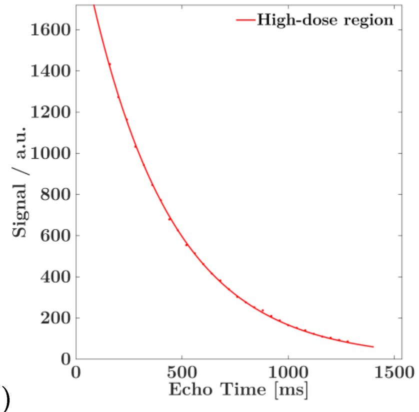
(a)</td><td colspan="2">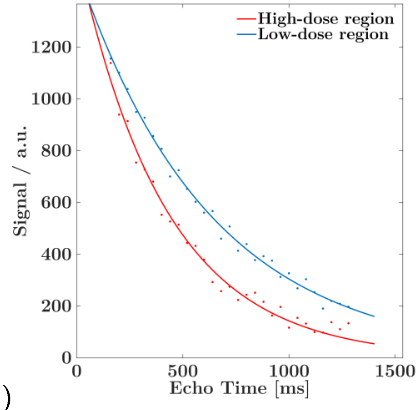
(b)</td><td colspan="2">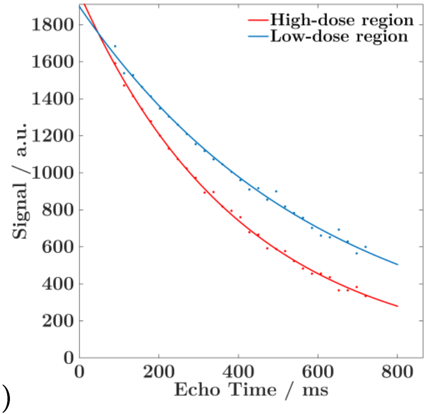
(c)</td></tr>
<tr><td>Region</td><td>High-dose (4 Gy)</td><td>High-dose (5 Gy)</td><td>Low-dose (0 Gy)</td><td>High-dose (5 Gy)</td><td>Low-dose (0 Gy)</td></tr>
<tr><td>T_2</td><td>391.8 ± 1.8 ms</td><td>417.3 ± 12.6 ms</td><td>625.6 ± 12.0 ms</td><td>$409.5 \pm 4.2\ ms$</td><td>603.9 ± 9.7 ms</td></tr>
<tr><td>$\Delta T_{2,rel}$</td><td>0.5 %</td><td>3.0 %</td><td>1.9 %</td><td>1.0 %</td><td>1.6 %</td></tr>
<tr><td>SNR</td><td>42.1</td><td>4.4</td><td>10.2</td><td>17.4</td><td>33.4</td></tr>
</table>

Figure 28. Single-voxel T_2 measurement using a multi-SE CPMG acquisition scheme for two different types of irradiation (uniform (a) and small-field (b) and (c)) for $TE = 40\ ms$ ((a) and (b)) and $TE = 22.5\ ms$ (c). In case of a small-field irradiation, both, low-dose and high-dose regions were analyzed corresponding to high- and low T_2 values, respectively. The signal intensity was fitted against a mono-exponential function. The first three echoes were not included into the fitting procedure. Besides the relative error of quantitative T_2 calculation, the SNR was also measured. As expected, a reduced voxel size results in lower SNR and larger ΔT_2 values. By adjusting the echo spacing TE, both, SNR and ΔT_2 could be significantly improved.

3.1.4 *Dose resolution and calibration*

The dose resolution is defined as the minimal dose difference between two measured doses that can be resolved at a confidence level of 95%. Since the dose conversion is performed by means of a calibration curve, the uncertainty in R_2 calculation has a direct influence on dose resolution. Previous measurements also showed a dependence of the calibration curve on the measurement parameters TE and slice thickness. Therefore, dose resolution was determined for two different parameter settings: (i) $TE = 22.5\ ms$ with $VS = 1 \times 1 \times 1\ mm^2$ and (ii) $TE = 40\ ms$ with $VS = 2 \times 2 \times 2\ mm^2$ (Figure 29(a)) and a total of 18 calibration curves each were included in the evaluation procedure. The relative dose resolution for (i) was calculated to be $4.6 \pm 1.1\%$ while (ii) amounted to $4.9 \pm 0.4\%$. That means that for a measured dose of e.g. 4 Gy, the next dose value which can be resolved is 4.184 Gy and 4.196 Gy, for the cases (i) and (ii), respectively. In addition, a mean calibration curve for both cases was calculated as well (Figure 29(b)). A comparison between both mean calibration curves indicated that choosing a short TE and a small voxel-size resulted in a broader coverage of R_2values ($\Delta R_2 = 2.6\ s^{-1}$ as compared to $TE = 40\ ms$ and $\Delta R_2 = 1.8\ s^{-1}$) while relative variations in R_2 values are larger and amount to 9.5% (i) as compared to 5.5% for $TE = 40\ ms$.

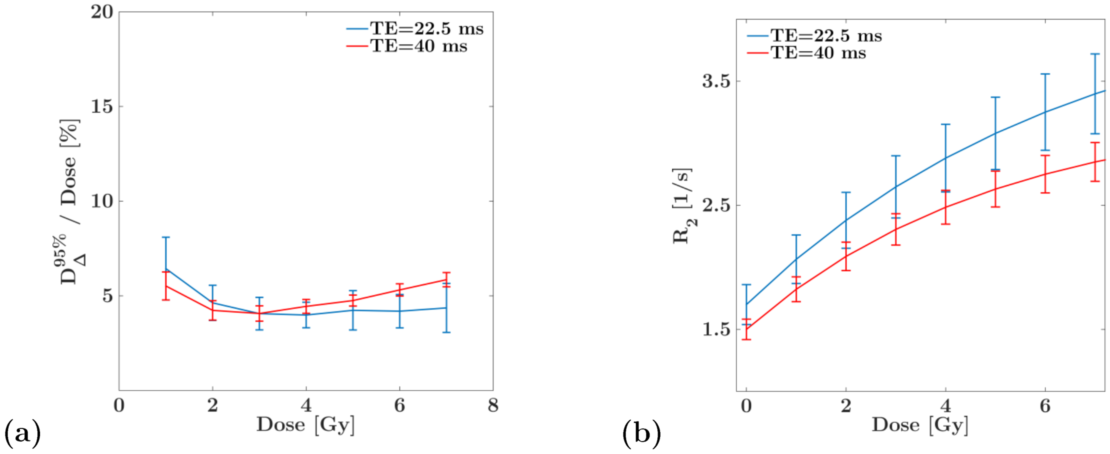

Figure 29. (a) Relative dose resolution for a set of 2×18 calibration flasks irradiated with doses between 0 and 7 Gy. A CPMG mulit-SE sequence with $TR = 3\ s$ and two different $TE = 22.5\ ms$ (blue) and $TE = 40\ ms$ (red) with a slice thickness of 1 mm and 2 mm was used for image acquisition. (b) Mean calibration curves acquired using the same parameters as for (a). Note that vertical bars do not correspond to dose uncertainties but should rather describe the variability of calibration curves between different PGD batches.

3.1.5 *B_1 and B_0 inhomogeneities*

The influence of local B_1 and B_0 field inhomogeneities on quantitative T_2 measurement were evaluated for a central slice of a *gel tumor* uniformly irradiated with 4 Gy (Section 2.5.5 (c)). Measurement parameters were set as suggested by Schuenke *et al* 2017. For comparison, a quantitative T_2 map of the same slice was also acquired. Corresponding maps are visualized in Figure 30 in which an additional line profile along a central region of the sensitive *gel tumor* volume (Figure 30(d)) is shown. Uncertainties of ΔB_0 are given in parts per million (ppm) and correspond to frequency shifts of individual voxels with respect to the static magnetic field B_0. Deviations in B_1 are given in relative flip angle maps (ΔFA) and are normalized with respect to an optimized reference flip angle. Deviations can then be calculated by simply multiplying any previously defined flip angle with ΔFA. Mean values for B_0 and B_1 inside the gel sensitive volume amount to 0.033 ± 0.455 ppm and 1.035 ± 0.021, respectively. The evaluated line profile showed both, an increase of ΔB_0 (from approx. -0.41 ppm to 0.06 ppm) and of ΔFA (ranging between 3.1% and 6.1%), while the corresponding T_2 profile showed only minor variations ($369 - 367$ ms). These variations in both, B_0 and B_1, are comparable with those reported in literature for smaller phantoms and are known to have only a minor influence on quantitative polymer gel dosimetry (Vandecasteele and De Deene 2013d). As a result, uncertainties caused by local field inhomogeneities were not taken into account and therefore no additional WASABI measurement was performed.

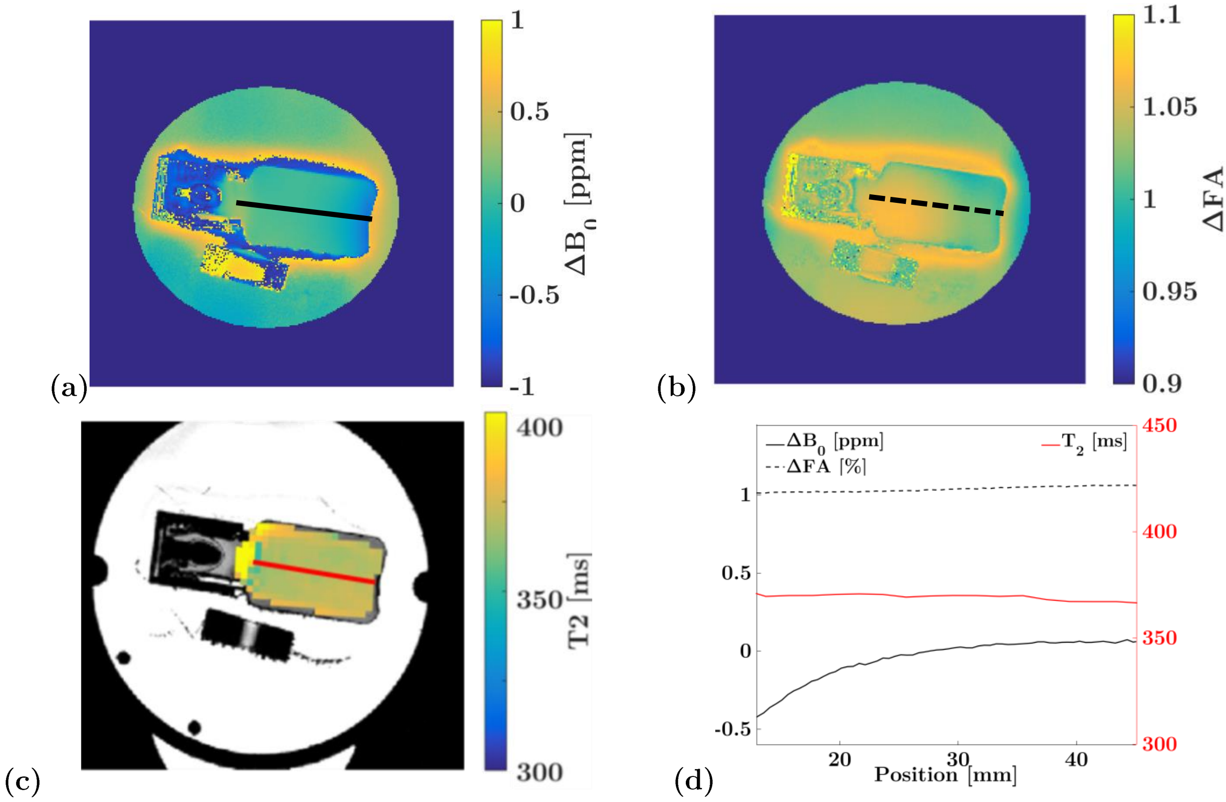

Figure 30. Uniformly irradiated *gel tumor* measured inside the water-flow phantom. Images are viszualized for (a) ΔB_0, (b) ΔFA and (c) T_2. For clarity,the T_2 acquisition is superimposed to a high-resolution MR image. (d) Line profiles along a central line for ΔB_0 (-), ΔFA (--) and T_2 (-). The left y-axis correpsonds to both, ΔB_0 and ΔFA while the y-axis on the right correpsond to T_2 values. No significant correlation between local filed inhomogeneities and the T_2 values was found.

3.1.6 *Dose rate dependence*

The dose rate dependence was evaluated by performing two different dose delivery schemes featuring: (i) continuous irradiation with $1 \times 520\ MU$ and (ii) fractionated irradiation with $4 \times 130\ MU$ and breaks of $\Delta t = 60\ s$ between two subsequent fractions. The irradiation was performed using the cylinder phantom with two *gel tumors* of the same batch. Therefore, production, storage and evaluation were identical and allowed to quantitatively compare both measurements. As visualized in Figure 32, quantitative comparison between (i) and (ii) showed no significant dose differences and no systematic trend could be identified by the analysis of representative dose profiles. A *gel tumor* difference image was additionally taken to generate a dose differences histogram (Figure 31). A Gaussian fit was applied to the data and the calculated mean dose difference was rather low ($\Delta D_{mean} = 0.01 \pm 0.07\ Gy$).

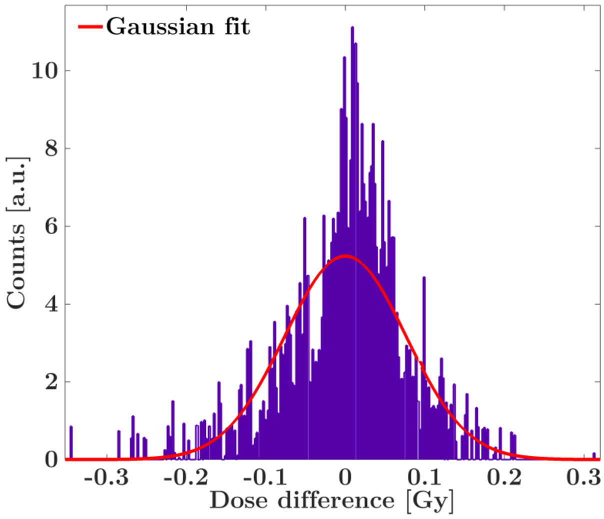

Figure 31. Dose difference histogram for two *gel tumors* irradiated either continuously ($1 \times 520\ MU$) or in a fractioned way ($4 \times\ 130\ MU$, 60 s breaks). A total of 1170 voxels were evaluated resulting in a mean dose difference of $\Delta D_{mean} = 0.01 \pm 0.07\ Gy$.

3.1.7 *Summary*

In the following, a brief point-like summary is given to point out important findings of the preceding Sections 3.1.1-3.1.6:

1. BAREX^{TM} was found to be the most suitable material for application in the porcine lung phantom in combination with the implemented workflow
2. Temperature fluctuations can be kept to a minimum by using the water-flow phantom
3. The optimized evaluation parameters for the irradiation scheme are:

   Protocol 1 (small-field irradiation): $TR = 3\ s$, $TE = 22.5\ ms$, $VS = 1 \times 1 \times 1\ mm^3$
   Protocol 2 (uniform irradiation): $TR = 3\ s$, $TE = 40.0\ ms$, $VS = 2 \times 2 \times 2\ mm^3$

4. The mean dose resolution amounts to $4.75\% \pm 0.75\%$
5. The influence of uncertainties on quantitative polymer gel dosimetry caused by local field inhomogeneities and dose rate variations are only of minor importance and can therefore be neglected.

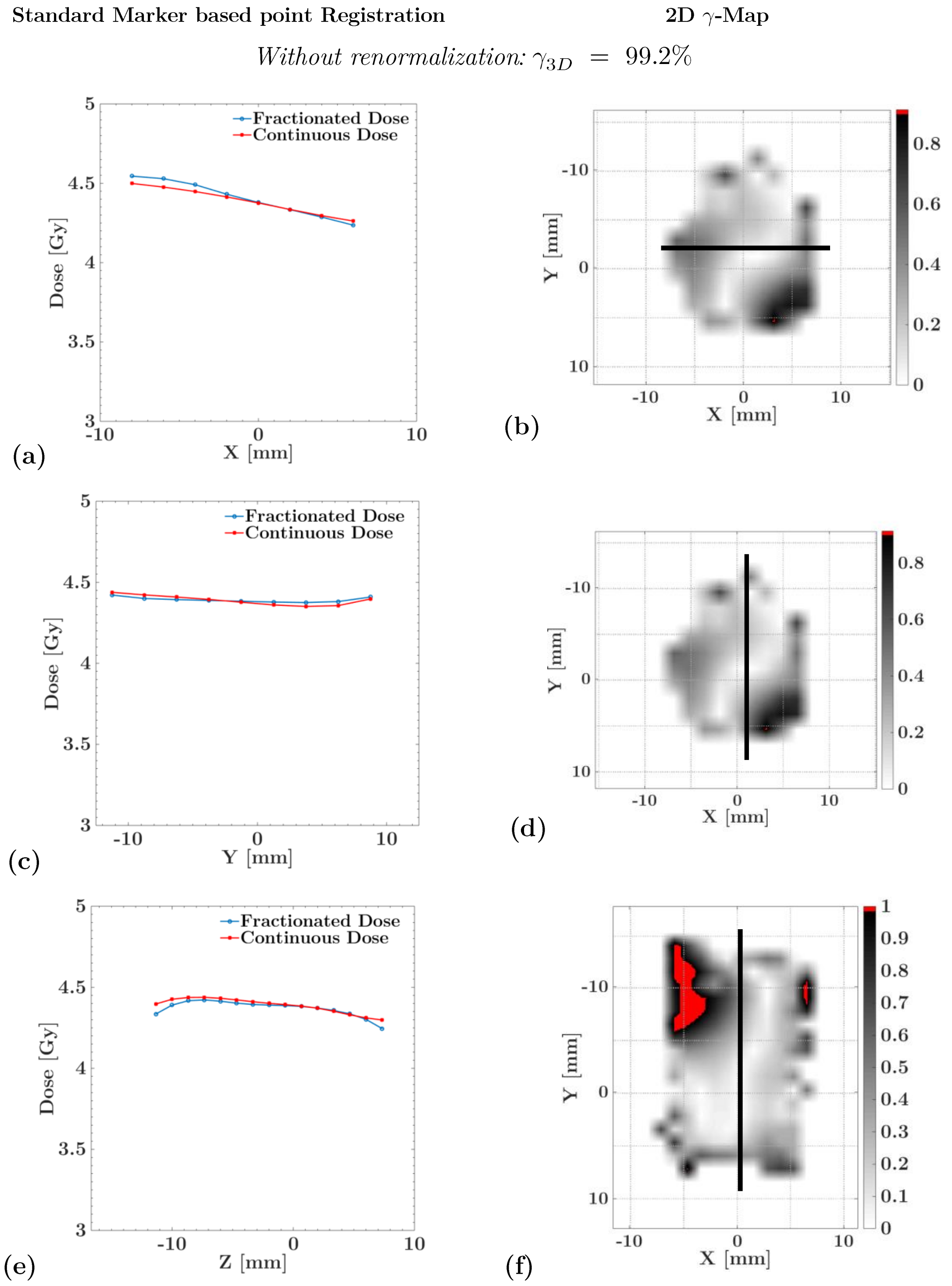

Figure 32. Uniform *gel tumor* irradiation for two different fractionation schemes. Dose profiles along the three main axis (black line, right column) of the *gel tumor* ((a),(c) and (e)) for a fractioned (blue) or continuous (red) dose delivery. Corresponding 2D-γ-maps ((b),(d) and (f)) are displayed as well with areas failing the 3%/3 *mm* γ-criterion marked in red. It should be mentioned that the calculated dose distribution was not renormalized as this would significantly influence the results.

3.2 Accuracy of gel dosimetry

Two sets of experiments were performed to check the accuracy of the PGD within the cylinder phantom. These include the water- or the lung-insert combined either with a uniform or a small-field irradiation. Additional point dose measurement with a diode at the center showed only small deviations of 0.46% and 0.27% for the uniform and 2.21% and 1.36% for the small-field irradiation as compared to the planned dose.

The influence of the TV filter on the dose distribution of a small-field and uniform irradiation is displayed in Figure 33. It displays profiles for both R_2- and dose values along a central slice. For the uniform irradiation (a), profiles showed only minor differences in the flat area while steep dose gradients are not significantly influenced by the filtering process, as visible for the small-field irradiation (b). However, the effect of the data filtering becomes more pronounced after converting the T_2-signal to dose. Nevertheless, the filtered data showed less noise in the flat area while the shape and position of the dose gradients are maintained.

The measured *gel tumor* experiments were evaluated and compared to the TPS-based dose distribution. This was performed for the filtered but non-renormalized data. Corresponding results are summarized in Table 1.

Table 1. A comparison between measured and calculated dose for both small-field and uniform irradiations using the cylinder phantom with either the water or the lung insert. Absolute dose values for the high-dose region are given as mean ± *SD*. n is the number of evaluated voxels in the respective region.

Phantom insert	**Measured** $[Gy]$	**Planned** $[Gy]$	**Deviation** [%]
Uniform irradiation			
Water (n=1480)	4.14 ± 0.23	4.00	3.6 ± 5.8
Lung (n=1267)	4.22 ± 0.25	4.00	5.5 ± 6.1
Small-field irradiation (maximum)			
Water (n=2)	5.63 ± 0.02	5.00	12.6 ± 0.3
Lung (n=3)	5.66 ± 0.01	5.00	13.2 ± 0.2

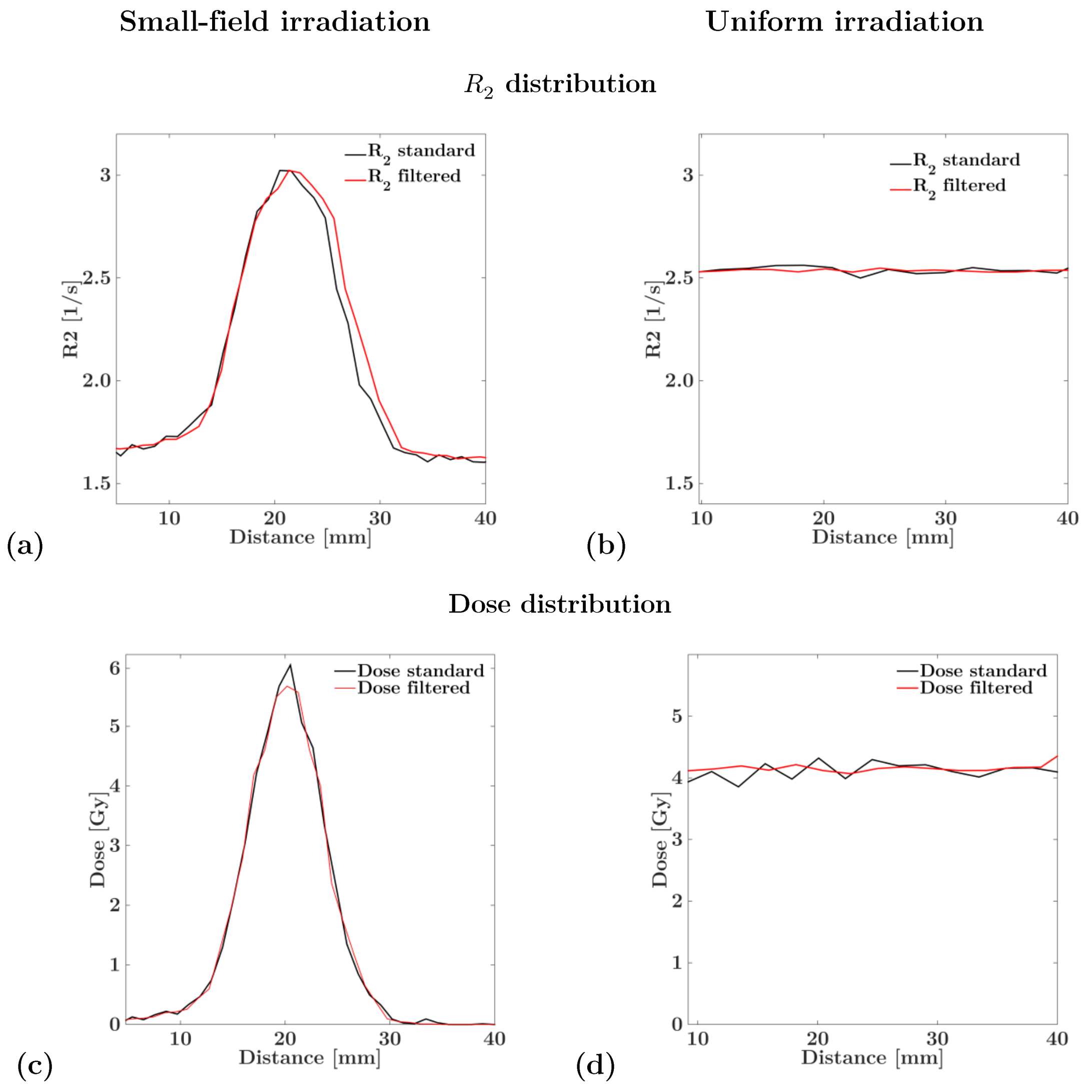

Figure 33. The influence of image filtering for a small-field irradiation ((a) and (c)) and a uniformly irradiated *gel tumor* ((b) and (d)) inside the cylinder phantom using the water-insert. R_2 profiles ((a) and (b)) show only minor differences. While the mean dose value in case of a uniform irradiation for the filtered and unfiltered data differs by less than 0.2%, a larger contribution of noise is visible in the dose distribution for the unfiltered data (d). The shape and positions of dose gradients, however, remained unchanged (c).

The calculated, measured and renormalized dose distribution along the three main axes of the irradiated *gel tumor* volume are displayed in Figure 34 for the water- and lung-insert for the case of the small-field irradiation. Due to the high positioning accuracy of better than 1 mm, only the SMR was applied. Independent of the type of insert, the shape and position of the measured dose profile agreed well with the calculated data. High γ-passing rates of 93.7% and 97.1% for the water- and lung-insert, respectively, were obtained. Performing a diode-based renormalization further increased the γ-index acceptance rate to 98.5% and 99.9%, respectively.

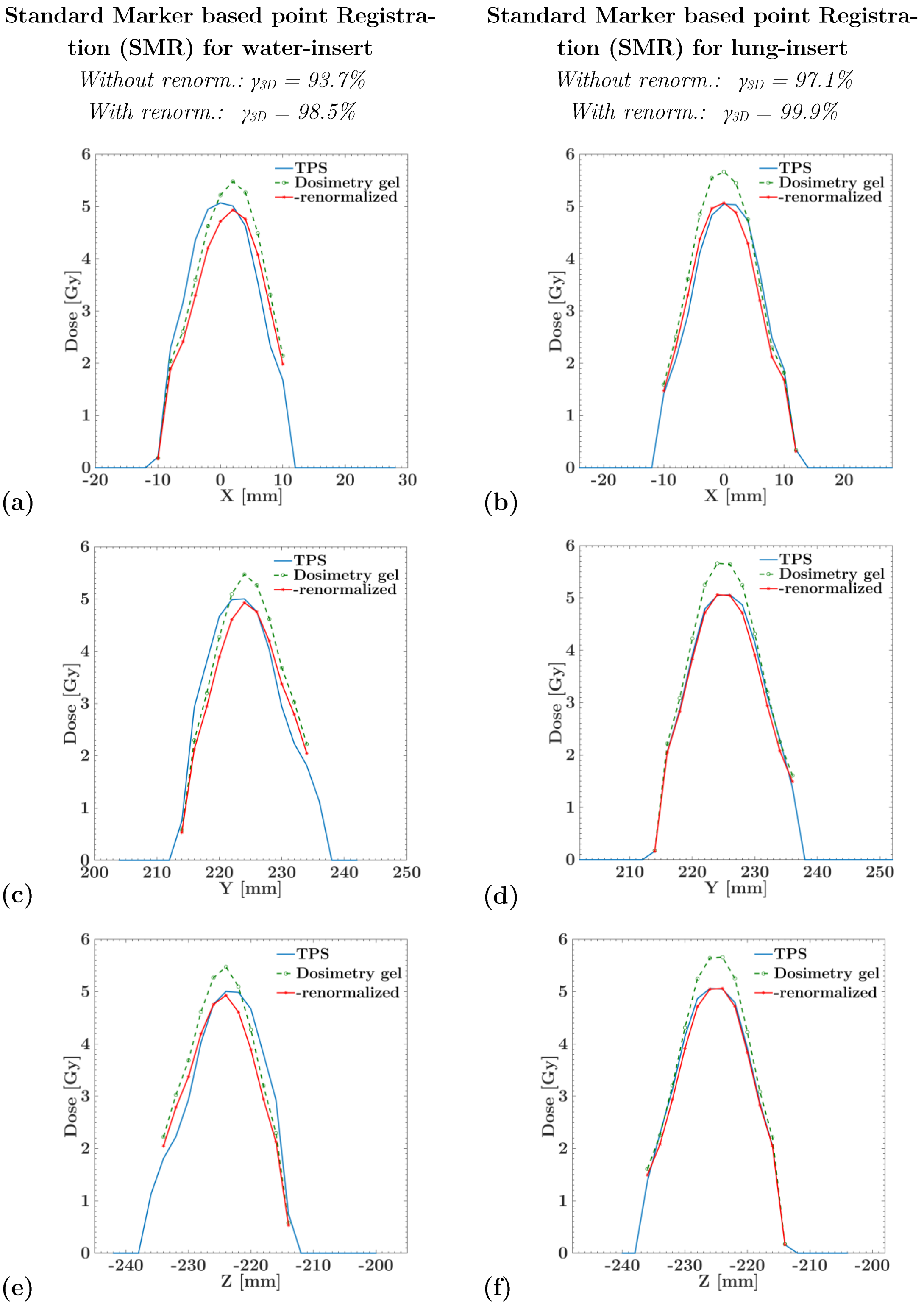

Standard Marker based point Registration (SMR) for water-insert

Without renorm.: γ_{3D} *= 93.7%*

With renorm.: γ_{3D} *= 98.5%*

Standard Marker based point Registration (SMR) for lung-insert

Without renorm.: γ_{3D} *= 97.1%*

With renorm.: γ_{3D} *= 99.9%*

Figure 34. Small-field irradiation using the cylinder phantom with either the water-((a), (c) and (e)) or the lung-insert ((b), (d) and (f)). Measured and calculated (blue) dose profiles using only the SMR are shown along the three main axis of the *gel tumor* without (green) and with (red) renormalization. Renormalization is based on a 1D point dose measurement at the dose maximum. By the renormalization, the γ-index increased from 93.7% to 98.5% for the water- and from 97.1% to 99.9% for the lung-insert, respectively.

3.3 Feasibility of 3D gel dosimetry inside the dynamic lung phantom

As the lung phantom has not been previously used with an externally attached *gel tumor* flask, its motion amplitude was evaluated for different locations. The *gel tumor* flask was attached to the mediastinum of the lung (i) close to the heart or (ii) close to the water-filled diaphragm. 4D-CT images were acquired and the corresponding amplitude was measured. *Gel tumor* flasks located very close to the heart did only show small motion amplitudes (in the order of less than 1 cm peak-to-peak). On the other hand, when the *gel tumor* was located closer to the diaphragm, a significantly larger motion amplitude is detected. In this case, tumor motion can exceed peak-to-peak amplitudes of up to 4 cm. It should be kept in mind, however, that the motion amplitude and pattern does also depend on the quality of the porcine lung, which may differ from experiment to experiment.

A total of three independent experiments using a small-field irradiation were evaluated to check the feasibility of the PGD within the porcine lung phantom. Since each experimental setting used a new porcine lung, exact reproduction of the *gel tumor* position inside the lung was not feasible. In addition, separate batches of dosimetry gel were used for each experiment making a quantitative comparison between the measurements difficult. For all experiments, the *gel tumor* was sewed to the mediastinum at a position located close to the diaphragm to assure sufficiently large motion amplitudes. The measured data were renormalized based on the maximum dose of the treatment plan as it was not possible to perform absolute dose measurements with a diode. Both, the calibration flasks and the *gel tumors* were stored inside the thermobox two hours prior to and during the quantitative T_2 evaluation since the water-flow phantom was not available at this time. MR *protocol 1* was used for image acquisition. The results of the individual experiments are displayed in Figure 35 for the static *gel tumor*, in Figure 36 for the *gel tumor* with motion but no motion compensation, and in Figure 37 for the *gel tumor* with motion-compensation by gating.

For the static *gel tumor* irradiation (Figure 35) a comparison between planned and measured dose profiles already showed good agreement if only the SMR was applied. However, a clearly visible geometrical shift in the order of patient positioning uncertainties was present. Performing additionally the APR significantly increased the agreement and both shape and position of the dose profiles could be well reproduced. 3D γ-evaluation increased the passing rate from 80.7% to 90.4%.

In case of the moving *gel tumor* without any motion-compensation (Figure 36), 4D-CT data showed a dominant motion in z-direction of 25.0 mm. *Gel tumor* motion in x- and y-direction was less pronounced (3.4 mm and 7.4 mm, respectively). As a result, large deviations in the comparison of measured and calculated doses were expected in z-direction. When only the SMR was taken into account, the 3D γ-index did not exceed 61.0%. In contrast to the static case, additional APR did also not improve the agreement significantly (3D γ-index 63.1%). Further analysis of the dose profiles including corresponding 2D γ-maps clearly showed an over-dosage in regions of large dose-gradients. This effect is especially pronounced in z-direction.

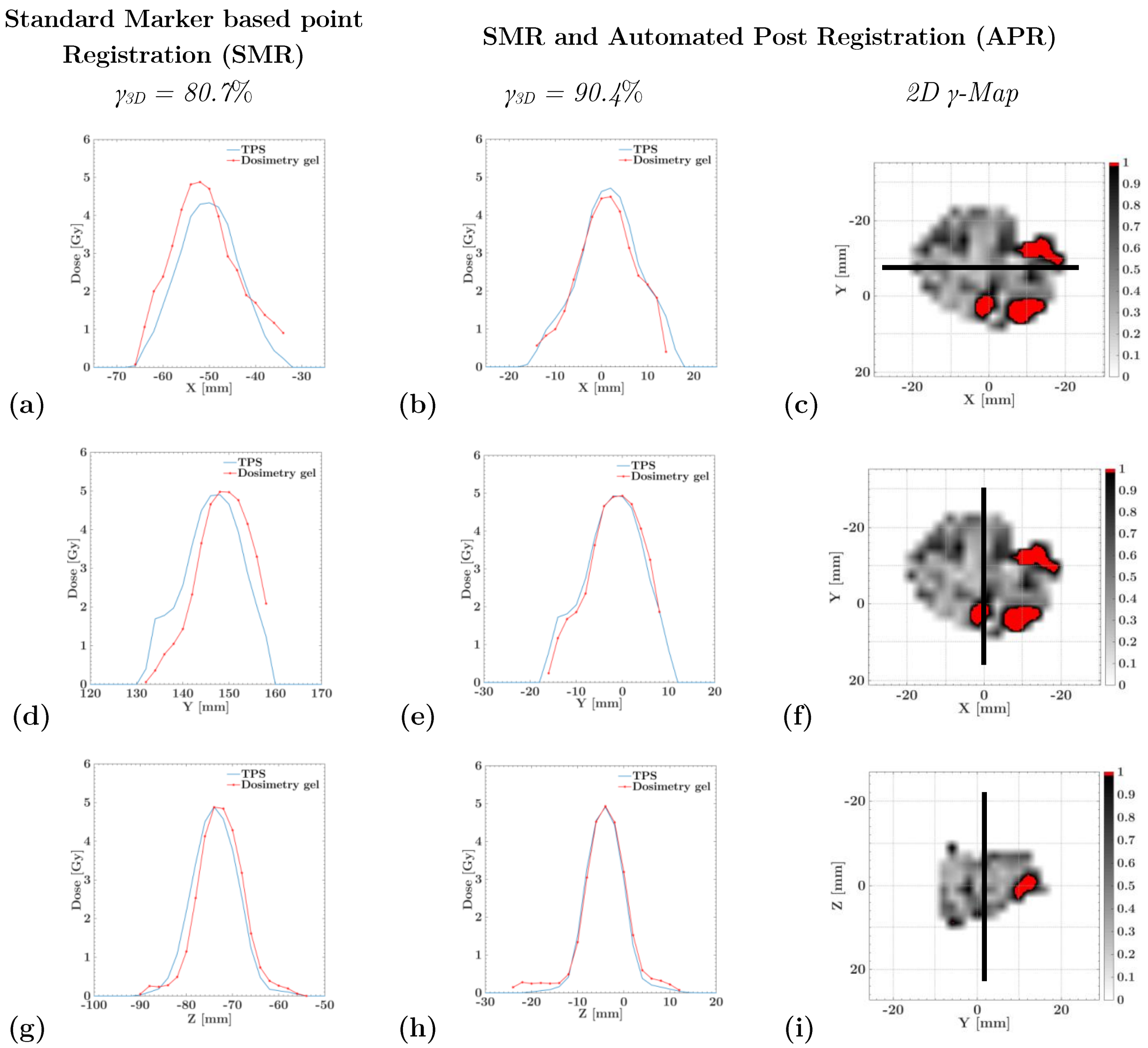

Figure 35. Static *gel tumor* irradiation with a field size of $1 \times 1\ cm^2$ performed in the porcine lung phantom. Calculated and measured dose profiles are shown along the three main axis of the phantom for the SMR ((a), (d) and (g)) and after APR was applied ((b), (e) and (h)). Additionally, 2D-γ maps are displayed ((c), (f) and (i)), showing regions where the γ-criterion is violated in red. The resulting positioning shift amounts to 1.54 mm in x-, 1.42 mm in y- and -1.03 mm in z-direction. As a result, APR-based image registration increased the 3D γ-index calculation from 80.4% to 90.4%.

Keeping in mind that the motion amplitude is comparable to the field size, an under-dosage in the central region and an over-dosage in the periphery of the *gel tumor* is expected. This effect is referred to as *dose-smearing.* By performing the renormalization to the maximum value of the planned dose, the under-dosage within the central region is compensated for while the measured dose profile in the direction of dominant motion is significantly broader than the calculated profile. Therefore, dose measurements without renormalization were additionally compared to the calculated profiles (see Figure 36, column 4) and, as expected, the measured profiles show a clearly visible *dose-smearing* in the central region of the *gel tumor.* As a consequence, the dose maximum is only 50% of the planned dose maximum and the corresponding γ-index of 74% was still relatively low.

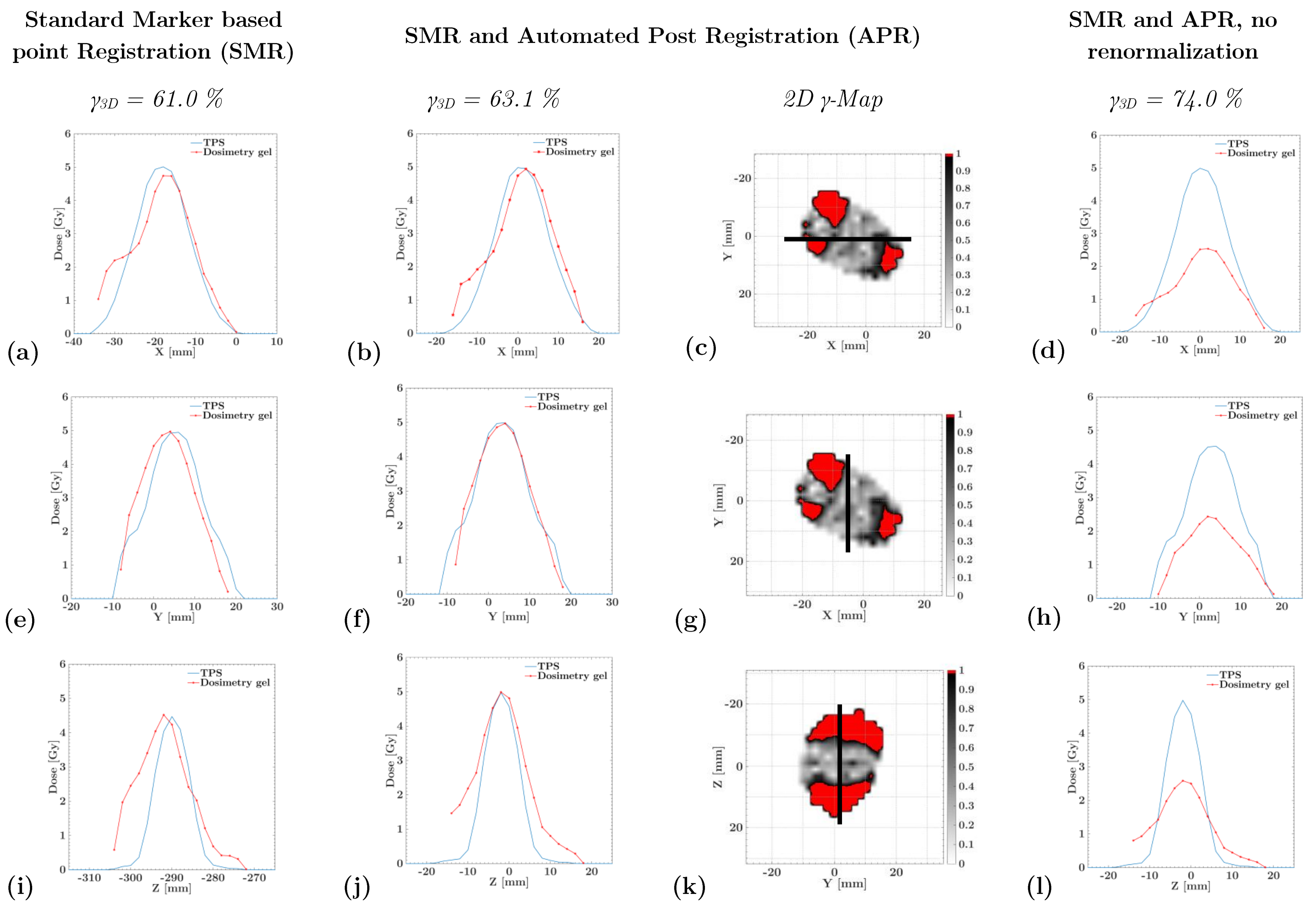

Figure 36. Moving *gel tumor* irradiation with a field size of 1 × 1 cm^2 performed inside the porcine lung phantom without motion-compensation. Calculated and measured dose profiles are shown along the three main axis of the phantom for the SMR ((a), (e) and (i)) and after APR was applied ((b), (f) and (j)). Additionally, 2D-γ maps are displayed ((c), (g) and (k)), showing regions where the γ-criterion is violated in red. The resulting shift of the dose maximum after SMR was -1.97 mm in x-, 0.1 mm in y- and 0.61 mm in z-direction. Additionally, dose profiles without renormalization ((d), (h) and (l)) showed the predicted *dose-smearing* effect in direction of dominant motion. All evaluations methods show only poor passing rates for the γ-index.

For the moving *gel tumor* including motion-compensation by a gated irradiation (Figure 37), *gel tumor* motion during irradiation could be significantly reduced from 8.4 *mm* in x-, 14.4 *mm* in y- and 24.7 *mm* in z-direction to 1 *mm*, 3.6 *mm* and 6 *mm*, respectively. As a result, dose profiles agreed much better for the SMR with the calculated data as compared to the uncompensated case. However, a clearly visible shift in the direction of the most dominant motion in the order of 2.0 *mm* was still visible. After this shift was corrected for by applying the APR, 3D γ-evaluation showed an increased passing rate from 72.8% to 91.3% which is comparable to the agreement for the static *gel tumor* irradiation.

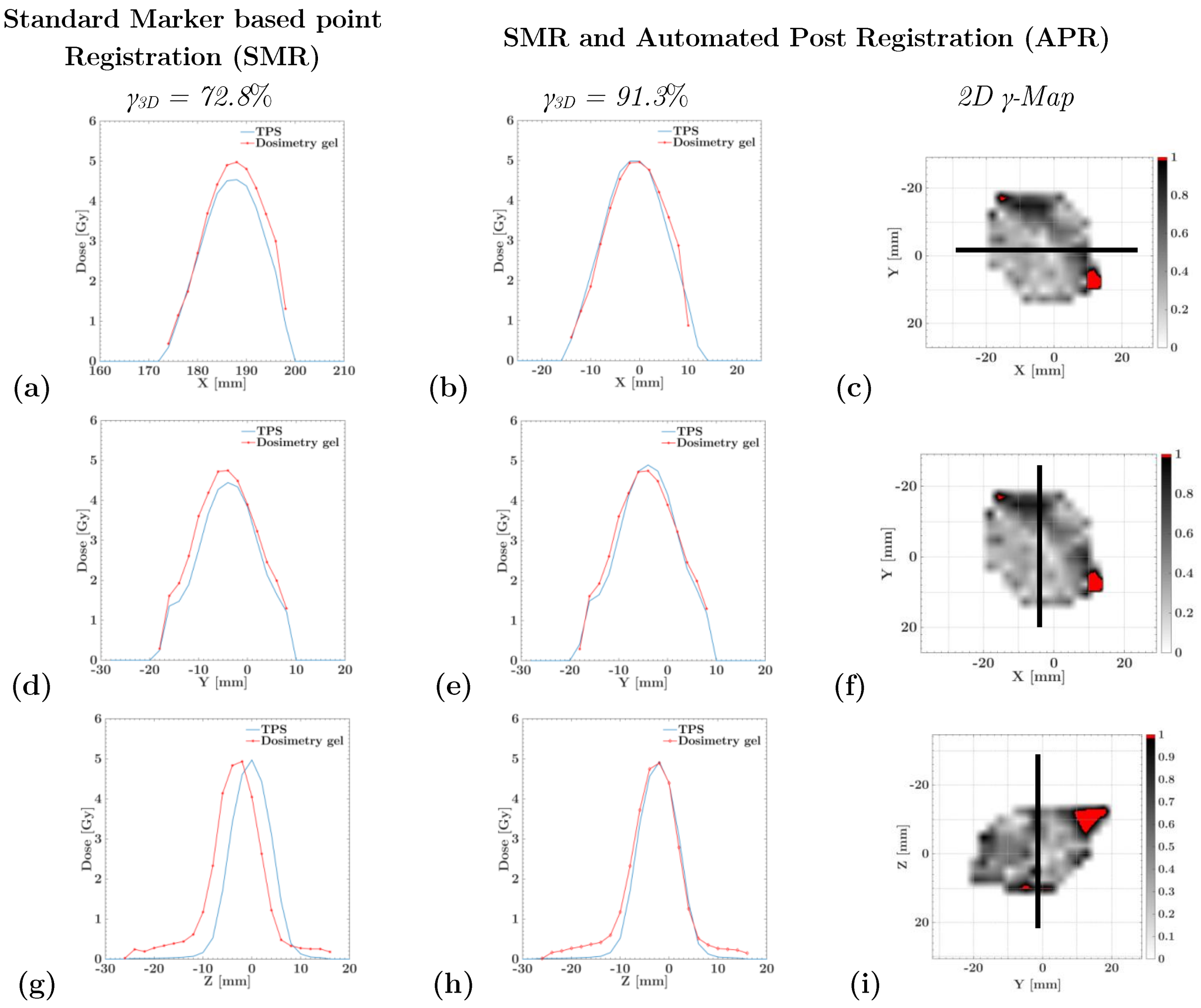

Figure 37. Gated *gel tumor* irradiation with a gating window of ±20% and a field size of $1 \times 1\ cm^2$ performed in the porcine lung phantom. Calculated and measured dose profiles are shown along the three main axis of the phantom for the SMR ((a), (d) and (g)) and after the APR was applied ((b), (e) and (h)). Additionally, 2D-γ maps are displayed ((c), (f) and (i)), showing regions where the γ-criterion is violated in red. The resulting positioning shift amounted to -0.04 *mm* in x-, 0.15 *mm* in y- and 2.00 *mm* in z-direction. As a result, APR-based image registration increased the 3D γ-index from 72.8% to 91.3%.

3.4 End-to-end tests for motion-compensated treatments

A total of three independent experiments were performed to verify clinical margin and motion-compensation concepts. Therefore, *gel tumor* irradiation was performed in a way to cover the entire volume uniformly with dose. The *gel tumor* was sewed on the mediastinum located close to the diaphragm to assure sufficient motion. The measured data was renormalized based on the maximum dose of the treatment plan as it was not possible to perform absolute dose measurements with a diode in the lung phantom. Both, the calibration flasks and the *gel tumors,* were stored inside the water-flow phantom two hours prior to and during the quantitative T_2 evaluation. Measurement parameters were set as defined by *protocol 2*. Comparisons between calculated and measured dose profiles along the three main axis of the phantom are displayed in Figure 38 for a static *gel tumor* including an isotropic 2 mm safety margin (column 1), a moving *gel tumor* without motion-compensation but including an adequately increased ITV (column 2) and for a *gel tumor* with motion including gating and an accordingly reduced ITV (column 3). In contrast to the feasibility testing (Section 3.3), this experimental setup only allowed measuring over- or under-dosages inside the *gel tumor* and is thus not sensitive to positioning-related errors. Therefore, the APR was not applied.

For all experiments, uniform *gel tumor* coverage was achieved, showing a good agreement between measured and calculated doses. Areas of significant under- or over-dosage were not present. In case of the moving *gel tumor* without motion-compensation, the calculated dose distribution was much broader as compared to the static case which consequently resulted in an increased dose to adjacent OARs. This effect, however, could be reduced by the application of a respiratory-gated irradiation.

High 3D γ-index passing rates were found in all three cases (93.6%, 87.4% and 94.4%). While the experiments for the static- and gated-case showed similar values, the agreement for uncompensated *gel tumor* motion was lower. To additionally quantify the exposure of the adjacent OARs, dose volume histograms (DVH) were calculated for the (i) esophagus, (ii) lung and (iii) heart (Figure 39). The DVHs showed that an increased ITV is accompanied with a larger dose to OARs. This effect is especially pronounced for the esophagus as it was located very close to the *gel tumor*. When gating is included in the irradiation procedure, a reduced ITV resulted in a significantly decreased dose in the corresponding OARs. To further quantify the beneficial influence of the gated treatment, a DVH was simulated for an uncompensated irradiation using the same 4D-CT data but including all phases to calculate the resulting PTV. As a result, the increased PTV is accompanied by a larger dose to OARs. It should be kept in mind, however, that location, size and shape of corresponding OARs with respect to the *gel tumor* position differed for each experiment. Therefore, the DVHs for the different cases cannot be quantitatively compared.

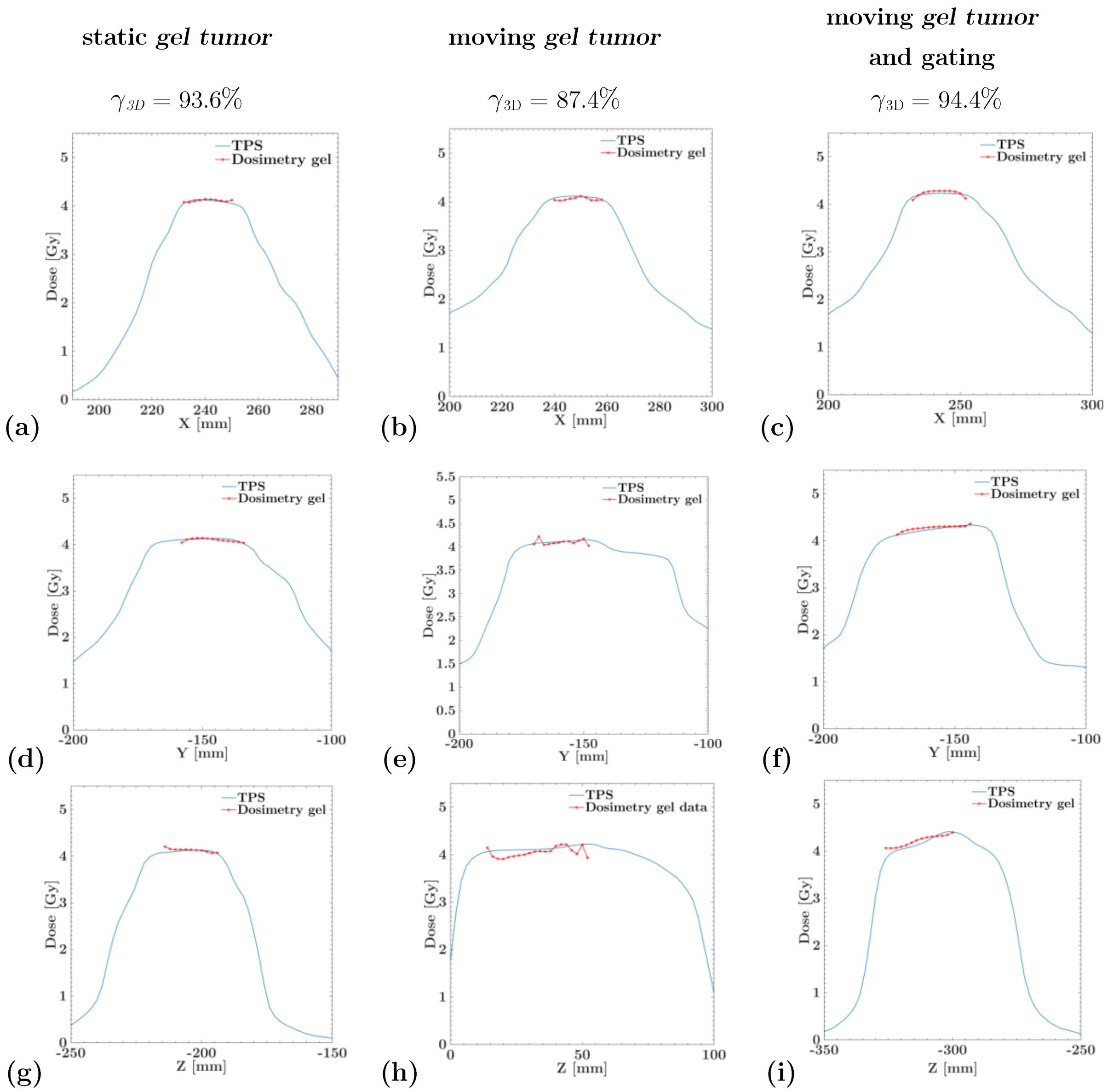

Figure 38. Uniform *gel tumor* irradiation for three different experimental setups. A comparison between the calculated and measured dose profiles along the three main axis of the phantom is shown for the static *gel tumor* ((a),(d) and (g)), the moving *gel tumor* with an additional ITV ((b),(e) and (h)) and a gated treatment with a GW of ±40% for a moving *gel tumor* with an reduced ITV ((c),(f) and (i)). For each experiment an additional 2 *mm* safety margin was added to define the PTV. Uniform dose coverage was achieved in all cases without performing the APR. Calculated doses are well reproduced resulting in high 3D γ-index values ranging between 87.4% and 94.4%.

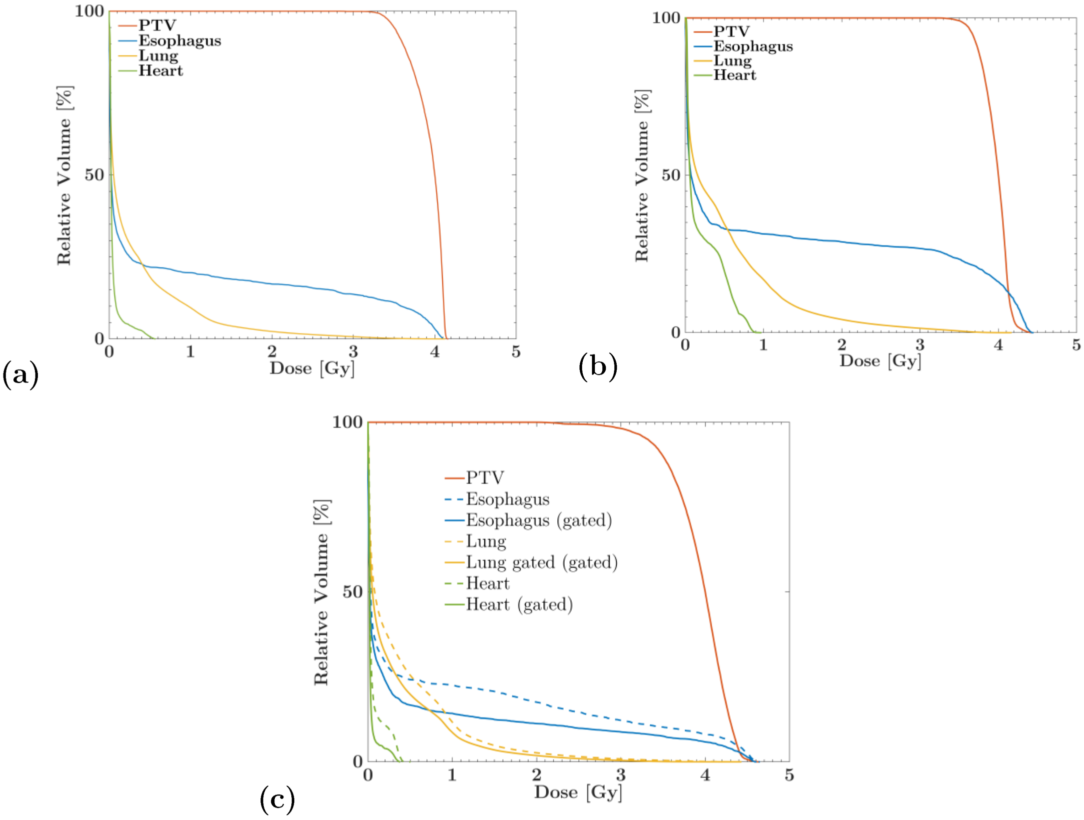

Figure 39. DVHs for tumor and OARs for a uniform *gel tumor* irradiation. Compared to the static condition (a), the irradiated normal tissue volume increased for the moving *gel tumor* without gating (b). Beam gating (c) reduced the irradiated normal tissue volume again to a level comparable to the static situation. For the gated experiment, an irradiation without gating was simulated based on the 4D-CT (dashed lines).

3.5 End-to end test for real-time markerless fluoroscopic tumor detection for treatments with beam gating

In this experimental setup, fluoroscopic imaging was included in the gating workflow to verify the actual *gel tumor* position by means of an real-time and markerless tumor detection algorithm.

As the on-board imaging detector is located in the beam, uncertainties caused by interactions of the primary beam and the imaging detector were evaluated first. This includes a repeated readout of the detector after the beam was switched off. Measurements showed large detector signal intensities of up to 30 s after the beam was switched off (this effect is subsequently termed as *after-glow).* If the x-ray tube is triggered within this period of time, both, *after-glow-* and fluoroscopic images are overlaid and could in principle cause the detection algorithm to fail. Therefore, to ensure that the *gel tumor* detection algorithm is not influenced by the *after-glow* effect, both, fluoroscopic imaging as well as the irradiation itself were performed only every forth respiratory cycle.

Furthermore, a significant beam attenuation in the order of 20% caused by the imaging detector was measured, which turned out to be independent of the field size. As no dedicated CT dataset of the detector was available, this could not be included in the TPS. Therefore, the calculated dose distribution was retrospectively corrected for by applying a constant factor of 0.80.

As for the previous experiment (Section 3.4), *gel tumor* irradiation aimed at covering the entire volume uniformly with dose. The *gel tumor* was sewed to the mediastinum at a position close to the diaphragm to assure sufficient motion. The measured data were renormalized based on the maximum dose of the treatment plan. Evaluation of the gel was performed according to *protocol 2* inside the water-flow phantom.

Both, training and real-time tracking of the *gel tumor* showed good results, which were independent of the beam angle α. A representative DRR is displayed for $\alpha = 0$ ° without and with segmentation (Figure 40 (a) and (b)). For the MTMA, the *gel tumor* detection success rate was 100%. The mean latency time for the detection and evaluation was found to be 120 ± 9 ms. The measured data of the breathing pattern, GW as well as the time points of the fluoroscopic imaging and beam-on signal are shown for a representative time interval (Figure 40(c)). Figure 40(d) – (f) displays the comparison between calculated and measured dose profiles along the three main axis of the phantom. As for the previous experiments, uniform *gel tumor* coverage and a good agreement between measured and calculated doses were achieved. The 3D γ-index passing rate of this experiment was 91.2%.

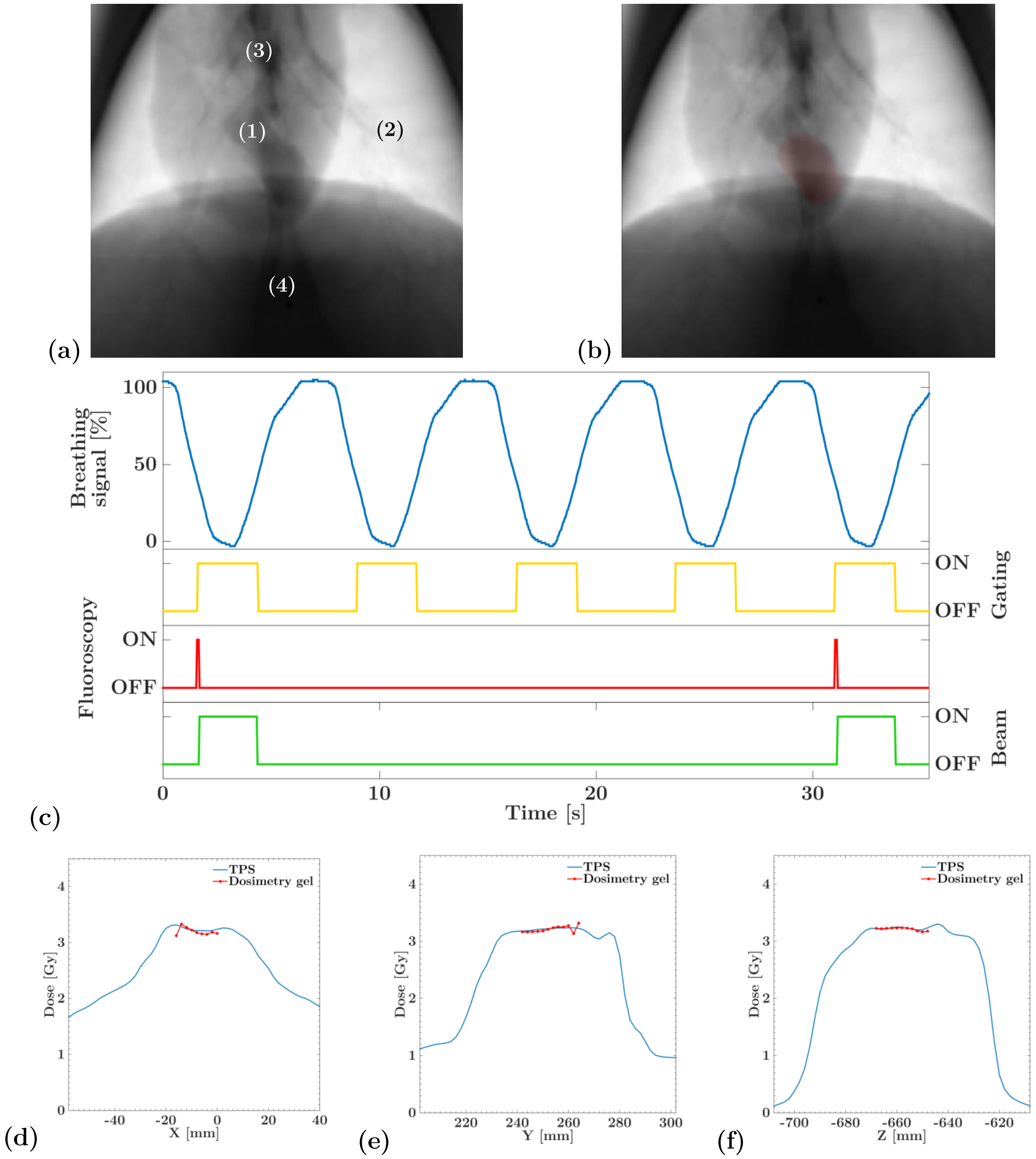

Figure 40. (a) and (b) 4D-CT-based DRR image used for the training of the MTMA. Images were calculated for a beam angle of $\boldsymbol{\alpha = 0}$ ° and show the *gel tumor* (1), the porcine lung (2), the heart (3), the diaphragm (4) as well as the corresponding automatically performed segmentation (red, only in (b)). As the actual images obtained during the experiment were not stored, comparable images are displayed. (c) The breathing signal (blue) acquired by the Anzai systems shows a very regular pattern throughout the entire treatment. The Anzai-system-based gating windows (yellow) successfully triggered the x-ray imaging system (red). Using the MTMA, the tumor position was successfully verified and the beam was switched on accordingly (green). At the end of the Anzai-signal based gating window, the beam was switched off again. For technical reasons, this procedure was applied only every forth breathing cycle (see text for details). (d)-(f) the comparison of calculated and measured dose profiles along the three main axis of the phantom shows a uniform dose coverage (no APR performed).

3.6 Validation of the 4D dose calculation for a moving target

Figure 41 displays the results of the 4D dose calculation for two static gel tumor ((a),(b) high dose and (c),(d) gradient region) as well as for a periodically moving *gel tumor* ((e) and (f)). All *gel tumors* were taken from a single batch and were evaluated with *protocol 1* inside the waterflow phantom.

For the static case, the PinPoint$^{\text{TM}}$ measurements showed only minor differences of ±1% compared to the planned dose. It turned out, however, that for the dynamic case, placing the PinPoint$^{\text{TM}}$ chamber at the isocenter position was not an optimal choice, as motion induced *dose - smearing* was already seen. Therefore, the plateau region of this measurement was renormalized to the corresponding plateau region of the planned dose.

For the static cases, measured and calculated dose distributions agreed very well in the homogeneous region as well as the dose gradient region measured in the shifted phantom. The corresponding 3D γ-index pass rates showed high values of 88.9% and 88.6%, respectively. Towards the bottle-neck of the *gel tumor* flask, however, a significant dose decrease in the order of 14% and 27%, respectively, was visible. As this region was uniformly irradiated in both experiments, the dose difference is most likely caused by a modified dose response of the gel. When the bottleneck area was not included in the γ-calculation, values increased to 93.2% and 93.5%, respectively.

When the phantom was moved by the motion robot, a significant *dose-smearing* effect in the direction of dominant motion was found (Figure 41 (e) and (f)), resulting in a dose decrease of more than 60%. If the dose calculation was performed without taking the *gel tumor* motion into account, a comparison with the measurement would result in a very poor 3D γ-index pass rate of only 54%. Applying the in-house developed dose accumulation algorithm, however, the pass rate increased to 84.6%. Similar as for the static irradiations, the bottle-neck region showed a dose reduction in the order of 13%. Excluding this region from the evaluation, the γ-index pass rate increased to 90.4%.

Static *gel tumor*

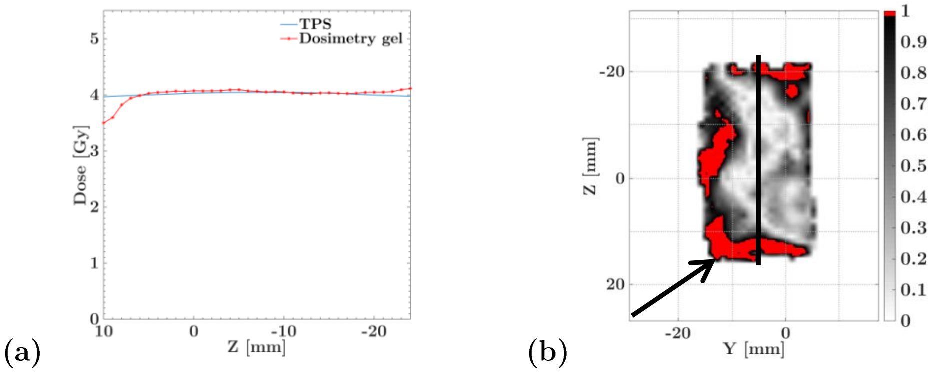

Static *gel tumor including a* 2.5 *cm* shift

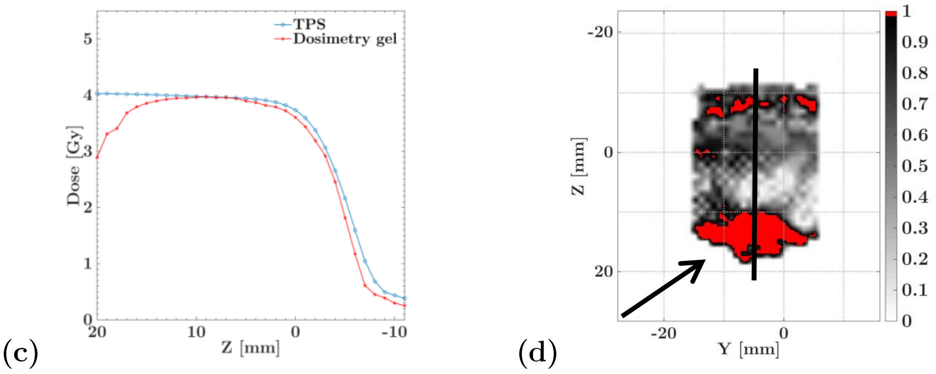

Gel tumor motion with an amplitude of 2.5 *cm*

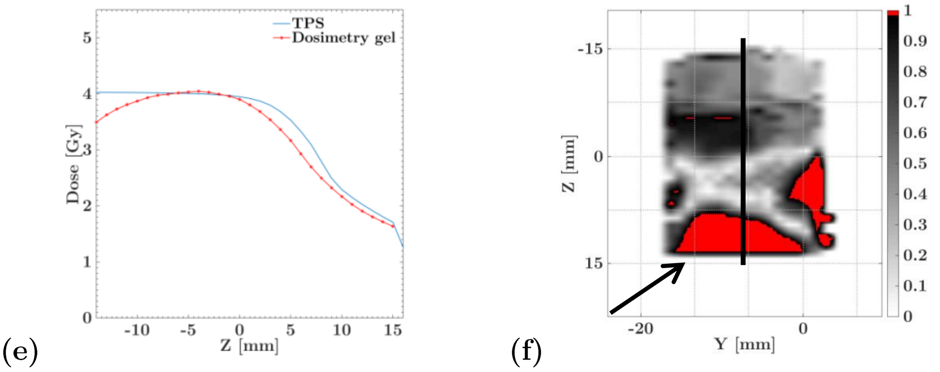

Figure 41. Results of the irradiation of the centered ((a) and (b)) and shifted ((c) and (d)) static and water-filled cylinder phantom as well as that of the periodically moving phantom ((e) and (f)). Calculated (blue) and measured (red) dose profiles are displayed along the z-direction of the *gel tumor* (black line in the 2D γ-maps on the right side). Areas, where the γ-criteria is violated, are indicated in red. When the bottle-neck region (right column, black arrow) is not included in the evaluation procedure, the γ-index increased significantly from 88.6% to 93.2% for the static case, from 88.6% to 93.5% for the shifted static case and from 84.6% to 90.4% for the dynamic case.

4 Discussion

New concepts in adaptive radiation therapy for moving targets have the potential to significantly reduce the dose to normal tissue and thus the risk of side effects while keeping high dose levels to the target. Although several approaches have been proposed in literature showing the potential of beam gating or tracking (Cui *et al* 2007, Glide-Hurst and Chetty 2014, Moser *et al* 2008), clinical implementation of these concepts presents a major challenge as the intended clinical workflow needs to be tested under realistic conditions prior to clinical application. This especially includes both, geometric- and dosimetric accuracy and precision. Although several experimental workflows have been proposed that include solid motion phantoms (Vásquez *et al* 2012) and dose measurements at certain points in 1D (e.g. by ionization chambers (Ceberg *et al* 2010), or in 2D (e.g. by films (Schmitt *et al* 2012)), dynamic phantoms usually lack the ability to measure the delivered dose in 3D. Additionally, a suitable verification workflow requires a realistic image contrast for radiological imaging e.g. by fluoroscopic imaging. This includes applications in image processing-based real-time tumor detection that can be used for tumor position verification and the generation of a corresponding gating signal. Dose verification should be ideally performed in 3D while a realistic image contrast is required for testing the implemented algorithm and workflow under realistic conditions.

In this study, we established a new workflow, which allows for breaking down patient specific problems to reproducible, workflow-oriented dosimetric measurements. This was realized by successively increasing the complexity of the experimental setup by means of (i) a geometrically well-defined cylindrical phantom with various inserts and (ii) an anthropomorphic porcine lung phantom with realistic breathing patterns. While (i) was used to implement the workflow of 3D dose verification it still shows limitations. Therefore (ii) was established as a new flexible setup to test well-established clinical concepts for static (ICRU Report No 50 1993) and moving targets (ICRU Report No 62 1999) with and without gating. Due to the realistic motion pattern of the embedded *gel tumor* and the anthropomorphic image contrast, it was possible to simulate the entire treatment chain of radiation therapy under patient-like conditions.

4.1 Polymer gel characterization

Prior to the implementation of 3D polymer gel dosimetry into the environment of the complex porcine lung phantom, which includes motion, air gaps and real tissue of different density, various experiments were performed to establish an optimal workflow for the (i) production, (ii) storage, and (iii) evaluation of the polymer gels.

As a first step, the process of polymer gel production was successfully implemented. The BAREX™ material turned out to be a suitable gel container as it showed superior properties in terms of the required oxygen barrier and chemical stability. In addition, the gel container provides soft-tissue equivalent CT image contrast and both, size and shape are well comparable to that of lung tumors in patients. By application of an optimized imaging protocol acquisition-related uncertainties could be minimized. B_0 inhomogeneities were reduced by including a manual shim before each T_2 acquisition and variations in B_1 turned out to be negligible. However, it is a crucial part of the MR acquisition to use identical imaging parameters for both, the 3D *gel* *tumor* evaluation as well as for the calibration flasks. Considering these aspects, the entire workflow of polymer gel production, storage and evaluation was successfully implemented allows applying it to a large variety of different applications. Especially the absence of a dose rate dependence makes the PAGAT-based polymer gel dosimeter a valuable tool to evaluate clinically relevant irradiation techniques such as gating with an overall dose resolution of less than 5%.

A more detailed discussion of the technical aspects of the polymer gel characterization experiments (Section 3.1.1-3.1.6) is given in the following sub-sections.

4.1.1 *Gel container materials*

Investigation of new gel container materials turned out to be a very time consuming task. Only a limited amount of suitable materials that can be combined with polymer gel dosimetry without influencing the gel response are reported in literature. If additionally, a specific image contrast, shapes and sizes are required, the number of available materials is further reduced. Flexible materials have shown to be not compatible with the gel dosimeter as both, oxygen permeability and chemical interaction with the gel itself significantly altered the dose response. Although not flexible, BAREX™ material turned out to be a near-optimal choice among the investigated materials. The gel response has been shown to be unaffected and image contrast, shape and size are well suited for experiments with the porcine lung phantom. However, the potential benefit of 3D polymer gel dosimetry is not limited to these experiments. To perform a large variety of different experimental settings, the construction of container materials of any arbitrary shape and size is desirable. A very promising material is VeroClear (Stratasys, Minnesota, USA) which is used for 3D printing. Initial 2D measurements showed a uniform dose response for uniformly irradiated calibration vessels and the calculated calibration curve was well comparable to previous results. However, the applicability for 3D dose measurements need to be further analysed, especially for uniform and small-field irradiations in 3D as well as for a quantitative comparison with the planned dose distribution.

4.1.2 *Control of temperature*

As the influence of temperature variations during MR measurements is known to significantly influence quantitative T_2 values for polymer gel dosimetry, a dedicated temperature stabilization protocol had to be developed. Initial measurements were performed inside a thermobox, where the intersection parameter $R_{2,0}$ of two calibration curves was varied by 2.6%, which caused the dose-conversion to deviate up to 25%. This shift is most likely due to temperature variations as shown by a detailed investigation by Vandecasteele and De Deene, where a temperature increase was proven to be correlated with a decreased $R_{2,0}$. The influence of this effect could be minimized using the water-flow phantom, where only minor fluctuations of $R_{2,0}$ in the order of 0.6% were found. These fluctuations, however, were assumed to be negligible as the corresponding dose uncertainty was shown to be less than the overall dose resolution. It could also be shown that these fluctuations are constant for different container positions within the phantom (e.g. bottom-, middle- or center-position). An additional temperature measurement with an electronic thermometer (EN13485, HANNA Instruments, Woonsocket, RI, USA)) inside both, gel containers and *gel tumor,* revealed identical temperature values with an accuracy of 0.1 $°C$. As a conclusion, the water-flow phantom is a versatile tool to minimize temperature drifts throughout the entire measurement volume and can therefore be used for quantitative T_2 measurements.

4.1.3 *Measurement parameters during image acquisition*

MRI-sequence parameters were optimized in such way that the total measurement time was minimized while maintaining a sufficiently high SNR. The measurements showed that it is very important that sequence parameters are identically chosen for both, calibration and 3D *gel tumor* flask, when quantitative comparison between calculations and measurement shall be performed. The optimized measurement parameters are summarized in Appendix B. In addition, it is recommended to set an isotropic image resolution as this minimizes any interpolation-related uncertainties that may occur during the post-image registration procedure.

4.1.4 *Dose resolution and calibration*

Over a dose range of $2 - 7\ Gy$ the mean relative dose resolution ($D_{\Delta}^{95\%}\ /D$) for 36 independently fabricated sets of dosimetry gel was found to be 4.75%. Although a trend to larger $D_{\Delta}^{95\%}/D$ values was identified for larger TE, no relevant differences for varying MR measurement parameters were found. However, variations of $D_{\Delta}^{95\%}/D$ were more pronounced for smaller TE and are most probably caused by the applied measurement protocol. As the smaller TE was chosen for a smaller voxel size, the lower signal intensity in each voxel causes the statistical noise to be more pronounced, which resulted in larger uncertainties.

Furthermore, reproducibility of the calibration curves was analyzed. It was found that the agreement was quite poor (Section 3.1.4, Figure 29(b)). This finding is due to the fact that minor differences in the gel fabrication procedure cannot be avoided and they may lead to differences in the polymerization characteristics. In addition, a clear shift to higher doses for shorter echo spacings was identified, which is most probably caused by the T_2 fitting procedure. In principle, a mono-exponential T_2 fit, as generally applied in polymer gel dosimetry, has shown to be a good representation of the T_2 decay. However, this must be considered only as an approximation as the underlying decay process of the magnetization should be rather described by a bi-exponential fit function. Both, the polymer- as well as the gelatine-structure have different T_2 decay constants $T_{2,gelatin}$ and $T_{2,poyl}$, respectively, and the measured T_2 value is therefore a superposition of both. However, $T_{2,gelatine}$ was shown to be unaffected by the gel irradiation and $T_{2,gelatin} \approx 40\ ms$ is therefore significantly lower than $T_{2,poly}$ (Lepage *et al* 2001). As a result, its contribution to T_2 is more pronounced for shorter echo spacings and therefore resulted in an underestimation of T_2 and an overestimation of R_2. This could also be shown for a simulated bi-exponential signal decay with

$$S_{bi}\ TE\ = \mathrm{S}_{0,\mathrm{gelatin}} \cdot \exp(-{}^{TE}\!/_{T_{2,gelatin}}) + \mathrm{S}_{0,\mathrm{poly}} \cdot \exp(-{}^{TE}\!/_{T_{2,poly}}) \tag{4.1}$$

The weighting factors $S_{0,gelatin}$ and $S_{0,poly}$ were set to 0.2 and 0.8, respectively. A T_2 acquisition was simulated by choosing 29 equidistant TE values along $S_{bi}\ TE$ and was then fitted against a mono-exponential function

$$S_{mono}\ TE\ = a\cdot \exp(-{}^{TE}\!/_{T_{2.mono}}), \tag{4.2}$$

where a is the initial signal intensity for $TE = 0$. As shown in Figure 42(a) and (b), a smaller echo spacing did cause the first term of S_{bi} to be more pronounced and therefore resulted in a smaller $T_{2,mono}$ value. As shown in Figure 42(c) a simulated calibration curve for representative values of $T_{2,poly}$ and different echo spacings could clearly reproduce the measured dose offset to larger R_2values for shorter TE (Figure 42(e)).

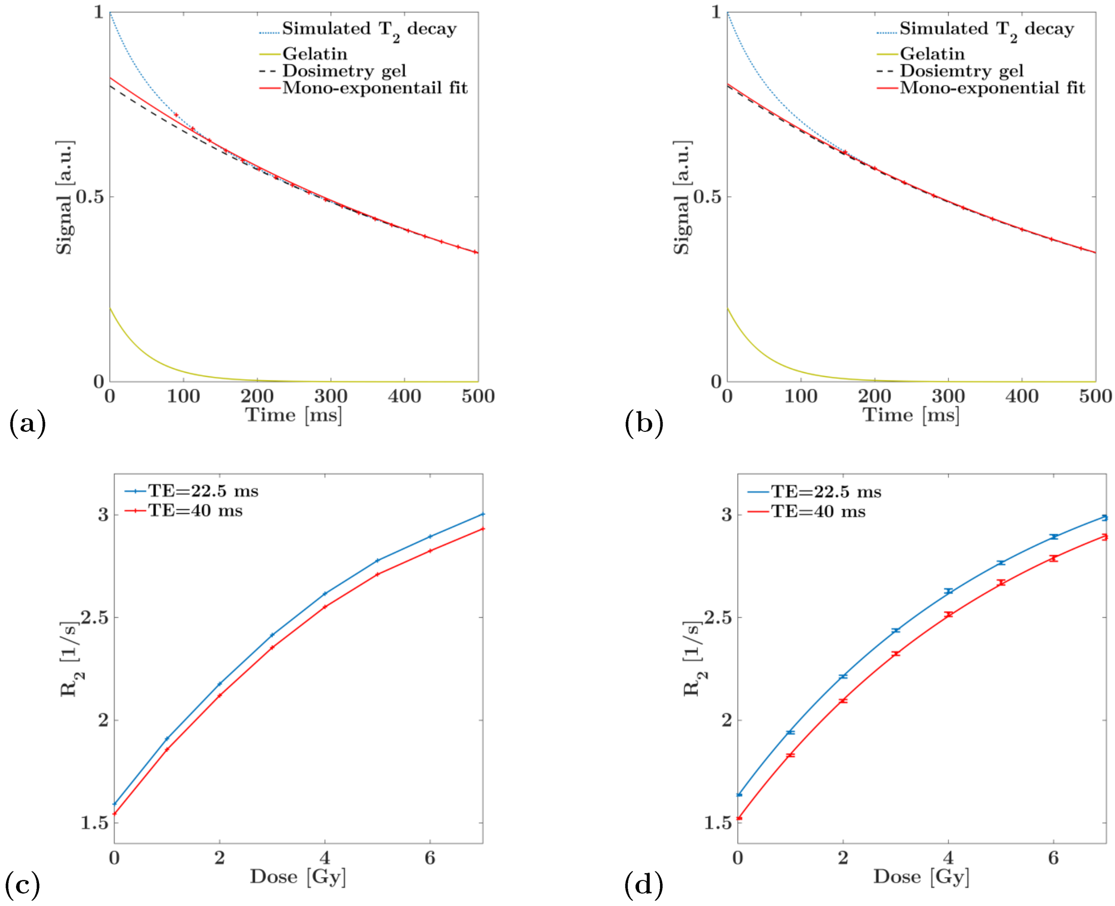

Figure 42. (a) and (b) Simulated bi-exponential T_2 decay (blue) using the decaying constants $T_{2,gelatin} = 40\ ms$ (yellow) and $T_{2,poly} = 600\ ms$ (black, dashed line). A mono-exponential fit (red) for two echo spacings ($TE_1 = 22.5\ ms$ and $TE_2 = 40\ ms$) and 32 equidistant echoes was performed. Ignoring echo 1-3 resulted in fit coefficients for (a) of $T_{2,mono1} = 580.8\ ms$ and (b) of $T_{2,mono2} = 598.0\ ms$ for TE_1 and TE_2, respectively. $T_{2,mono2}$ agreed better with the simulated polymer-based decaying constant $T_{2,poly}$. (c) Simulated calibration curve for representative $T_{2,poly}$ values for doses between $0-7\ Gy$ and echo spacings TE_1 (blue) and TE_2 (red). (d) Representative temperature controlled calibration measurement for TE_1 (blue) and TE_2 (red) also showed a clear trend to higher R_2-values for shorter TE.

Based on these investigations, it is therefore concluded that polymer gel dosimetry is a suitable tool for 3D verification of new workflows or treatment techniques, where uncertainties can easily add up to large deviations ($>D_{\Delta}^{95\%}$). The maximum dose resolution of the gel, however, should be kept in mind for the design of new experiments as e.g. a uniform irradiation of 4 Gy can only distinguish doses that differ by $\Delta D > 0.19\ Gy$. Especially for quantitative measurement it is very important to perform a calibration measurement using the same batch of dosimetry gel as well as the same MR parameters as for the measurement of the *gel tumor*.

4.1.5 *B_1 and B_0 inhomogeneities*

The influence of B_1 and B_0 inhomogeneities on the measured dose distribution was found to be negligible. The resulting dose errors for the small *gel tumor* volume were significantly lower than the overall dose resolution (1.4% as compared to 4.75%). However, this is only true for small gel containers. Uncertainties have been reported to be in the order of up to 25% for the peripheral region of larger phantoms (Vandecasteele and De Deene 2013b). It is therefore a crucial part of the evaluation procedure to previously analyze any new gel container material or gel container size in terms of B_1 and B_0 inhomogeneities prior to its application in new experiments.

4.1.6 *Dose rate dependence*

As the polymer gel was selected to verify and test clinically relevant irradiation techniques, it had to be assured that the dose response does not vary significantly for irradiations performed at different dose rates (e.g. as for an extended delivery timed for gating). The corresponding experiments showed no significant dose rate dependence for two uniformly irradiated *gel tumors* (Section 2.4.5). Dose difference amounted to $0.2 \pm 1.6\%$ of the maximum dose value and were well-comparable to uncertainties given in the published literature (Ceberg *et al* 2008). Minor differences in the 3D γ-evaluation are most likely related to positioning uncertainties. As no clear trend to higher or lower doses was identified, the obtained deviations are most probably related to statistical fluctuations and do not originate from systematic errors. The applied fractionation scheme of 4×130 *MU* with breaks of 60 *s* is considered as a realistic time pattern for the dose delivery of a clinical irradiation with four different gantry angles while a continuous dose delivery of 520 *MU* is more comparable to the implemented calibration irradiation workflow. As the irradiation technique of beam gating is a combination of consecutive beam delivery including shorter and longer breaks (e.g. caused by beam gating and gantry rotation) the dose rate dependence is expected to be in the same order of magnitude as in this measurement.

4.1.7 *Renormalization*

The applied renormalization procedure has proven to work well to compare measurements and calculations in 3D for both, static and dynamic scenarios. The agreement was especially high for experiments where an ionization chamber or diode was used. An exemplarily comparison between non-renormalized and renormalized data is shown in Figure 43. Although a uniform dose distribution was delivered, a clear offset to larger doses is visible resulting in very poor γ-passing rates of only 27.1%. Renormalization significantly improved the agreement and resulted in large γ-passing rates of 95.9%. Other experiments also showed a clear trend to higher doses of the measurement as compared to the calculations and therefore the observed discrepancy seems to be of systematic nature. This finding has also been reported in literature and is especially pronounced when calibration- and volumetric gel flasks (here: *gel tumor*) are treated differently during the experiment (Vandecasteele and De Deene 2013b). Although special precautions were taken to identify and minimize such differences by applying a dedicated protocol for production, storage, irradiation and evaluation (Section 3.1), the problem of absolute dose measurement with gels is still not satisfactorily solved yet. In spite of the applied highly-controlled conditions, a few factors still seem to be present, which can introduce uncertainties to the measurement: This includes (i) temperature differences during the irradiation and (ii) uncertainties introduced by the dose calculation of the TPS. As shown by De Deene *et al* 2006, the influence of (i) is only of minor importance for PAGAT polymer gels. However, uncertainties for the dose calculation for treatment planning of lung tumors in patients (ii) have been reported in literature (Korreman 2012). Therefore, for experiments with the dynamic porcine lung phantom (which includes various materials such as water, lung, muscle tissue and PMMA), dose calculations may not be as accurate as for conditions under which the gel calibration is usually performed. In principle, this uncertainty can be reduced by the insertion of an additional point dosimeter. Ongoing projects are currently evaluation the feasibility of optically stimulated luminescent dosimeters (OSLDs) being attached on the *gel tumor's* surface. This point dose measurement could be used for both, *gel tumor* renormalization as well as for cross validation of the calculated dose.

4.2 Accuracy

The overall accuracy for the implemented polymer gel dosimetry workflow was investigated under well-defined conditions. A cylinder phantom was used containing either water- or lung equivalent material.

1D dose measurement showed good agreement with the planned dose for both, the water and the lung-insert, and thus confirmed the accuracy of the dose calculation algorithm. Remaining errors for the small-field irradiation are most likely caused by positioning uncertainties of the diode inside the *gel tumor*. In addition, the applied TV filter has proven to be a suitable tool to ensure that both, the position and shape of strong dose gradients was preserved while the data in regions of a uniform dose distribution showed less noise. This is especially important when 3D γ-evaluations for quantitative comparison of measured and calculated data are performed. Gamma values may be significantly underestimated, if the measured dose distribution contains noise and it would therefore lead to a misinterpretation of obtained agreement. This effect was found to be especially pronounced for regions of shallow dose gradients (Low 2010). Absolute dose measurement for a uniformly irradiated *gel tumor* showed systematic deviations to higher doses in the order of 3% to 6% as compared to the planned dose. These deviations are well comparable to polymer gel measurements as described in literature (Vandecasteele and De Deene 2013a). Agreement between the standard deviation and the corresponding dose resolution are quite good (4.4% and 6%, respectively). Improvement can in principle be achieved by increasing the number of averages for the MR acquisition. However, this is accompanied by a significantly increased measurement time and was therefore not performed.

SMR without renormalization

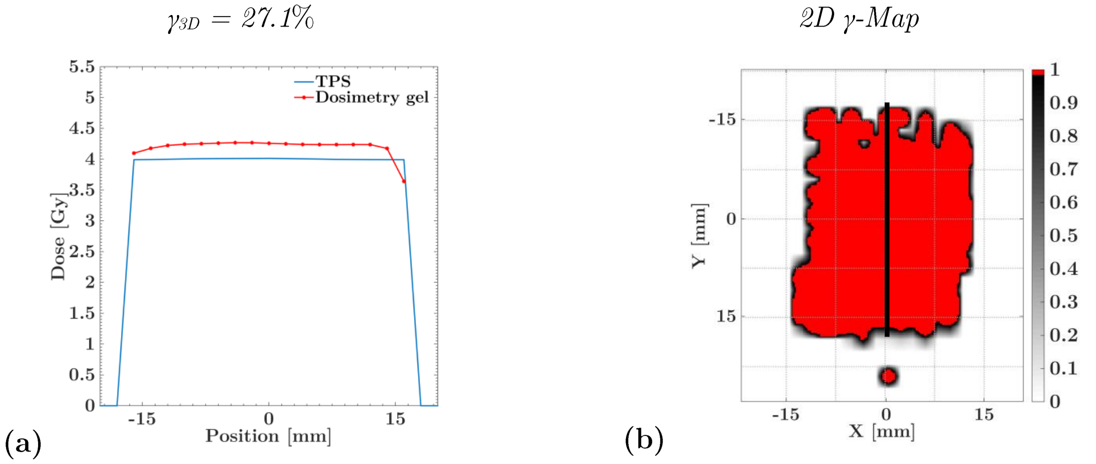

SMR with renormalization

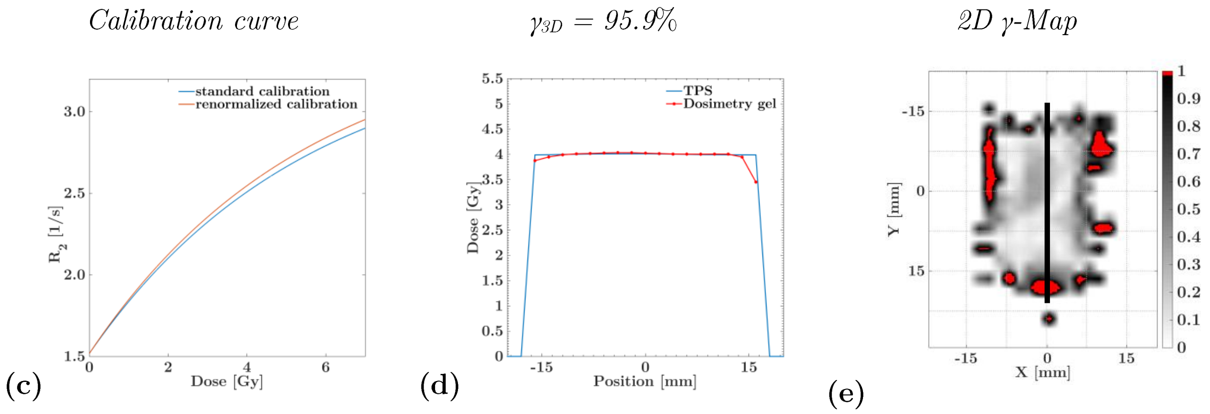

Figure 43. (a) Uniform *gel tumor* irradiation performed inside the cylinder phantom. Calculated (blue) and measured (red) dose profiles are shown along the y–axis of the phantom for the non-renormalized (a) and renormalized (d) measured dose distribution. Corresponding calibration curves are displayed in (c). Additionally, 2D-γ maps are displayed ((b) and (e)), showing regions where the γ-criterion is violated in red. As a result, the diode-based renormalization procedure significantly increased the 3D γ-index calculation from 27.1% to 95.9%.

Investigation of the non-renormalized small-field *gel tumor* irradiation revealed good agreement between measured and planned dose. Location of the dose maximum and shape of the dose profile were well reproduced and not influenced by the TV filter. However, a shift towards higher dose values was still observed without renormalization. This shift is especially pronounced in the high-dose region. However, the number of voxels at the maximum is very small and therefore the agreement is strongly affected by statistical fluctuations of the measured T_2 values. Applying the proposed renormalization procedure resulted in very high γ-passing rates of 98.5% and 99.9%, respectively, for the water- as well as for the lung-insert.

As a result of these investigations, it can therefore be concluded that the entire workflow of gel fabrication, storage, irradiation, and MR-based evaluation using the optimized protocol and imaging parameters was successfully implemented within the specifications necessary for applications in radiation therapy. In addition, the post-processing procedure consisting of data filtering, image registration and renormalization allows verifying both, small-field as well as uniform *gel tumor* irradiation with an overall accuracy of 5%. Even though the accuracy is lower when compared to other 1D or 2D dosimeters, polymer gel dosimeters can be used in challenging environments, which are not accessible with standard dosimeters, and provide dose information in 3D rather than 1D or 2D.

4.3 Feasibility of the experimental setup

The combination of polymer gel dosimetry and the porcine lung phantom turned out to be a versatile setting to test various treatment techniques under clinically realistic conditions. The entire chain of radiation therapy from CT acquisition to treatment planning and dose delivery was successfully implemented and the results showed very good agreement with dose calculations.

4D-CT data revealed an average *gel tumor* motion of $7.5 \pm 6.6\ mm$ in x-, $9.3 \pm 4.9\ mm$ in y- and $25.5 \pm 4.7\ mm$ in z-direction (mean ± SD). All measurements showed sufficiently large *gel tumor* motion and were well comparable to typical lung tumor motion amplitudes described in literature (Knybel *et al* 2016). As the agreement between calculations and measurements for the gated case was very high, it is concluded that the motion trajectory did not significantly change between 4D-CT and irradiation. Various experiments showed that this can only be achieved if the cylindrical BAREX$^{\text{TM}}$ *gel tumor* flask is aligned parallel to the axis of dominant motion (z-direction) and if it is located between the right and left lobe of the lung. Sewing the *gel tumor* with an orientation perpendicular to the z-direction revealed a significant drift of the *gel tumor* position and should therefore not be used if reproducibility is crucial for the experiment. However, even if the motion trajectory is not significantly changed, there may still be some variations. Two independent effects influencing the *gel tumor* dynamics were identified: (i) during transportation between the CT and the LINAC, the external vacuum pump caused the lung volume to decrease slightly. Although this effect could be reversed by switching on the on-board vacuum system again, small changes in the *gel tumor* trajectory cannot be ruled out. (ii) The biomechanical properties of the lung may change during the experiment. As the experiment can last for up to 3 h, drying of the lung can influence the elasticity and thus the motion trajectory. However, the problem of limited reproducibility of the tumor trajectory may also occur during treatment of patients. Further analysis of this effect in the experimental as well as in the clinical setting could be realized by performing an additional 4D-CT after the irradiation or by including fluoroscopic imaging during the treatment.

Technical limitations of the experimental setting were evaluated with a small-field irradiation providing very steep dose gradients. Without *gel tumor* motion, the γ-criteria showed very good agreement of 90.4% after the APR was applied. The maximum positioning shift of $2\ mm$ is well comparable to setup uncertainties assumed in patients. The origin of this offset is most likely a combination of uncertainties in positioning, dose delivery and the registration procedure. Prior to irradiation, a CB-CT was acquired to correct for any positioning shift. However, due to the anthropomorphic and thus partly challenging soft tissue contrast and the finite image resolution, small residual positioning errors cannot be ruled out. Image registration as implemented in the post-processing procedure can additionally cause the *gel tumor* position to deviate from the plan. This may occur due to the finite image resolution of both, the CT – and MR-datasets used for image registration as well as that of the corresponding markers.

Irradiation of the moving *gel tumor* without applying any motion-compensation technique resulted in very poor agreement between measured and planned dose distribution and a significant *dose-smearing* in the direction of dominant *gel tumor* motion was found. This also showed the limitation of the applied renormalization procedure. Since the actually delivered maximum dose is already expected to be significantly lower than the planned, treatment plan-based renormalization to the maximum dose should not be performed. Although agreement in the central region is expected to be very high in this case, the *dose-smearing* effect causes the lower dose levels to be significantly shifted to higher dose values. Therefore, the passing rate of the γ-critera remains rather low ($\gamma_{3D} = 61.3\%$). If no renormalization is applied, the measured dose profile shows the expected *dose-smearing* but the γ-critera still remains similarly low ($\gamma_{3D} = 74.0\%$). This shows that the normalization procedure is only reasonable, if the relative distributions of measured and planned dose are the same, which is not the case in presence of motion.

When gating was applied, the dose distribution could be successfully restored and it showed very good agreement with a γ-criteria passing rate of 91.3%. At the level of very low dose values, mean deviations of up to 6% of the maximum Dose D_{max} were found. The source of this discrepancy was most probably a combination of (i) residual motion during the irradiation and (ii) the renormalization procedure. As the gating window was set to ±20%, residual motion during irradiation was still present, thereby increasing the dose in regions where no dose is expected to be delivered. As a consequence, the dose maximum is expected to be lowered and by applying the renormalization, the dose maximum is then overestimated and accompanied by a dose increase of low-dose regions (see previous paragraph).

The established setup has proven to be a versatile tool to measure and verify steep dose gradients under different conditions (static and gating) within a pre-defined target region. It is therefore concluded that this experimental setting can now be used to verify both, well-established and highly advanced clinical concepts for the irradiation of moving targets.

4.4 End-to-end tests for motion-compensated treatments

Clinical application requires the target volume to be uniformly irradiated while any under-or over-dosage including local cold - or hot-spots need to be avoided. In clinical application these requirements are usually taken into account by the medical physicist and the treatment planning software while quality assurance protocols are used to verify the correct delivery of the calculated plan. Plan verification, however, is usually performed on rather simple phantom settings that do not reflect the patient's anatomy or movements and therefore excluding any patient-or workflow-specific uncertainties. To take these uncertainties additionally into account and measure the effect on the delivered dose for static and dynamic target motion with and without gating, experiments with the porcine lung phantom were performed while the *gel tumor* was uniformly irradiated (see Figure 44). Results show very good *gel tumor* coverage while no relevant cold- or hot-spots are visible. The agreements with the planned dose are especially comparable for the static and the gated case ($\gamma_{3D} = 93.6\%$ versus 94.4%). Although the gated case showed slightly better agreement, it has to be kept in mind that the γ-values result from different experiments (i.e. from different batches of dosimetry gel) and differences in the order of 1% are therefore not considered to be significant (Vandecasteele and De Deene 2013b). Nevertheless, achieving this small dose discrepancy without performing the APR demonstrates the feasibility of the applied margin concept. The applied margins could successfully compensate for any setup-related errors and residual motion in both, the static and the gated case. The choice of appropriate margins was based on previous findings (see 3.3), where the maximum positioning shift amounted to $2\ mm$. Therefore, adding an additional safety margin of $\Delta PTV = 2\ mm$ to the GTV/ITV was assumed to be sufficient to ensure uniform *gel tumor* coverage in both experiments.

Analysis of the uniform dose distribution showed only minor statistical fluctuations in the order of the maximum achievable dose resolution (see Table 2). Furthermore, the dose uniformity within the irradiated *gel tumor* volume was relatively good, leading to the conclusion that the motion trajectory did not significantly vary between 4D-CT acquisition and irradiation. However, it cannot be ruled out if the maximum motion amplitude was decreased during irradiation as a uniform dose distribution would still be expected in this case.

For the dynamic *gel tumor* without motion-compensation, the PTV increased (see Figure 44) from $35.6\ cm^3$ to $96.7\ cm^3$ which is accompanied by a significant dose enhancement to adjacent OARs. This effect was especially pronounced for the esophagus as the *gel tumor* was attached to the mediastinum (see Figure 39). This location was used as a representative example and using a different *gel tumor* location would have caused the dose distribution to change also in the adjacent OARs of the new location. Including gating into the experimental setup could significantly decrease the PTV from $96.7\ cm^3$ to $62.6\ cm^3$.

Table 2. Comparison between measured and calculated dose for a uniform irradiation inside the porcine lung phantom for a static, dynamic and gated case. Absolute dose values are given as mean ± ***SD***.

Experiment	Measured [Gy] (relative dose error)	Planned [Gy]
Static	4.00 ± 0.17 (±4.3%)	4.06 ± 0.06
Dynamic	4.02 ± 0.17 (±4.2%)	4.09 ± 0.05
Dynamic + Gating	4.17 ± 0.15 (±3.6%)	4.17 ± 0.17

While the reduced PTV still showed uniform *gel tumor* coverage, the dose to adjacent OARs could be reduced. Quantitative comparison between the corresponding DVH and an additionally recalculated plan taking all phases of the 4D-CT into account (without applying gating), revealed a significant dose reduction for all OARs. Especially, the esophagus showed 30.8% less dose than for the uncompensated case. The entire experimental setting has therefore proven to be a valuable tool to verify clinically relevant workflows and new treatment techniques in a patient-like environment.

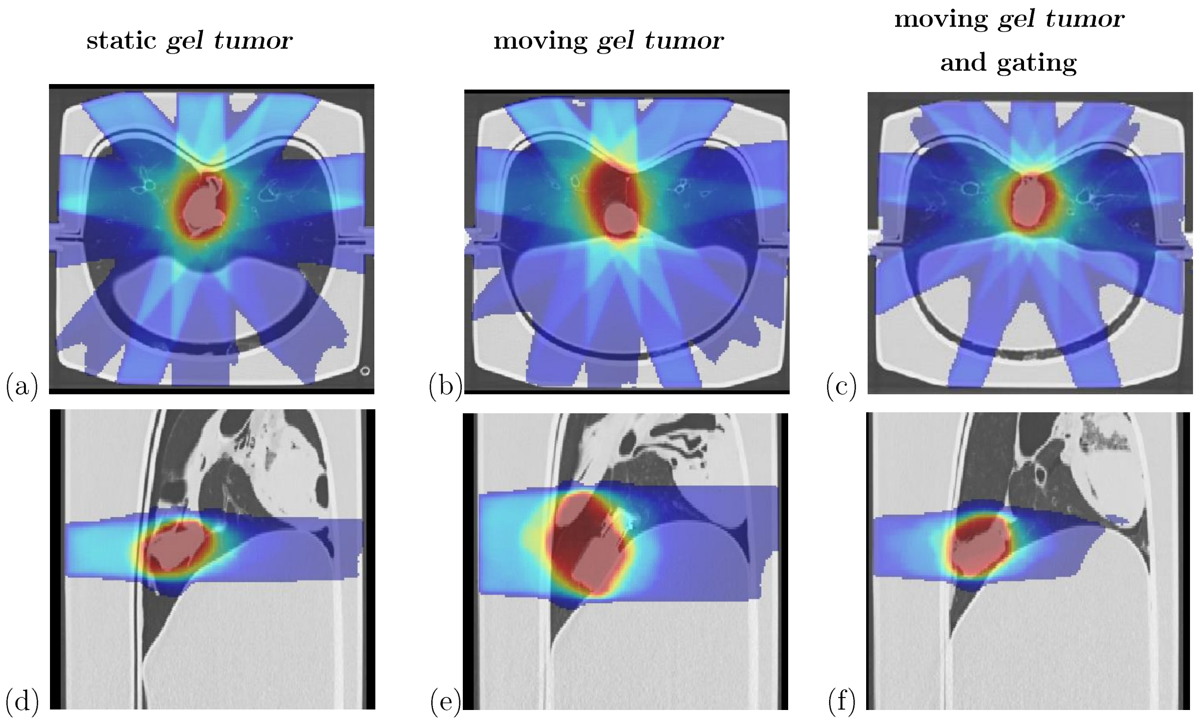

Figure 44. Planning CT (grey) and superimposed calculated dose distribution (colored) for a *gel tumor* irradiation in the (1) static ((a), (d)), (2) dynamic non-gated ((b), (e)) and (3) dynamic gated case ((c), (f)) for a representative transversal ((a), (b) and (c)) and sagittal ((d), (e) and (f)) slice. Nine intersecting beams (blue) are optimized to ensure a uniform PTV coverage (red area). As the *gel tumor* position could not exactly be reproduced, corresponding PTVs differ in shape and location. The beam width significantly varies for individual experiments and is largest for (2) followed by (3) and smallest for the static case (1).

It should be kept in mind, however, that the experiments did not fully address all error sources that can arise during lung tumor treatment of real patients. Due to the reproducible breathing pattern, both, the *gel tumor* motion trajectory during 4D-CT and irradiation showed very high correlation. This is not necessarily true for patients. Therefore, future research should focus on the dosimetric impact for the case, if the *gel tumor* motion is changing over time and, in addition, if the correlation between surrogate signal and the real *gel tumor* position is disturbed. To detect such distortions, real-time fluoroscopic imaging of the *gel tumor* will be included into the workflow. This will require the connection of the experimental setup to the x-ray as well as to the interlock system of the linear accelerator.

4.5 End-to end test for real-time markerless fluoroscopic tumor detection for treatments with beam gating

As shown by previous experiments, the advantage of a gated tumor irradiation is clearly visible as the dose to adjacent OARs can be significantly reduced while the tumor is still uniformly irradiated. However, clinical implementation is rather difficult as an intra-fractional position verification of the tumor position is important, but usually not available. As a result, a disturbance of the correlation of the surrogate signal with the tumor position could in principle cause wrong beam triggering and therefore a significant tumor under-dosage while the dose to the surrounding normal tissue could be increased. To prevent this, a possible solution is the integration of a real-time image-based tumor detection algorithm, which allows verifying the actual tumor position prior to each irradiation. As a prove-of principle, an end-to end test for real-time markerless fluoroscopic tumor detection was performed for treatments with beam gating.

In this experiment, the implemented algorithm has proven to be a good choice for the markerless *gel tumor* detection in real-time. As the training data was based on DRRs from the 4D-CT used for planning, no additional images had to be acquired. Moreover, fluoroscopic images showed a highly comparable image contrast as compared to patients (see Figure 45). The additional exposure expected for the patient was measured to be $7.8 \pm 0.1\ mGy$ (Witte 2016), which is comparable to a single additional CT acquisition of the chest. Results showed very good *gel tumor* coverage without relevant cold- or hot-spots in the *gel tumor* volume and the agreement with the planned dose distribution was comparable to previous experiments ($\gamma_{3D} =\ 91.2\%$). It can therefore be concluded that the implemented workflow of online *gel tumor* position verification can be used to trigger the irradiation. This enables validating the correlation between the surrogate signal of the Anzai respiratory belt and the current tumor position obtained during the 4D planning-CT.

However, further optimization is still required before this technique can be implemented into clinical routine. This especially includes the reduction of the total irradiation time which lasted for about 35 min. This long irradiation time was mainly due to the fact that only every forth breathing cycle was used to minimize the impact of the after-glow effect. Although the imaging detector was in principle designed to be irradiated by the therapeutic beam, the present installation showed severe limitations with this respect. Besides an optimization of the imaging detector, the overall treatment time could also be reduced by (i) acquiring less fluoroscopic images, (ii) increasing the dose rate of the irradiation, e.g. by using the flattening filter free technique, or (iii) by using fewer beam angles within an IMRT-approach, which typically used only five equally-distributed beams.

As the correlation between surrogate signal and the tumor position is not expected to significantly change between two respiratory cycles, fluoroscopic images may not be required for each breathing cycle. The position verification should rather be performed for a pre-defined time interval (e.g. every 60 s) and additionally, if the breathing pattern shows significant irregularities (e.g. caused by coughing). This would further reduce the dose to the patient. Finally, the setting in the performed experiment assumed a perfectly reproducible respiratory breathing pattern, which led to a perfect correlation with the surrogate signal. As previously mentioned, this is not necessarily the case for real patients. As a next step, it is therefore important to demonstrate that the developed method is able to detect irregularities in the correlation of the surrogate signal with the tumor motion.

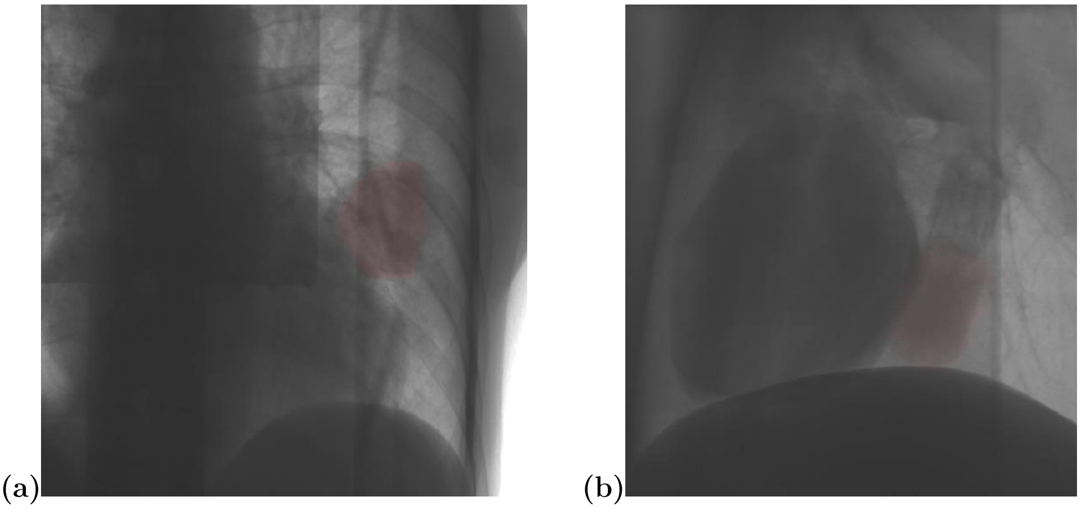

Figure 45. Fluoroscopic image of a real tumor-patient (a) and that of the porcine lung phantom with the gel tumor (b). In both cases, the tumor is automatically detected (displayed in red).

4.6 Validation of the 4D dose calculation for a moving target

With the implementation of the PGD, various treatment- and dose delivery techniques were successfully verified. In all performed experiments, the dose calculation was always considered to be the ground truth which is a good approximation if the target is uniformly irradiated. However, in presence of dose gradients, the calculated static dose distribution cannot be considered to be a reasonable approximation for the actually delivered dose (see *dose-smearing* effect in Figure 36). In this case, it is therefore important to consider the target motion within the dose calculation. As the dose-rate independent PGD integrates the dose distribution over its trajectory, it presents a versatile tool that allows verifying a 4D dose calculation algorithm in 3D.

Prior to the dynamic measurement, two static irradiations were performed to identify any gel-related errors. Results agreed very well with the calculated data when using a PinPoint$^{\text{TM}}$-chamber-based renormalization procedure. However, deviations of up to 1 *Gy* towards the bottleneck region were identified. As this seemed to be systematic and did not depend on the irradiation schemes, it was most likely caused by an altered gel response. A possible explanation could be an oxygen contamination of the gel. As the BAREX$^{\text{TM}}$-lid might capture some oxygen during the filling process, a local oxygen contamination near to the lid may still be possible.

Irradiation under dynamic conditions resulted in high 3D γ-passing rates above 90% when measurements were compared against the 4D dose calculation. These results are well comparable with previously published work for measurements with the same 4D dose calculation algorithm, which used only a film-based 2D-evaluation (Schmitt *et al* 2012). However, the calculated dose profiles showed deviations in the gradient regions (Figure 46(a)). This finding could be related either to errors resulting from (i) the 4D dose calculation, (ii) the Calypso$^{\text{TM}}$-system, which provided the motion trajectory for the dose calculation or (iii) a positioning error of the phantom. As the basic principle of the 4D dose calculation algorithm has already been shown to provide good results, (i) was not considered to be the causes of the deviation.

Analysis of the acquired *gel tumor* motion trajectory, however, showed small deviations between the motion trajectory derived from the Calypso$^{\text{TM}}$-system and that acquired directly from the motion robot. Deviations were especially large for regions of maximum elongation, where the *gel tumor* positions was underestimated for 24 out of 39 cases (mean deviation: $-1.07\ \pm 0.38\ mm$). Therefore, the 4D dose calculation resulted in a dose overestimation in corresponding regions. To analyze this effect in more detail, the 4D dose calculation was repeated using the robot-based rather than the Calypso$^{\text{TM}}$-system-based *gel tumor* trajectory. Although the 3D γ-analysis was only slightly improved (pass rates increased from 90.4% to 91.8%), the shape of the profile in the dose gradient showed a better agreement with the measured data (Figure 46(b)). Nevertheless, the profiles showed a constant offset in the order of $0.2\ Gy$ in the gradient region that could have been caused by a minor positioning shift. Correcting this shift of $\leq 1\ mm$ by an APR resulted in an almost perfect agreement of the profiles (Figure 46(c)).

It is therefore concluded that the 4D dose calculation algorithm in combination with 3D polymer gel dosimetry is very accurate to calculate dynamic target irradiation without the application of motion-compensation techniques. It should be emphasized that the PGD was able to detect both small deviations being caused by the Calypso$^{\text{TM}}$ –based 4D calculation as well as a small positioning shift caused by inaccurate positioning of the phantom. Therefore, the PGD can be considered as a valuable and robust tool for the purpose of workflow verification in adaptive radiation therapy.

In spite of the good agreement found in this study, the implemented dose calculation algorithm is known to have certain limitations when applied in very inhomogeneous media. These limitations may also apply for 4D calculations in the dynamic porcine lung phantom. In addition, the accuracy of the Calypso$^{\text{TM}}$-systems as implemented in this experimental setting may show deviation of up to $1.07\ mm$ with respect to the true position.

Similar to previous applications of polymer gel dosimetry in IMRT (Sandilos *et al* 2004, Gustavsson *et al* 2003, Zhen *et al* 2011), future projects will include the insertion of gel-based OARs to optimize IMRT-treatment plans and to test their robustness in the presence of organ motion. In addition, *gel tumor* motion may be simulated in x-, y-, and z-direction using motion trajectories acquired from patients. The corresponding dose distribution of both, the *gel tumor* and OARs, can then be evaluated in 3D and residual motion can be considered by 4D dose calculations.

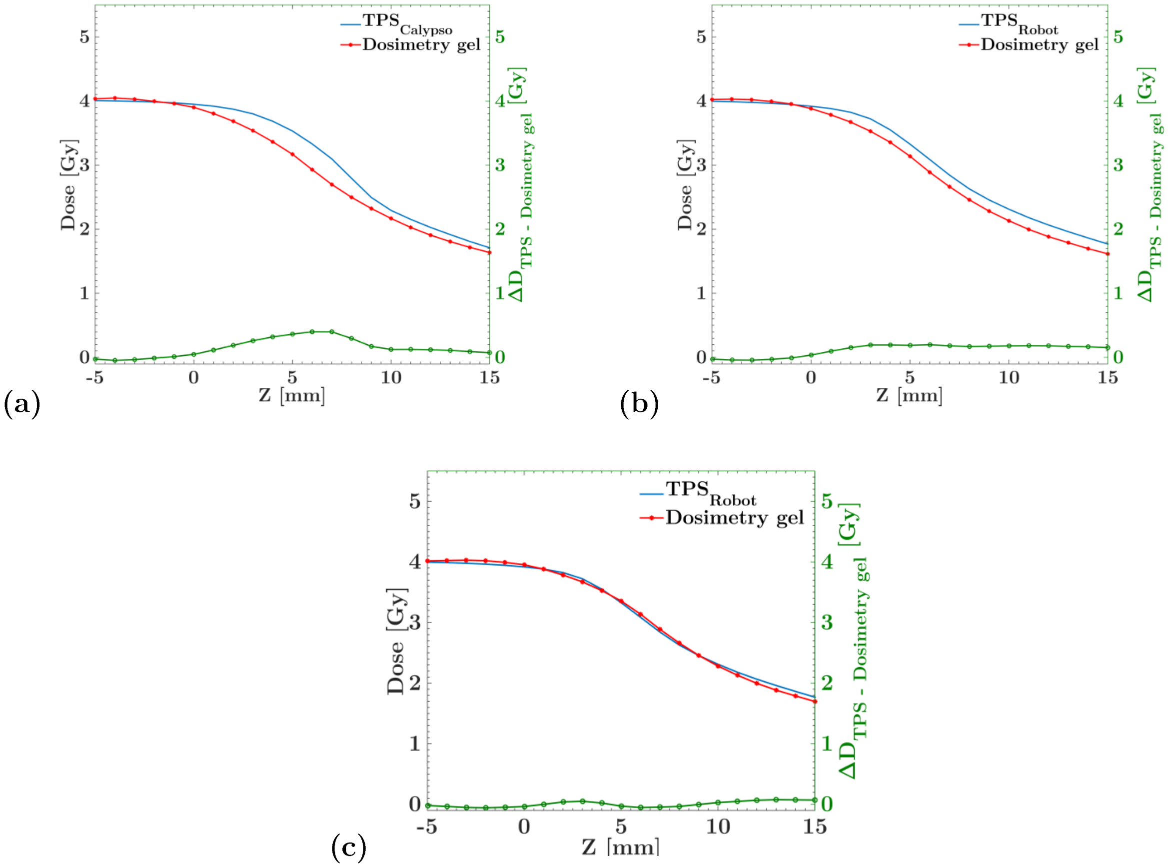

Figure 46. Measured (red) and calculated (blue) dose profiles along the direction of dominant *gel tumor* motion. *Gel tumor* trajectory was obtained either from the Calypso^{TM}-system (a) or from the predefined motion trajectory of the robot (b) and (c). The corresponding dose difference $\Delta D_{TPS-Dosimetry\,gel}$ is displayed in green. While for (a) relatively large variations and large dose differences in the order of 0.4 *Gy* were present, agreement was much better for the robot-based trajectory (b). Here, the maximum dose difference was only 0.2 *Gy* with very small variations indicating a small positioning error. After applying the APR both profiles agree very well (c).

5 Conclusion

The purpose of this thesis was the development and integration of new methods for workflow validation of novel adaptive treatment techniques in radiation therapy. These end-to-end tests are crucial for safe application of advanced treatment techniques and the developed methods were demonstrated for various phantom settings of increasing complexity.

As a first step, suitable procedures for production-, irradiation- and evaluation for polymer gel dosimetry were established. By following a dedicated protocol, the relative 3D dose distributions could be measured with an average dose uncertainty of less than 5%. The polymer gel dosimeter was used to validate patient-specific irradiation procedures with an anthropomorphic porcine lung phantom. This phantom provided both, a realistic image contrast as well as a patient-like respiratory motion pattern. For small-field irradiations under static as well as dynamic motion conditions with and without beam gating, feasibility of gel dosimetry in the porcine lung phantom was demonstrated and good agreement between measured and calculated dose distributions was obtained. The same experimental setting was then used to perform end-to end-tests for different motion-compensated treatment techniques (uniform irradiation for a static phantom, dynamic phantom plus ITV, dynamic phantom plus beam gating and reduced ITV). As a result, high γ-index passing rates between 87.4% and 94.4% were found using the 3%/3 mm mm passing criteria. To independently validate the tumor position in gated treatments, real-time markerless fluoroscopy-based tumor detection was implemented using a template matching algorithm and the result of the tumor-detection was used to trigger the beam. 3D dosimetric evaluation revealed high γ-index passing rates of 91.2%. As the comparison of measured and planned dose is also affected by residual motion, which is normally not reflected in the dose calculation, an in-house developed 4D dose calculation algorithm was verified in 3D for a dynamic phantom setting. This resulted in very good agreement with a high γ-index passing rate of 91.8%.

In conclusion, this thesis established an experimental setting, which allows testing highly advanced adaptive radiation therapy treatment techniques under realistic conditions. The performed end-to-end tests especially included 3D polymer gel dosimetry in anthropomorphic phantoms as well as the real-time evaluation of images of realistic contrast. In all tested clinical workflows, a good agreement between measured and calculated dose was obtained. The established experimental setting can be used to test further advanced treatment techniques in case of intra-fractional tumor motion such as beam gating with additional online tumor localization and the consideration of the impact of residual motion in treatment planning by a 4D dose calculation.

Appendix A

Due to the strict and non-flexible dosimetry gel workflow, the availability of the laboratory, planning CT (if necessary), TPS, LINAC and MR-device need to be checked prior to the gel production.

A.1. Fabrication instructions for the Pre-BANG kit

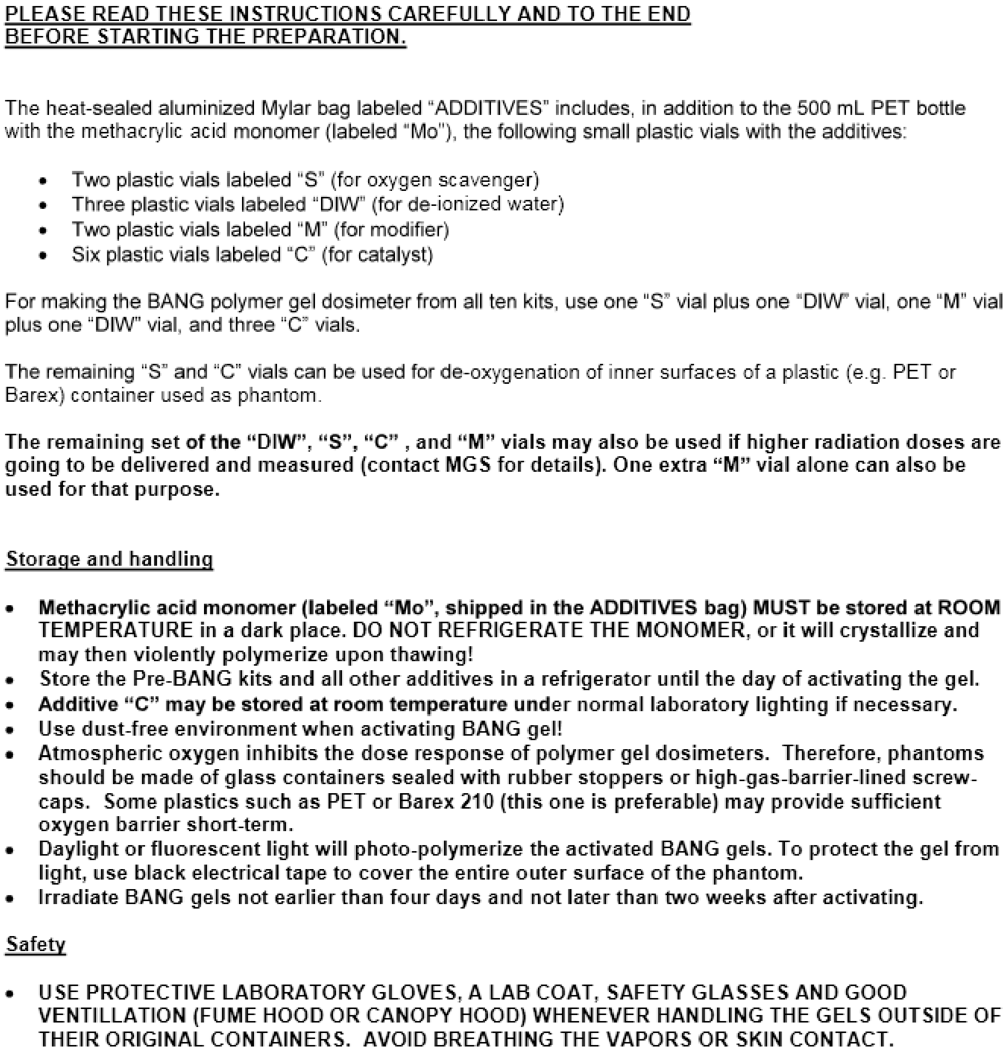

PLEASE READ THESE INSTRUCTIONS CAREFULLY AND TO THE END BEFORE STARTING THE PREPARATION.

The heat-sealed aluminized Mylar bag labeled “ADDITIVES” includes, in addition to the 500 mL PET bottle with the methacrylic acid monomer (labeled “Mo”), the following small plastic vials with the additives:

- Two plastic vials labeled “S” (for oxygen scavenger)
- Three plastic vials labeled “DIW” (for de-ionized water)
- Two plastic vials labeled “M” (for modifier)
- Six plastic vials labeled “C” (for catalyst)

For making the BANG polymer gel dosimeter from all ten kits, use one “S” vial plus one “DIW” vial, one “M” vial plus one “DIW” vial, and three “C” vials.

The remaining “S” and “C” vials can be used for de-oxygenation of inner surfaces of a plastic (e.g. PET or Barex) container used as phantom.

The remaining set of the “DIW”, “S”, “C” , and “M” vials may also be used if higher radiation doses are going to be delivered and measured (contact MGS for details). One extra “M” vial alone can also be used for that purpose.

Storage and handling

- **Methacrylic acid monomer (labeled “Mo”, shipped in the ADDITIVES bag) MUST be stored at ROOM TEMPERATURE in a dark place. DO NOT REFRIGERATE THE MONOMER, or it will crystallize and may then violently polymerize upon thawing!**
- **Store the Pre-BANG kits and all other additives in a refrigerator until the day of activating the gel.**
- **Additive “C” may be stored at room temperature under normal laboratory lighting if necessary.**
- **Use dust-free environment when activating BANG gel!**
- **Atmospheric oxygen inhibits the dose response of polymer gel dosimeters. Therefore, phantoms should be made of glass containers sealed with rubber stoppers or high-gas-barrier-lined screw-caps. Some plastics such as PET or Barex 210 (this one is preferable) may provide sufficient oxygen barrier short-term.**
- **Daylight or fluorescent light will photo-polymerize the activated BANG gels. To protect the gel from light, use black electrical tape to cover the entire outer surface of the phantom.**
- **Irradiate BANG gels not earlier than four days and not later than two weeks after activating.**

Safety

- **USE PROTECTIVE LABORATORY GLOVES, A LAB COAT, SAFETY GLASSES AND GOOD VENTILLATION (FUME HOOD OR CANOPY HOOD) WHENEVER HANDLING THE GELS OUTSIDE OF THEIR ORIGINAL CONTAINERS. AVOID BREATHING THE VAPORS OR SKIN CONTACT.**

Equipment, reagents, and glassware needed (some optional)

- Heavy-duty magnetic hot-plate-stirrer,
- 2" or 3" long stir bar
- Chemical fume hood
- Amber or yellow filtered lamp for gel activation procedure
- A 6L Erlenmeyer flask or a 10L bottle (Pyrex glass) for mixing the gel.
- Isopropyl alcohol and deionized water (or triply-distilled water) for cleaning and rinsing the phantom container
- Al (aluminum) foil
- Compressed nitrogen gas
- A clean Tygon tubing (clean by passing hot water with detergent through the tubing, then do the same with cold de-ionized water alone).
- A clean glass or stainless steel (grade 316L) tube connected tightly to the Tygon tubing for bubbling nitrogen gas through the melted gel
- Thermometer
- Lint-free tissue paper for wiping the glassware dry (white coffee filter paper is excellent!).

Making the scavenger solution (must be done just before mixing the gel).

Open the ADDITIVES pouch. Transfer the entire amount of the de-ionized water from ONE vial labeled "DIW" into ONE vial labeled "S" (it has the scavenger powder inside). If a few drops of the water are left in the "DIW" vial, it does not matter. Close the "S" vial tightly and shake it well until all the powder is completely dissolved. It may take a few minutes. This solution contains the oxygen scavenger needed for utilizing all ten PreBANG kits.

Three "C" (catalyst) vials are needed for that amount of gel.

Making the modifier solution (must be done just before mixing the gel).

Transfer the entire amount of the de-ionized water from ONE vial labeled "DIW" into ONE vial labeled "M" (it has the scavenger powder inside). If a few drops of the water are left in the "DIW" vial, it does not matter. Close the "M" vial tightly and shake it well until all the powder is completely dissolved. It may take a few minutes. This solution contains the response modifier needed for utilizing all ten PreBANG kits.

GENERAL PROTOCOL FOR MAKING THE DOSIMETER

1. Melt the pre-BANG kits by placing them, tightly closed, in a hot water bath (such as a lab sink, or, even better, a cooler box that can keep the temperature for longer, filled with hot water) at 55-60 degrees centigrade, for ninety minutes. Maintain the water bath temperature in the 55-60 deg C range by adding hot water to the bath and draining the excess water as necessary. Shake the pre-BANG kits from time to time to accelerate melting and make it more uniform.
2. Place the magnetic stir bar at the bottom of a clean beaker, bottle or an Erlenmeyer flask (from now on called mixing flask), with the capacity of at least 1.5 of the desired volume of the final gel to be activated. Keep covered with Al foil to keep the dust out.
3. In a fume hood, place the mixing flask described above on a heavy-duty magnetic hot-plate-stirrer. Turn on the hot plate and select about 20% level heat.

4. Remove pre-BANG kits, one by one, from the hot water bath. Wipe each pre-BANG kit bottle dry, then unscrew the cap and transfer the melted gel (=sol) into the mixing flask.
5. When all pre-BANG kits have been transferred to the mixing flask, measure the temperature in the solution.
6. Bring the temperature of the melted pre-BANG to 55 deg C.
7. At this point the amber (or yellow) filtered light should be turned on and the overhead fluorescent light turned off.
8. Under the fume hood, open the bottle labeled “Mo”, then VERY SLOWLY add the contents, while continuously stirring the gel solution, to allow the monomer to be dispersed without forming clumps.
9. Keep stirring the solution at 55 deg C for 30 minutes.
10. SLOWLY add the freshly prepared “S” solution while continuously stirring the sol.
11. SLOWLY add the “C” solution (THREE VIALS) while continuously stirring the sol.
12. SLOWLY add the freshly prepared “M” solution while continuously stirring the sol.
13. Using the Tygon tubing with a glass (or stainless steel) tube, start bubbling nitrogen gas through the sol at a slow flow rate (avoid creating foam or spilling the sol outside the beaker!).
14. Continue stirring at 55 deg C for another 30 minutes, with continued bubbling of nitrogen gas through the sol.
15. Stop stirring to allow the bubbles to rise up for about 15 minutes, and retrieve the nitrogen gas dispensing tube just above the surface of the sol. Cover tightly with Al foil. This nitrogen “blanketing” prevents atmospheric oxygen from entering the sol while the bubbles are rising up.
16. Slowly and very gently dispense the sol into your phantom container(s). Minimize bubble formation by pouring the sol along the inner walls of the container.
17. After dispensing, blow nitrogen gas above the surface of the sol in the phantom for about 15 seconds, then quickly cover the container’s filling port tightly with Al foil. Leave at 20-22 deg C for at least 12 hours, without moving or shaking, well protected from light.
18. When the gel has set, remove the Al foil and blow nitrogen gas over the surface of the gel while having the screw cap or a stopper ready. Quickly retrieve the nitrogen gas dispensing tube and close the container air-tight.
19. The gel may be irradiated after 96 hrs from dispensing into phantom containers, at room temperature or refrigerated. The gel’s dose response is temperature dependent; therefore it is very important to make sure that the temperature is uniform throughout the gel volume during irradiation within +/-1 deg C. This can be obtained by placing the gels overnight in an insulated container (a cooler or Styrofoam box) which has previously been equilibrated to the storage room temperature.

If very low doses (down to 5 cGy) are to be measured, use half the amount of the scavenger solution (“S” plus “DIW”), half the amount of the catalyst, (“C”), and do not use “M” at all.

A.2. Fabrication instructions for the PAGAT dosimetry gel

The following workflow of gel fabrication, -irradiation and -evaluation showed to be a suitable workflow to (i) minimize the influence of penetrating oxygen, (ii) to assure chemical stability after fabrication and (iii) irradiation:

Equipment, reagents and glassware needed for 1 kg of PAGAT

- Deionized water (880 g)
- Gelatine, 300 bloom (60 g)
- Acrylamide (30 g)
- Bis-Acrylamide (30 g)
- THPC (10 $mMol$)
- Chemical fume hood
- 2 x Temperature controlled magnetic hot-plate stirrers
- 4 x Stir bars (length = 4 cm)
- 2 x Water bath container as heat reservoir (1.5 l)
- 2 x Beakers, (2 l)
- Scale (1 $g - 100\ g$)
- Syringe (50 ml)
- Single-channel Pipette (100 µl − 1000 µl)
- Spatula / Spoon
- Respirator
- Safety glasses
- Protection gloves
- Gel flasks (ideally BAREX™)
- Compressed nitrogen gas
- Tygon tubing and a large cannula
- Aluminum foil
- Desiccator

General protocol for making the dosimeter

The production of the gel is based on a protocol described elsewhere (De Deene *et al* 2006). The entire gel production process can be divided into three general steps: (i) preparation of gelatine and monomer solution, (ii) mixing- and (iii) filling procedure. A schematic sketch of the production procedure is displayed in Figure 47.

Preparation of gelatine and monomer solution

Monomer and gelatine solution are both prepared in separate beakers using one temperature controlled magnetic hot-plate stirrer, each. For preparation, the water reservoir is filled with hot water and heated up under constant stirring to a temperature of 42 °C. The preparation of gelatine and monomer solution needs to be prepared simultaneously.

Monomer Production:

Due to the low solubility of the bis-acrylamide monomer in water, 528 *ml* (60%) of the deionized water is used to prepare the monomer solution. For that, the deionized water is placed within the water bath and heated to 42 °C using the digital thermometer placed within the beaker. To ensure a homogeneous distribution of the chemical components, a stirrer is used with a maximum speed between level 1 and 1.5. When the maximum temperature is reached, 30 *g* acrylamide is poured into the water followed by 30 *g* of bis-acrylamide. The acrylamide will be dissolved within 1 minute followed by a temperature drop of approx. 1 - 2 °C. The bis-acrylamide, however, will take up to 30 minutes to be completely dissolved.

Gelatine production:

60 *g* gelatine is mixed with the remaining 352 *ml* deionized water. It is important to insert the magnetic stirrer prior to inserting the gelatine. After a 12 *min* swelling process, the solution is placed inside the water bath and heated up to 42 °C using the digital thermometer. A stirrer is used to ensure homogeneous mixing with a maximum speed between level 1 and 1.5

Once both, gelatine and monomers are completely dissolved, the solution is cooled down to a temperature of 32 °C. This is realized by replacing the hot water bath by colder water of approx. 20 °C. It is very important at this point to avoid temperatures lower than 30 °C as the gelatine will then start to thicken.

Mixing procedure

Once the final temperature is reached, the monomer solution is *carefully* poured into the gelatine beaker to obtain the final dosimetry gel. It should be ensured that the water level of the water bath matches the level of the dosimetry gel. To reduce the amount of dissolved oxygen (De Deene *et al* 2002), nitrogen is flushed for approx. 5 minutes with a pressure of 1.5 *bar* into the dosimetry gel using the tygon tubing and a large cannula. To finalize the gel production, the THPC is then added to the polymer gel under constant stirring. It should be noted that the equipment for the filling process should be well prepared as the dosimetry gel starts to thicken once the THPC is added.

Filling procedure

After approx. 1 – 2 minutes, the THPC is homogeneously distributed and can then be filled into the gel flasks that have been previously flushed with nitrogen. For that, use a 50 *ml* syringe and *carefully* pour the dosimetry into the gel flask avoiding any air inclusions inside the flask. To further guarantee a clear and bubble-free dosimetry gel probe, existing bubbles on the tip of the syringe need to be removed prior to filling dosimetry gel into the flasks. As the influence of light is known to cause polymerization, the flasks were covered with aluminum foil during storage. As the creation of small bubbles inside the gel flask can still occur after production it is recommended to prepare some back-up gel flasks. At the end of the filling process, the gel flasks are stored within a nitrogen flushed desiccator inside a refrigerator at a temperature of 4 °C.

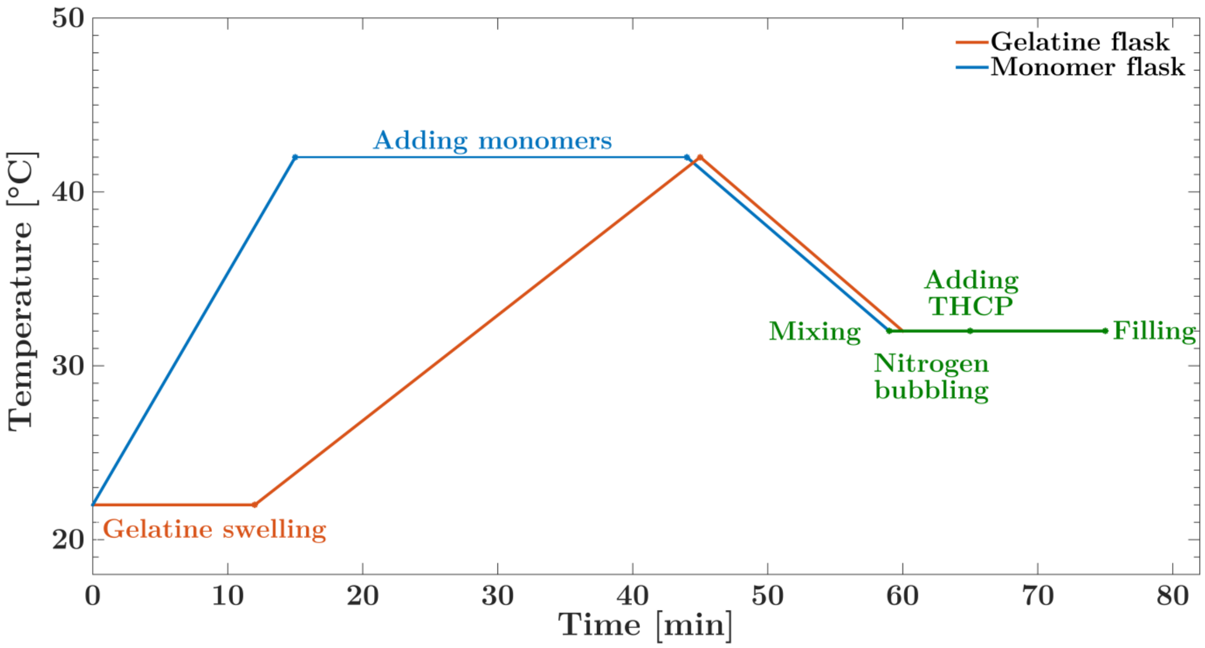

Figure 47. Schematic overview of the PAGAT fabrication workflow

Appendix B

Settings for a standard polymer gel dosimetry measurement

Measurement parameters were optimized regarding the type of PGD irradiation (small-field or homogeneous). All measurements were performed on a Siemens 3T Biograph mMR.

Table 3. Settings of the standard PGD protocol for both, small-field and homogeneous *gel tumor* irradiation.

parameter	**MR**	
	small-field	**homogeneous**
Echo time (TE) [ms]	22.5	40
Repetition time (TR) [ms]	3000	
Field of view (FoV) [mm^2]	128×128	256×256
Matrix	128×128	128×128
Slice Thickness [mm]	1	2
Number of slices	$27 - 30$	$14 - 16$
Number of echoes	32	
Acquisition time (TA) [min]	$6{:}24$ */slice*	
Bandwidth (BW) [Hz/Pix]	130	

List of Figures

List of Tables

Bibliography

Bakai A, Alber M and Nüsslin F 2003 A revision of the gamma-evaluation concept for the comparison of dose distributions. *Phys. Med. Biol.* **48** 3543–53

Baldoc C, Lepage M, Bäck S a, Murry P J, Jayasekera P M, Porter D and Kron T 2001 Dose resolution in radiotherapy polymer gel dosimetry: effect of echo spacing in MRI pulse sequence. *Phys. Med. Biol.* **46** 449–60

Baldock C, De Deene Y, Doran S, Ibbott G, Jirasek A, Lepage M, McAuley K B, Oldham M and Schreiner L J 2010 Polymer gel dosimetry. *Phys. Med. Biol.* **55** R1-63

Balter J M, Wright J N, Newell L J, Friemel B, Dimmer S, Cheng Y, Wong J, Vertatschitsch E and Mate T P 2005 Accuracy of a wireless localization system for radiotherapy. *Int. J. Radiat. Oncol. Biol. Phys.* **61** 933–7

Bert C, Metheany K G, Doppke K and Chen G T Y 2005 A phantom evaluation of a stereo-vision surface imaging system for radiotherapy patient setup *Med. Phys.* **32** 2753

Bert C, Metheany K G, Doppke K P, Taghian A G, Powell S N and Chen G T Y 2006 Clinical experience with a 3D surface patient setup system for alignment of partial-breast irradiation patients. *Int. J. Radiat. Oncol. Biol. Phys.* **64** 1265–74

Biederer J, Dinkel J, Remmert G, Jetter S, Nill S, Moser T, Bendl R, Thierfelder C, Fabel M, Oelfke U, Bock M, Plathow C, Bolte H, Welzel T, Hoffmann B, Hartmann G, Schlegel W, Debus J, Heller M and Kauczor H-U 2009 4D-Imaging of the lung: reproducibility of lesion size and displacement on helical CT, MRI, and cone beam CT in a ventilated ex vivo system. *Int. J. Radiat. Oncol. Biol. Phys.* **73** 919–26

Biederer J and Heller M 2003 Artificial thorax for MR imaging studies in porcine heart-lung preparations. *Radiology* **226** 250–5

Bortfeld T 2006 IMRT: a review and preview. *Phys. Med. Biol.* **51** R363–79

Brock K K and Dawson L A 2014 Point: Principles of Magnetic Resonance Imaging Integration in a Computed Tomography-Based Radiotherapy Workflow *Semin. Radiat. Oncol.* **24** 169–74

Burnet N G, Thomas S J, Burton K E and Jefferies S J 2004 Defining the tumour and target volumes for radiotherapy *Cancer Imaging* **4** 153–61

Calypso Medical Technologies I 2010 *Beacon, Investigator's Brochure - Anchored Transponders., Electromagnetic*

Canny J 1986 A Computational Approach to Edge Detection *IEEE Trans. Pattern Anal. Mach. Intell.* **8** 679–98

Ceberg S, Falk M, Af Rosenschöld P M, Cattell H, Gustafsson H, Keall P, Korreman S, Medin J, Nordström F, Persson G, Sawant A, Svatos M, Zimmerman J and Bäck S Å 2010 Tumor-tracking radiotherapy of moving targets; verification using 3D polymer gel, 2D ion-chamber array and biplanar diode array *J. Phys. Conf. Ser.* **250** 12051

Ceberg S, Karlsson A, Gustavsson H, Wittgren L and Bäck S a J 2008 Verification of dynamic radiotherapy: the potential for 3D dosimetry under respiratory-like motion using polymer gel. *Phys. Med. Biol.* **53** N387-96

Chuter R 2015 The use of deformable image registration to integrate diagnostic MRI into the radiotherapy planning pathway for head and neck cancer *Submitted* **5**

Court L E, Seco J, Lu X-Q, Ebe K, Mayo C, Ionascu D, Winey B, Giakoumakis N, Aristophanous M, Berbeco R, Rottman J, Bogdanov M, Schofield D and Lingos T 2010 Use of a realistic breathing lung phantom to evaluate dose delivery errors. *Med. Phys.* **37** 5850–7

Cui Y, Dy J G, Sharp G C, Alexander B and Jiang S B 2007 Multiple template-based fluoroscopic tracking of lung tumor mass without implanted fiducial markers. *Phys. Med. Biol.* **52** 6229–42

De Deene Y and Baldock C 2002 Optimization of multiple spin-echo sequences for 3D polymer gel dosimetry. *Phys. Med. Biol.* **47** 3117–41

De Deene Y, Hurley C, Venning a, Vergote K, Mather M, Healy B J and Baldock C 2002 A basic study of some normoxic polymer gel dosimeters. *Phys. Med. Biol.* **47** 3441–63

De Deene Y, Pittomvils G and Visalatchi S 2007 The influence of cooling rate on the accuracy of normoxic polymer gel dosimeters. *Phys. Med. Biol.* **52** 2719–28

De Deene Y and Vandecasteele J 2013 On the reliability of 3D gel dosimetry *J. Phys. Conf. Ser.* **444** 12015

De Deene Y, Vergote K, Claeys C and De Wagter C 2006 The fundamental radiation properties of normoxic polymer gel dosimeters: a comparison between a methacrylic acid based gel and acrylamide based gels. *Phys. Med. Biol.* **51** 653–73

De Deene Y and De Wagter C 2001 Artefacts in multi-echo T2 imaging for high-precision gel dosimetry: III. Effects of temperature drift during scanning. *Phys. Med. Biol.* **46** 2697–711

De Deene Y, Wagter C De, Neve W De, Achten E, De Deenet Y, De Wagter C, De Neve W and Achten E 2000 Artefacts in multi-echo T2 imaging for high-precision gel dosimetry: II. Analysis of B1-field inhomogeneity. *Phys. Med. Biol.* **45** 1825–39

De Deene Y, Walle R V De, Achten E, Wagter C D D, Deene Y D, Walle R V De, Achten E and Wagter C D D 1998 Mathematical analysis and experimental investigation of noise in quantitative magnetic resonance imaging applied in polymer gel dosimetry *Signal Processing* **70** 85–101

Ehrbar S, Perrin R, Peroni M, Bernatowicz K, Parkel T, Pytko I, Kl??ck S, Guckenberger M, Tanadini-Lang S, Weber D C and Lomax A 2016 Respiratory motion-management in stereotactic body radiation therapy for lung cancer ??? A dosimetric comparison in an anthropomorphic lung phantom (LuCa) *Radiother. Oncol.* **121** 328–34

Fast M F, Krauss A, Oelfke U and Nill S 2012 Position detection accuracy of a novel linac-mounted intrafractional x-ray imaging system. *Med. Phys.* **39** 109–18

Franz a. M, Schmitt D, Seitel A, Chatrasingh M, Echner G, Oelfke U, Nill S, Birkfellner W and Maier-Hein L 2014 Standardized accuracy assessment of the calypso wireless transponder tracking system *Phys. Med. Biol.* **59** 6797–810

George R, Vedam S S, Chung T D, Ramakrishnan V and Keall P J 2005 The application of the sinusoidal model to lung cancer patient respiratory motion *Med. Phys.* **32** 2850

Giaccone G 2012 *Systemic Treatment of Non-Small Cell Lung Cancer* (OUP Oxford)

Glide-Hurst C K and Chetty I J 2014 Improving radiotherapy planning, delivery accuracy, and normal tissue sparing using cutting edge technologies. *J. Thorac. Dis.* **6** 303–18

Gustavsson H, Karlsson A, Bäck S a J, Olsson L E, Haraldsson P, Engström P and Nyström H 2003 MAGIC-type polymer gel for three-dimensional dosimetry: intensity-modulated radiation therapy verification. *Med. Phys.* **30** 1264–71

Haacke E M, Brown R W, Thompson M R and Venkatesan R 1999 Magnetic Resonance Imaging - Physical Principles and Sequence Design *J. Appl. Phys.* **109** 914

Hennig J 1991 Echoes—how to generate, recognize, use or avoid them in MR-imaging sequences. Part II: Echoes in imaging sequences *Concepts Magn. Reson.* **3** 179–92

ICRU Report No 50 1993 *Prescribing, recording and reporting photon beam therapy* (Washington, D.C., USA)

ICRU Report No 62 1999 *Prescribing, recording and reporting photon beam therapy (supplement to ICRU report 50)* (Washington, D.C., USA)

Jiang S B 2006 Technical aspects of image-guided respiration-gated radiation therapy. *Med. Dosim.* **31** 141–51

Jirasek a and Hilts M 2014 Dose calibration optimization and error propagation in polymer gel dosimetry. *Phys. Med. Biol.* **59** 597–614

Karlsson a, Gustavsson H, Månsson S, McAuley K B and Bäck S a J 2007 Dose integration characteristics in normoxic polymer gel dosimetry investigated using sequential beam irradiation. *Phys. Med. Biol.* **52** 4697–706

Keall P J, Mageras G S, Balter J M, Emery R S, Forster K M, Jiang S B, Kapatoes J M, Low D A, Murphy M J, Murray B R, Ramsey C R, Van Herk M B, Vedam S S, Wong J W and Yorke E 2006 The management of respiratory motion in radiation oncology report of AAPM Task Group 76. *Med. Phys.* **33** 3874–900

Knybel L, Cvek J, Molenda L, Stieberova N and Feltl D 2016 Analysis of Lung Tumor Motion in a Large Sample: Patterns and Factors Influencing Precise Delineation of Internal Target Volume *Int. J. Radiat. Oncol.* **96** 751–8

Koeva V I, Olding T, Jirasek a, Schreiner L J and McAuley K B 2009 Preliminary investigation of the NMR, optical and x-ray CT dose-response of polymer gel dosimeters incorporating cosolvents to improve dose sensitivity. *Phys. Med. Biol.* **54** 2779–90

Kontaxis C, Bol G H, Lagendijk J J W and Raaymakers B W 2015 A new methodology for inter- and intrafraction plan adaptation for the MR-linac *Phys. Med. Biol.* **60** 7485–97

Korreman S 2012 Motion in radiotherapy: photon therapy *Phys. Med. Biol.* **57** R161–91

Korreman S, Mostafavi H, Le Q-T and Boyer A 2006 Comparison of respiratory surrogates for gated lung radiotherapy without internal fiducials. *Acta Oncol.* **45** 935–42

Kubo H D and Hill B C 1996 Respiration gated radiotherapy treatment: a technical study *Phys. Med. Biol.* **41** 83–91

Lepage M, Whittaker A K, Rintoul L and Baldock C 2001 13C-NMR, 1H-NMR, and FT-Raman study of radiation-induced modifications in radiation dosimetry polymer gels *J. Appl. Polym. Sci.* **79** 1572–81

Low D A 2010 Gamma Dose Distribution Evaluation Tool *J. Phys. Conf. Ser.* **250** 12071

Low D A, Harms W B, Mutic S and Purdy J a. 1998 A technique for the quantitative evaluation of dose distributions. *Med. Phys.* **25** 656–61

Mann P, Saito N, Lang C, Runz A, Johnen W, Witte M and Schmitt D 2017a Validation of 4D dose calculation using an independent motion monitoring by the calypso tracking system and 3D polymer gel dosimetry *J. Phys. Conf. Ser.*

Mann P, Witte M, Armbruster S, Runz A, Lang C, Breithaupt M, Berger M, Biederer J, Karger C P and Moser T 2015 Feasibility of polymer gel dosimetry measurements in a dynamic porcine lung phantom *J. Phys. Conf. Ser.* **573** 12079

Mann P, Witte M, Moser T, Lang C, Runz A, Johnen W, Berger M, Biederer J and Karger C P 2017b 3D dosimetric validation of motion compensation concepts in radiotherapy using an anthropomorphic dynamic lung phantom *Phys. Med. Biol.* **62** 573–95

Marquardt D W 1963 An Algorithm for Least-Squares Estimation of Nonlinear Parameters *J. Soc. Ind. Appl. Math.* **11** 431–41

Mate T P, Krag D, Wright J N and Dimmer S 2004 A new system to perform continuous target tracking for radiation and surgery using non-ionizing alternating current electromagnetics *Int. Congr. Ser.* **1268** 425–30

Meiboom S and Gill D 1958 Modified spin-echo method for measuring nuclear relaxation times *Rev. Sci. Instrum.* **29** 688–91

Mercea P, Teske H, Giske K and Bendl R 2015 PD-0464: Adaptive search area template matching for image-based lung tumor tracking *Radiother. Oncol.* **115** S228–9

Mole R H 1984 The LD50 for uniform low LET irradiation of man *Br. J. Radiol.* **57** 355–69

Moser T, Biederer J, Nill S, Remmert G and Bendl R 2008 Detection of respiratory motion in fluoroscopic images for adaptive radiotherapy. *Phys. Med. Biol.* **53** 3129–45

Nolden M, Zelzer S, Seitel A, Wald D, Müller M, Franz A M, Maleike D, Fangerau M, Baumhauer M, Maier-Hein L, Maier-Hein K H, Meinzer H P and Wolf I 2013 The Medical Imaging Interaction Toolkit: challenges and advances *Int. J. Comput. Assist. Radiol. Surg.*

8 607–20

Oldham M, Thomas A, O'Daniel J, Juang T, Ibbott G, Adamovics J and Kirkpatrick J P 2012 A Quality Assurance Method that Utilizes 3D Dosimetry and Facilitates Clinical Interpretation *Int. J. Radiat. Oncol.* **84** 540–6

Papagiannis P, Karaiskos P, Kozicki M, Rosiak J M, Sakelliou L, Sandilos P, Seimenis I and Torrens M 2005 Three-dimensional dose verification of the clinical application of gamma knife stereotactic radiosurgery using polymer gel and MRI. *Phys. Med. Biol.* **50** 1979–90

Plathow C, Fink C, Ley S, Puderbach M, Eichinger M, Zuna I, Schmähl A and Kauczor H-U 2004 Measurement of tumor diameter-dependent mobility of lung tumors by dynamic MRI. *Radiother. Oncol.* **73** 349–54

Reiser M F, Semmler W and Hricak H 2008 *Magnetic Resonance Tomography* (Berlin Heidelberg: Springer-Verlag)

Rudin L I, Osher S and Fatemi E 1992 Nonlinear total variation based noise removal algorithms *Phys. D Nonlinear Phenom.* **60** 259–68

Sandilos P, Angelopoulos A, Baras P, Dardoufas K, Karaiskos P, Kipouros P, Kozicki M, Rosiak J M, Sakelliou L, Seimenis I and Vlahos L 2004 Dose verification in clinical imrt prostate incidents *Int. J. Radiat. Oncol.* **59** 1540–7

Sauer R 2010 *Strahlentherapie und Onkologie* (München: Elsevier, Urban & Fischer)

Schlegel W 2005 Advancing Radiation Medicine *49th Regular Session of the IAEA General Conference* (Vienna: IAEA)

Schlegel W, Pastyr O, Bortfeld T, Becker G, Schad L, Gademann G and Lorenz W J 1992 Computer systems and mechanical tools for stereotactically guided conformation therapy with linear accelerators *Int. J. Radiat. Oncol. Biol. Phys.* **24** 781–7

Schmitt D, Nill S, Roeder F, Herfarth K and Oelfke U 2012 SU-E-J-147: Dosimetric Consequences of Intrafraction Prostate Motion: Comparison Between Phantom Measurements and Three Different Calculation Methods *Med. Phys.* **39** 3686

Schreiner L J 2006 Dosimetry in modern radiation therapy: limitations and needs *J. Phys. Conf. Ser.* **56** 1–13

Schuenke P, Windschuh J, Roeloffs V, Ladd M E, Bachert P and Zaiss M 2017 Simultaneous mapping of water shift and B 1 (WASABI)-Application to field-Inhomogeneity correction of CESTMRI data *Magn. Reson. Med.* **77** 571–80

Shah A P, Kupelian P A, Waghorn B J, Willoughby T R, Rineer J M, Mañon R R, Vollenweider M A and Meeks S L 2013 Real-time tumor tracking in the lung using an electromagnetic tracking system. *Int. J. Radiat. Oncol. Biol. Phys.* **86** 477–83

Sharp G, Li R, Wolfgang J, Chen G, Peroni M, Spadea M F and Kandasamy N 2010 Plastimatch: an open source software suite for radiotherapy image processing *Proceedings of the XVI'th International Conference on the use of Computers in Radiotherapy (ICCR)* (Amsterdam)

Siddon R L 1985 Prism representation: a 3D ray-tracing algorithm for radiotherapy applications. *Phys. Med. Biol.* **30** 817–24

Siewerdsen J H and Jaffray D A 2001 Cone-beam computed tomography with a flat-panel imager: magnitude and effects of x-ray scatter. *Med. Phys.* **28** 220–31

Szegedi M, Rassiah-Szegedi P, Fullerton G, Wang B and Salter B 2010 A proto-type design of a real-tissue phantom for the validation of deformation algorithms and 4D dose calculations. *Phys. Med. Biol.* **55** 3685–99

Tacke M B, Nill S, Krauss A and Oelfke U 2010 Real-time tumor tracking: Automatic compensation of target motion using the Siemens 160 MLC *Med. Phys.* **37** 753

Tang X, Sharp G C and Jiang S B 2007 Fluoroscopic tracking of multiple implanted fiducial markers using multiple object tracking. *Phys. Med. Biol.* **52** 4081–98

Teske H, Mercea P, Schwarz M, Nicolay N H, Sterzing F and Bendl R 2015 Real-time markerless lung tumor tracking in fluoroscopic video: Handling overlapping of projected structures *Med. Phys.* **42** 2540–9

Vandecasteele J and De Deene Y 2013a Evaluation of radiochromic gel dosimetry and polymer gel dosimetry in a clinical dose verification. *Phys. Med. Biol.* **58** 6241–62

Vandecasteele J and De Deene Y 2013b On the validity of 3D polymer gel dosimetry: I. Reproducibility study *Phys. Med. Biol.* **58** 19–42

Vandecasteele J and De Deene Y 2013c On the validity of 3D polymer gel dosimetry: II. Physico-chemical effects *Phys. Med. Biol.* **58** 43–61

Vandecasteele J and De Deene Y 2013d On the validity of 3D polymer gel dosimetry: III. MRI-related error sources. *Phys. Med. Biol.* **58** 63–85

Vandecasteele J and De Deene Y 2013e Polymer gel dosimetry of an electron beam in the presence of a magnetic field *J. Phys. Conf. Ser.* **444** 12104

Vásquez C, Runz A, Echner G, Sroka-Perez G and Karger C P 2012 Comparison of two respiration monitoring systems for 4D imaging with a Siemens CT using a new dynamic breathing phantom *Phys. Med. Biol.* **57** N131–43

Vedam S S, Keall P J, Kini V R, Mostafavi H, Shukla H P and Mohan R 2003 Acquiring a four-dimensional computed tomography dataset using an external respiratory signal. *Phys. Med. Biol.* **48** 45–62

Venning J, Hill B, Brindha S, Healy B J and Baldock C 2005 Investigation of the PAGAT polymer gel dosimeter using magnetic resonance imaging. *Phys. Med. Biol.* **50** 3875–88

Vergote K 2005 *Development of polymer gel dosimetry for applications in intensity-modulated radiotherapy*

Vergote K, De Deene Y, Duthoy W, Gersem W De, Neve W De, Achten E and Wagter C De 2004 Validation and application of polymer gel dosimetry for the dose verification of an intensity-modulated arc therapy (IMAT) treatment *Phys. Med. Biol.* **49** 287–305

Vinet L and Zhedanov A 1970 International Commission ON Radiation Units and Measurements (ICRU). *Am. J. Roentgenol. Radium Ther. Nucl. Med.* **109** 417

Witte M 2010 *Evaluation of dosimetry gels for use in an anthropromorphic phantom* (University of Heidelberg)

Witte M 2016 *Markerless fluoroscopic real-time tumor detection for adaptive radiotherapy realized in an anthropomorphic lung phantom* (University of Heidelberg)

Zentrum für Krebsregisterdaten im Robert Koch-Institut 2016 *Bericht zum Krebsgeschehen in Deutschland 2016* (Berlin)

Zhen H, Nelms B E and Tomé W a. 2011 Moving from gamma passing rates to patient DVH-based QA metrics in pretreatment dose QA *Med. Phys.* **38** 5477

List of publications

Journal articles

Mann P, Witte M, Armbruster S, Runz A, Lang C, Breithaupt M, Berger M, Biederer J, Karger C P and Moser T 2015 Feasibility of polymer gel dosimetry measurements in a dynamic porcine lung phantom *J. Phys. Conf. Ser.* **573** 12079

Niebuhr N I, Johnen W, Güldaglar T, Runz A, Echner G, **Mann P**, Möhler C, Pfaffenberger A, Jäkel O and Greilich S 2016 Technical Note: Radiological properties of tissue surrogates used in a multimodality deformable pelvic phantom for MR-guided radiotherapy. *Med. Phys.* **43** 908–16

Mann P, Witte M, Moser T, Lang C, Runz A, Johnen W, Berger M, Biederer J and Karger C P 2017 3D dosimetric validation of motion compensation concepts in radiotherapy using an anthropomorphic dynamic lung phantom *Phys. Med. Biol.* **62** 573–95

Mann P, Saito N, Lang C, Runz A, Johnen W, Witte M and Schmitt D 2017 Validation of 4D dose calculation using an independent motion monitoring by the calypso tracking system and 3D polymer gel dosimetry *J. Phys. Conf. Ser.* ***[In print]***

Conference contributions

Mann P, Witte M, Armbruster S, Runz A, Lang C, Breithaupt M, Berger M, Biederer J, Karger C P and Moser T 2015 Feasibility of polymer gel dosimetry measurements in a dynamic porcine lung phantom. In: *IC3DDose* (2014)

Mann P, Witte M, Armbruster S, Runz A, Lang C, Breithaupt M, Berger M, Biederer J, Karger C P and Moser T: Feasibility of polymer gel dosimetry measurements in a dynamic porcine lung phantom. In: *4D Treatment Planning Workshop* (2014)

Mann P, Witte M, Runz A, Lang C, Moser T, Lang C, Biederer J, Karger C P and Moser T: Geometric and dosimetric validation of motion monitoring techniques in respiratory-gated radiotherapy using a dynamic lung phantom combined with dosimetry gels. In: *Retreat of the National Center for Radiation Research in Oncology, NCRO* (2015)

Mann P, Heußer T, De las Heras Gala H, Kachelrieß M and Bachert P: An MR-PET-CT phantom for quality assurance and research. In: *European Congress of Radiology, ECR* (2015)

Mann P, Witte M, Moser T, Lang C, Runz A, Berger M, Biederer J and Karger C P: Geometric and dosimetric validation of dose distributions in a dynamic anthropomorphic lung phantom using dosimetry gel. In: *46. Jahrestagung der Deutschen Gesellschaft für Medizinische Physik, DGMP* (2015)

Runz A, **Mann P**, Barry S, Boßler D, Johnen W, Echner G and Jäkel O: Einsatz von Dosimetrie Gelen in anthropomorphen Modellen. In: *46. Jahrestagung der Deutschen Gesellschaft für Medizinische Physik, DGMP* (2015)

Niebuhr N I, Johnen W, Güldaglar T, Runz A, Echner G, **Mann P**, Möhler C, Pfaffenberger A, Jäkel O and Greilich S: Multimodales, anthropomorphes und deformierbares Beckenphantom zur Untersuchung der Unsicherheiten bei MRT-geführter Strahlentherapie. In: *46. Jahrestagung der Deutschen Gesellschaft für Medizinische Physik, DGMP* (2015)

Mann P (invited talk for a teaching sesstion): Hybrid imaging phantom for research applications and quality control for PET/MR and PET/CT systems. In: *32nd Annual scientific meeting of the European Society for Magnetic Resonance in Medicine and Biology, ESMRMB* (2015)

Mann P, Heußer T, De las Heras Gala H, Weigel R, Kachelrieß M and Bachert P: A Hybrid Imaging Phantom for Quality Assurance and Research. In: *101st scientific assembly and annual meeting of the Radiological Society of Nothern America, RSNA* (2015)

Mann P, Witte M, Moser T, Lang C, Runz A, Berger M, Biederer J and Karger C P: Geometric and dosimetric validation of motion monitoring techniques in respiratory-gated radiotherapy using a dynamic lung phantom in combination with dosimetry gels. In: *4D Treatment Planning Workshop* (2015)

Heußer T, **Mann P**, Schäfer M, Dimitrakopoulou-Strauss A, Kachelrieß M, Schlemmer H P and Freitag M T: The Halo–Artifact in 68Ga–PSMA–PET/MRI: Studies Using Phantom and Clinical Data. In: 5th Conference on PET/MR and SPECT/MR, PSMR (2016)

Runz M, Runz A, **Mann P** and Jäkel O: Range assignment of protons in 18-oxygenated dosimetry gel using MR-PET imaging. In: *European Congress of Medical Physics, ECMP* (2016)

Witte M, Mercea P, **Mann P**, Moser T, Häring P, Lang C, Biederer J and Karger C P: MITK as multi-functional evaluation tool in modern adaptive radiotherapy. In: *Annual MITK user meeting* (2016)

Witte M, Mercea P, **Mann P**, Moser T, Häring P, Lang C, Biederer J and Karger C P: Evaluation eines Verfahrens zur fluoroskopischen Echtzeit-Positionsüberwachung von Lungentumoren in einem anthropomorphen Lungenphantom. In: *47. Jahrestagung der Deutschen Gesellschaft für Medizinische Physik, DGMP* (2016)

Runz M, Runz A, **Mann P**, Witte M and Jäkel O: Reichweitenbestimmung von Protonen in 18-Sauerstoff angereichertem Dosimetrie-Gel mittels MR-PET Bildgebung. In: *47. Jahrestagung der Deutschen Gesellschaft für Medizinische Physik, DGMP* (2016)

Witte M, Mercea P, **Mann P**, Moser T, Häring P, Lang C, Biederer J and Karger C P: Markerless fluoroscopic real-time tumor detection for adaptive radiotherapy realized in an anthropomorphic lung phantom. In: *4D Treatment Planning Workshop* (2016)

Mann P, Saito N, Lang C, Runz A, Johnen W, Witte M and Schmitt D 2017 Validation of 4D dose calculation using an independent motion monitoring by the calypso tracking system and 3D polymer gel dosimetry. In: *IC3DDose* (2016)

Acknowledgments

Prof. Dr. Peter Bachert and Prof. Dr. Joao Seco, I am very grateful for kindly accepting to be my first and second referee for my dissertation.

I would also like to express my special thanks to Prof. Dr. Christian Karger for the long and valuable discussions.

Finally, I would like to thank all of those who supported me during my project.

Explanation

I hereby assure that I composed this work by myself and did not use any other than the listed resources.

Heidelberg, 28.02.2017 ………………………………………………………………